UNIVERSITY OF SOUTHAMPTON

FACULTY OF ENGINEERING, SCIENCE & MATHEMATICS

OPTOELECTRONICS RESEARCH CENTRE

TAPERED WAVEGUIDE LASERS

by

Simon James Hettrick

Thesis submitted for the degree of Doctor of Philosophy

September, 2003.

UNIVERSITY OF SOUTHAMPTON

ABSTRACT

FACULTY OF ENGINEERING, SCIENCE AND MATHEMATICS
OPTOELECTRONICS RESEARCH CENTRE

Doctor of Philosophy

TAPERED WAVEGUIDE LASERS.

By Simon James Hettrick

The work reported in this thesis concerns the design and fabrication of tapered waveguide lasers to allow efficient, high-power diode-pumping and produce diffraction-limited, near-symmetrical output, whilst maintaining a monolithic design compatible with integrated optical circuits.

The design rules required for efficient operation of a tapered waveguide are derived, and applied to the fabrication of tapered waveguides by thermal ion exchange (TIE) in Nd-doped borosilicate glass. Ti:sapphire pumped laser operation of these waveguides indicates efficient (40%) and low-loss ($0.2dBcm^{-1}$) operation, comparable to that of a channel waveguide fabricated within the same substrate. Parabolic and linear taper shapes are compared, and the linear shape is found to provide superior operation at wide taper expansions (up to $250\mu m$, over a length of $\approx 22mm$), and hence is more suited to end-pumping with multi-watt broad-stripe-diodes. Broad-stripe-diode end-pumping is also investigated, and the laser performance is characterised, indicating a need to control the refractive index profile to maximise the overlap of the multimode-pump and single-mode laser. Field-assisted ion exchange is therefore investigated to improve the overlap of the diode-pump and laser modes in a tapered waveguide. Waveguides produced by this technique are shown to exhibit the desired step-like index profile, but require further optimisation to improve the laser performance.

Low-loss ($0.1dBcm^{-1}$) operation of a tapered waveguide laser is reported in a hybrid Nd-doped/undoped borosilicate glass. The hybrid glass is proposed as a useful substrate for reducing the quasi-3-level reabsorption loss of Yb^{3+}-doped lasers. As an initial step towards this goal, channel waveguides are fabricated in standard Yb^{3+}-doped phosphate glass, which exhibit efficient (50–75%) and moderate-loss ($0.6dBcm^{-1}$) laser operation.

The design requirements for a power scalable diode-side-pumped tapered waveguide laser are also investigated, and YVO_4 is proposed as a suitable substrate material due to its high absorption coefficient. The indiffusion of Nd, Gd and Ti is characterised for the first time, and the fabrication of the first Nd-indiffused waveguide in YVO_4 is reported.

I had a terrible education, I attended a school for emotionally disturbed teachers.

— Woody Allen

Acknowledgements

Over the past four years I've been really looking forward to writing the acknowledgements, however, thanking everyone that has helped me through this time - in one page - is going to be difficult. Here goes:

Firstly, I'd like to thank my supervisor Dave Shepherd for his constant help, optimistic attitude and the look of panic he does when you say something stupid before the vi va. Cheers Dave!

I'd also like to thank Jacob Mackenzie (Matchcad Man) and Cheng Li for the diode-pumping, Dave Sager and Neil Sessions the cleanroom Guru's and Angelique Favre for the glass bonding.

Outside of work (the best place to be in my opinion) I've found a number of people without whom life would have been very dull. The most notable culprits are Taj Bhutta for providing advice galore, being useless at Goldeneye and his somewhat savage critique of my writing. Denis Guilhot - next for the chop - who came round every Thursday to see if I was still alive, then cooked my lunch and listened to me rant about Physics for an hour, and Barry Dunne for being delightfully non-ORC and thrashing me repeatedly at chess. I'd also like to thank the transient population of office 2071 for the larking about over the years, don't let the portacabin break the Babylon ethic. And make them give you shelves.

My Mum and Dad who not only had to put up with laser-based conversations bordering on the torturous, but paid me to do it! Thanks for the support, and I hope you're not upset that the thesis has nothing to do with floppy disks.

Finally, I'd like to thank my angelic girlfriend, Della Camp, without whom I would have been hairier, smellier and a lot thinner during my write-up. Fortunately I was supplied with food and a constant barrage of optimism that I'll never forget.

Contents

Chapter 1

Introduction

1.1 Diode-pumped Solid-State Lasers

Solid-state lasers have been the focus of a great deal of research since the realisation of the first laser in 1960 [1]. The solid-state lasers detailed in this thesis consist of a host material, either a crystal or glass, doped with an active ion. Both semiconductor lasers and the relatively new ceramic based lasers [2] are also classified within the solid-state laser group, however, the scope of this thesis is limited to diode-pumped solid-state glass and crystal lasers. An extensive number of active ions have been studied, the majority of which belong to the rare-earth (RE) or transition metal groups, allowing access to a wavelength range that spans from the ultraviolet to the mid-infrared. This vast wavelength range has allowed solid-state lasers to find applications within such diverse fields as medicine, materials processing, range-finding and research. Host materials have also been extensively studied, with hundreds of possible hosts presently available [3].

Early work with solid-state lasers was limited by the flashlamps originally used as the pump source [4]. The demonstration of the first laser diode in 1962 [5], followed by improvements in their lifetime, power and efficiency, initiated interest in their use as solid-state pump sources. The benefits of a pump source with high brightness and an improved spectral match to the laser absorption were realised only two years later, with the production of the first diode-pumped solid-state laser [6].

Early diode-lasers suffered from limited output powers, and are still limited to powers of $\approx 10W$ for an individual diode emitter [7,8]. However, far greater power can be accessed through the use of diode-bars, although this increase in power is accompanied by an increase in the beam asymmetry and a reduction in the beam quality. Therefore, the benefits of a diode-laser pump have to be offset against the difficulties involved with efficiently coupling the highly asymmetric and multimode pump beam into a solid-state gain medium. Various solutions have been proposed for coupling into bulk media such as: re-shaping the beam [9], the use of reflective pump chambers [10, 11], lens ducts [12] and fibre coupling [13]. With the exception of reflective pump chambers, these solutions attempt to improve the geometrical match of the diode-laser output with the bulk-laser mode, and rely on manipulating the diode-laser output. An alternative approach is to design a laser gain medium that naturally provides a geometrical match with the output from a diode-laser. The planar waveguide is such a structure; it is inherently well matched to the diode-laser output, allowing a reduction in the pump coupling optics required [14], or in some cases, requiring no coupling optics at all [15].

1.2 The Waveguide Geometry

There are a number of possible waveguide geometries, all of which operate by confining optical radiation within the waveguide core through the use of total internal reflection. Examples of the main geometries are depicted in figure 1.1.

Waveguide lasers benefit from a number of advantages when compared to their bulk counterparts. Small beam areas are possible through tailoring of the confinement, which can result in a low threshold power if the waveguide propagation loss is also low. The confinement effectively negates free-space divergence and, when combined with the small beam area, results in a high intensity-length product and therefore a high gain per unit pump power. The monolithic design of waveguide lasers allows a level of immunity to cavity misalignment, and decreases their suscepti-

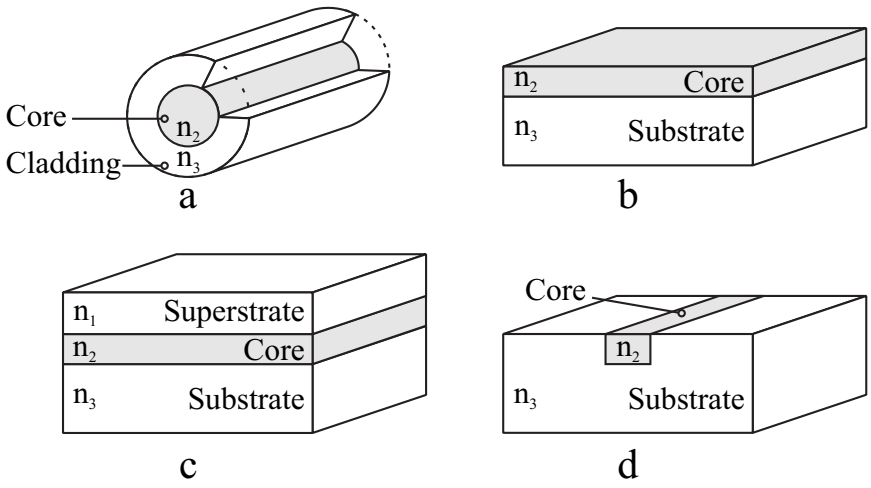

Figure 1.1: Main waveguide geometries: a/ Fibre, b/ 3-layer, air-clad planar, c/ 3-layer planar, d/ Channel

bility to vibration, moisture and temperature drift. The slab geometry, of which the planar waveguide is an extreme example, is well known to have superior thermal properties in comparison to the rod geometry [16], and is therefore attractive for reducing thermally induced problems experienced under high pump powers.

Planar fabrication methods, and the planar geometry of the laser itself, are perfectly suited to the production of optoelectronic integrated circuits (OIC's) [17]. The possibilities of the OIC have been discussed since 1960, with research fuelled by the desire to produce a renaissance in optics similar to that which accompanied the production of the first electronic integrated circuits (IC's). The development of the OIC has been hampered by the lack of an optical analogue to silicon, and the lack of suitable laser sources [18]. The tapered waveguide laser, investigated in the following chapters, fulfils the requirements of such a device with early research showing reasonable output power, efficiency and near-symmetric, single transverse mode operation.

1.2.1 Waveguide Lasers

The first waveguide laser utilised the confinement of a multimode fibre to overcome the poor quality glass available at the time [19]. Improvements

in the fabrication of optical glasses have resulted in the production of extremely low-loss fibres ($< 0.1dBkm^{-1}$), which are attractive laser hosts. Although the fibre geometry is not inherently suited to diode-laser pumping, the innovation of double-clad fibres [20, 21] has led to output powers up to $110W$ with near-diffraction limited output [22], and $272W$ with only a slightly reduced beam quality [23].

In comparison to fibre lasers, planar waveguides benefit from a geometrical match to the output of a diode-laser and fabrication is possible within many different host materials. There is also a greater degree of versatility concerning the pump arrangement, with three separate geometries possible. In the end-pumped geometry (figure 1.2a), both the laser and pump propagate co-linearly, allowing the greatest overlap between pump and laser modes [25], although scaling to higher powers is limited by the use of a single pump source. Side-pumping (figure 1.2b), in which the pump and laser propagate perpendicularly, suffers from a reduced pump and laser overlap, which can lead to a lower efficiency in comparison to end-pumping. A significant advantage of the side-pumped geometry is that simple power scaling can be achieved by increasing the length over which the waveguide is pumped to allow more pump units, or by pumping both side faces [26]. Face pumping (figure 1.2c) also has the potential for power scaling, as the large area of the top face can be pumped with stacked diode bars [27]. However, relatively large core depths and reflective pump chambers are required for efficient absorption.

RE doped, planar waveguide lasers were first realised in 1972 [24], but suffered from a high threshold power and required cooling to $77K$. Two decades elapsed before the advent of the first high-power diode-side-pumped waveguide laser, which consisted of a Nd^{3+}-doped yttrium aluminium garnet (YAG) layer grown by liquid phase epitaxy on an undoped YAG substrate [28]. Since this time research into waveguide devices has focussed on producing higher output powers and improving the output beam quality. At present powers up to $150W$ have been obtained from a Nd:YAG planar waveguide laser, face-pumped by stacked diode-bar lasers [29]. However, the design of this laser is non-monolithic and re-

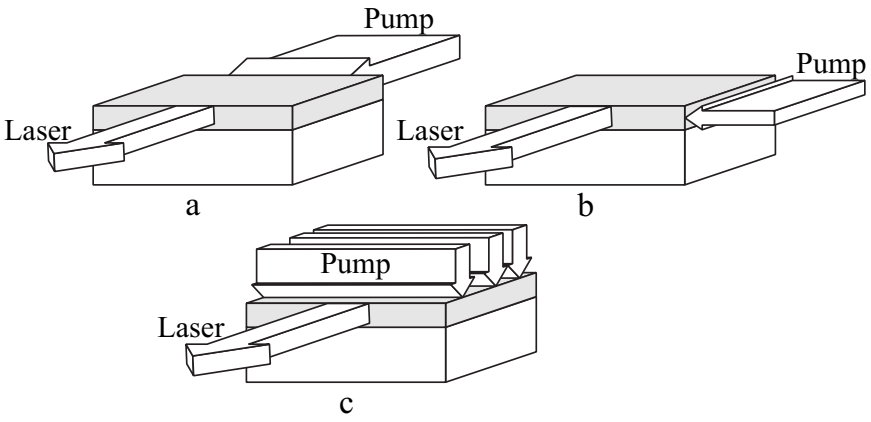

Figure 1.2: Pump geometries: a/ End-pumping, b/ Side-pumping, c/ Face-pumping

quires a hybrid unstable-stable resonator to improve the beam quality.

It would be desirable to obtain both high output power and diffraction limited performance from a monolithic laser design. These specifications restrict waveguide design, as efficient pump coupling requires a multi-mode waveguide, whereas diffraction limited performance requires single-mode laser operation. One method is the use of double-clad planar waveguides, which have led to output powers of $> 10W$ for Tm^{3+} [26], Yb^{3+} [30] and Nd^{3+}-doped YAG [30]. However, diffraction limited performance is only achieved in the guided axis of the waveguide.

1.2.2 The Tapered Waveguide Laser

A different approach is required to attain the goal of diffraction-limited operation in both axes, combined with a monolithic design and access to reasonably high pump powers. The most straightforward technique is to focus the pump beam to match the fundamental laser mode. The beam waist ω_0 in a stable laser cavity can be calculated with reference to the following equation [31]:

$$\omega_0 = \left(\frac{L\lambda}{\pi}\right)^{\frac{1}{2}} \left[\frac{g_1 g_2 \left(1 - g_1 g_2\right)}{\left(g_1 + g_2 - 2g_1 g_2\right)^2}\right]^{\frac{1}{4}} \tag{1.1}$$

Where L is the cavity length, λ is the wavelength within the gain material, $g_{1,2} = 1 - L/R_{1,2}$ and $R_{1,2}$ is the curvature of the end-face mirrors.

A near-planar, monolithic cavity of a few centimetres in length, lasing at $\approx 1\mu m$, would lead to a beam waist size in the order of a $100\mu m$, which limits pumping to sources that can be efficiently focussed to this degree. Alternatively, the high gain afforded by the waveguide geometry allows the use of a hybrid unstable/stable resonator to improve the non-guided beam quality of a planar waveguide, with a recent non-monolithic device shown to operate successfully [32]. A monolithic design has also been produced, through the fabrication-intensive procedure of polishing curved waveguide end-faces, but this prototype requires further optimisation before successful operation can be attained [33]. Diffraction limited output in both directions can be achieved through the use of a channel structure, although this geometry is not well suited to high-power diode-pumping. Output powers of only $1W$ [34] have been demonstrated, and an external cavity was required to achieve diffraction-limited output.

An alternative solution is to combine both the planar and channel geometries, in an attempt to gain the benefits of both. The resulting geometry is that of the tapered waveguide, which is depicted in figures 1.3 and 1.4. The tapered waveguide consists of a broad section to allow efficient coupling of a diode-laser, a channel waveguide to select single mode operation and an interconnecting adiabatic taper. The taper allows conversion of the single laser mode within the channel section, to a single mode of greater lateral size within the broad section. Any higher order modes excited during the mode size conversion would be radiated from the waveguide as the mode returned to the channel section. A fundamental requirement for low-loss taper operation, is that the taper maintains all power within the single-mode during the mode size conversion. Operation of this nature is termed 'adiabatic operation' and is possible through careful taper design [35, 36].

Milton and Burns [35] have shown that adiabatic expansion of a parabolic taper can be designed with reference to the following equation:

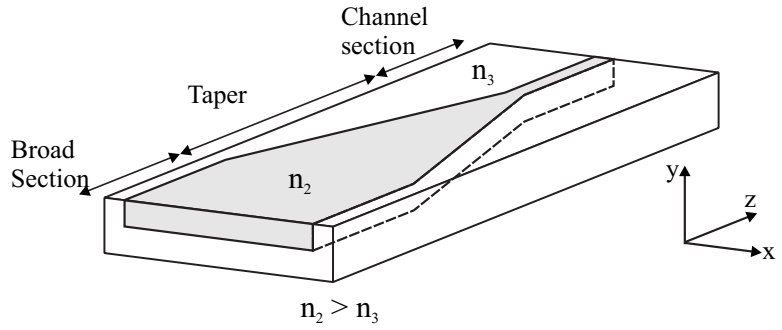

Figure 1.3: 3D view of a tapered waveguide

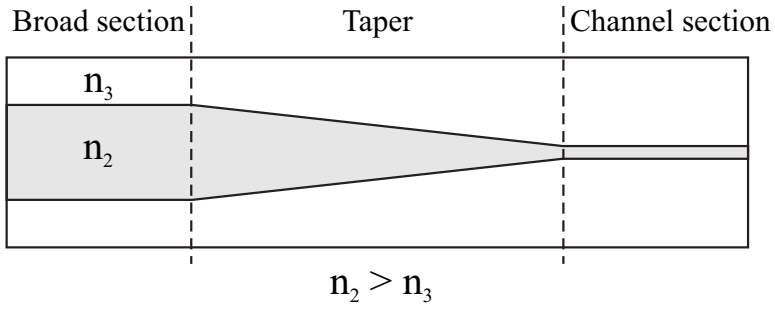

Figure 1.4: Plan view of a tapered waveguide

$$L = \frac{W^2 n_3}{2\alpha\lambda_0} \tag{1.2}$$

Where L is the taper length, W is the taper width, n_3 is the refractive index of the substrate and λ_0 is the free-space wavelength. The coefficient α controls the rate at which the taper opens, and is therefore linked to the adiabatic performance of the taper. Milton and Burns reccomend an $\alpha \leqslant 1$ for adiabatic taper performance [35]. For reasons that will be explained in section 3.3, equation 1.2 is only applicable to waveguides fabricated with a small difference between the refractive index of the core and the substrate (typically 10^{-3}), such as the tapered waveguides produced during this thesis.

Equation 1.2 limits the taper width for a given length, and in this way can be seen as a limit on the rate of taper opening. Efficient diode-bar end-pumping of a tapered waveguide would require a broad section width of $\approx 5mm$, whereas single-mode operation requires a channel width in the order of a few microns. Adiabatic mode conversion between these

vastly different channel widths would require a taper length of $\approx 20m$, which is impractical due to limits on substrate size, fabrication capabilities and propagation losses. However, a broad section width of ≈ 200–$300\mu m$ could be adiabatically converted over a length of ≈ 2–$3cm$, which would allow end-pumping with a single emitter broad-stripe diode, and access to pump powers up to 4W. The first ion-exchanged tapered waveguide laser is demonstrated in chapter 4, early results of diode pumping are also discussed in this chapter. Side-pumping of the broad section with a diode-bar may be possible if the waveguide is fabricated in a material with an absorption coefficient of sufficient magnitude to absorb the pump power over the width of the broad section. The material requirements and the possibilities of this pump geometry are discussed in more detail in chapter 6.

1.3 Solid-State Materials

The work described in the following chapters concerns the laser operation of two ions: neodymium and ytterbium, within two different glass hosts: BK7, a popular silicate glass for optical applications and IOG-1, a relatively new phosphate glass. Initial steps towards the fabrication of a neodymium doped yttrium vanadate laser are also described.

1.3.1 Active Ions

The laser operation of neodymium (Nd) and ytterbium (Yb) doped waveguides are studied during this thesis. The relevant energy levels of these ions are depicted in figure 1.5. Rare earth ions have the advantageous property that the $4f$ electrons, utilised during lasing, are shielded from the crystal field by the filled, outer-lying $5s$ and $5p$ electron shells [3]. The effect of this shielding is to produce relatively narrow emission lines, and allows the absorption and emission characteristics of the ion to be relatively unaffected by doping in different hosts.

During laser operation the Nd^{3+} ion is optically pumped to a high lying

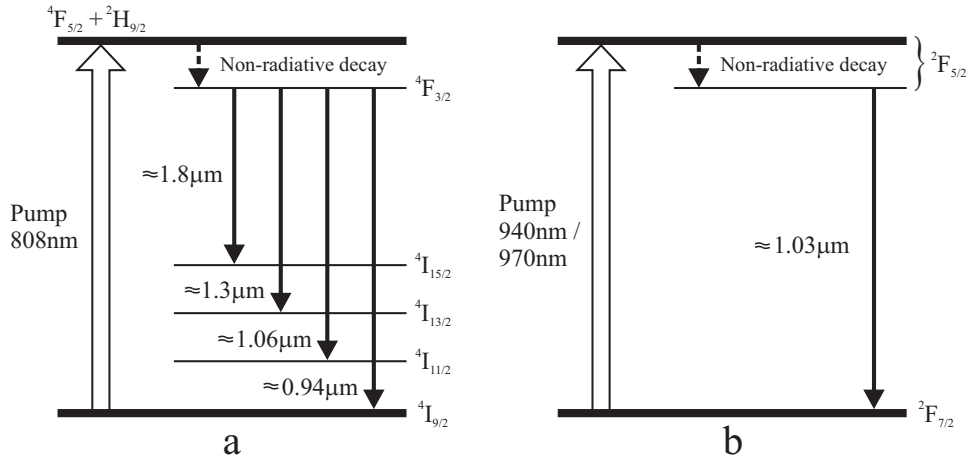

Figure 1.5: Relevant energy levels of a/ neodymium, and b/ ytterbium laser ions

manifold, followed by fast non-radiative decay to one of the Stark split levels of the $^4F_{3/2}$ manifold. The strongest transition, from the $^4F_{3/2}$ to the $^4I_{11/2}$ manifold, results in an emission wavelength of $\lambda \approx 1.06\mu m$. The laser operation of the Nd^{3+} ion is four-level in nature, as the $^4I_{11/2}$ manifold is high above the ground state and is therefore unpopulated at room temperature. Apart from the transition to the $^4I_{11/2}$ manifold, other weaker transitions are also possible to the $^4I_{15/2}$, $^4I_{13/2}$ and $^4I_{9/2}$ manifolds, resulting in emission wavelengths of $\lambda \approx 1.8\mu m$, $\lambda \approx 1.3\mu m$ and $\lambda \approx 0.9\mu m$ respectively.

Initial research into the laser operation of the Yb^{3+} ion was limited by the difficulties involved with flashlamp pumping at the required wavelength of $\approx 0.94\mu m$ or $0.97\mu m$ [37]. The advent of diode-lasers that could efficiently pump at these wavelengths renewed interest in the Yb^{3+} ion, as it exhibits some attractive features for high power lasers [38]. The small quantum defect between the pump and the $\approx 1.03\mu m$ laser wavelength results in reduced thermal loading of the host material, and allows higher output powers to be gained for a given pump power. The Yb^{3+} ion displays no higher lying or intermediate manifolds, which eliminates the concentration dependent effects suffered by Nd^{3+} systems [39], allowing higher Yb^{3+} concentrations to be utilised in order to improve the laser gain. One drawback is that the lower laser level of Yb^{3+} is one of the Stark

split levels of the ${}^2F_{7/2}$ ground state manifold, which is thermally populated at room temperature. The resulting quasi-three level operation of an Yb^{3+} laser suffers from re-absorption loss leading to a higher threshold than that of four-level systems.

1.3.2 Host Materials

Laser hosts can be split into two main categories: glasses and crystals. Glasses have a number of favorable properties which include low cost, large substrate size, high homogeneity, chemical durability, doping flexibility and an index match with optical fibres [40]. In comparison to crystal hosts, glasses suffer from lower thermal conductivity, which limits their high power operation, and emission broadening. However, a reason for the continued use of glass in waveguide applications is its compatibility with the ion exchange fabrication technique, which allows simple and reproducible waveguide production. Chapters 4 and 5 deal with the production of glass waveguides by ion exchange.

In comparison to glasses, crystal hosts are known to possess superior mechanical strength, thermal conductivity and benefit from a narrower emission linewidth when doped with active ions, however, the cost, doping flexibility and substrate size is often poor in comparison. Yttrium aluminium garnet (YAG) has achieved a position of dominance for high power applications, due to the ability to dope with Nd^{3+} and Yb^{3+} ions and its very high thermal conductivity and mechanical strength. However, YAG is not a suitable host for the side-pumping of relatively narrow waveguides, as will be considered in chapter 6, due to a typical absorption length of a few millimetres for diode-pump sources. In comparison to Nd:YAG, Nd^{3+}-doped yttrium vanadate (Nd:YVO_4) benefits from an absorption coefficient $\approx 3\times$ greater, a broader absorption band and a stimulated emission cross-section $\approx 6\times$ greater [41, 42]. These properties are very attractive to the diode-side-pumping of the relatively narrow waveguides discussed in the previous section. Chapter 6 discusses the possibilities of diode-side-pumping Nd:YVO_4 waveguides and details the first waveguides fabricated in YVO_4 by indiffusion. The high power operation of

YVO_4 is limited by its thermal conductivity [43], which is approximately half that of YAG, however, the thermal management of the planar geometry should go some way to overcoming this shortfall.

1.4 Waveguide Fabrication

A wide variety of fabrication techniques are available for the production of waveguides, which can be separated into two groups: layer alteration, which involves the alteration of the upper layer of a substrate and layer deposition, which involves the growth of a new layer on a substrate. Typically the choice of fabrication method is dependant upon the desired properties of the final laser device, i.e. the required host material, waveguide geometry, numerical aperture (NA) and refractive index profile.

Layer alteration techniques often require relatively simple fabrication procedures, are reproducible and cheap to perform. However, as many of these techniques are driven by thermal diffusion they are highly dependent on the process temperature, which can result in lengthy fabrication durations [44]. The low refractive index change caused by these techniques, and hence the low numerical aperture (NA), is perfectly suited to the production of single mode waveguides, but is not best suited for pumping with non-diffraction limited sources.

The process of ion-exchange has been utilised for glass strengthening for over a century [45] and was first used for the production of waveguides in 1972 [46]. Ion-exchange operates by exchanging a mobile ion within a glass substrate (the glass ion), with another ion (the diffusant ion) of different polarisability and/or ionic radius to alter the refractive index of the glass. The source of the diffusant ions can be either a molten salt [47–49] or a metal film [50, 51]. Thermal ion exchange (TIE) is based on diffusion kinetics and therefore the size of the waveguide produced is dependent upon the process temperature (often 300–$500^{\circ}\mathrm{C}$) and the process duration. The diffusion based fabrication produces a graded refractive index profile with the maximum index at the surface of the waveguide [52], although a two-step process has resulted in buried waveguides [53]. The production

of buried waveguides has also been completed using a novel ion exchange technique that involves the contact bonding of a potassium rich glass with a glass of lower potassium concentration [54]. This process benefits from a single-step fabrication procedure and can be combined with UV writing to produce channel waveguides [55].

Field-assisted ion exchange (FAIE) was developed to allow greater flexibility over the index profile, and is especially useful for the production of step-index waveguides [52]. FAIE is identical to TIE, except for the addition of an electric field applied across the sample. The electric field drives the migration of the exchanger ions, with fields of sufficient magnitude allowing the thermal diffusion characteristics of the ion exchange to be overcome [45]. Both TIE and FAIE often result in waveguide propagation losses of $\leqslant 0.2dBcm^{-1}$ [45].

Proton exchange is strongly related to ion-exchange and involves exchanging lithium ions within crystals of lithium niobate ($LiNbO_3$) or lithium tantalate ($LiTaO_3$), with H^+ ions from an acidic solution. The simplicity of the process, coupled with the low propagation losses of $0.15dBcm^{-1}$ [56], has allowed proton exchange to become one of the two major methods used for waveguide fabrication within these crystals. The alternative method for production of low-loss ($\leqslant 0.5dBcm^{-1}$ [57, 58]) waveguides is the process of indiffusion [59, 60], which has also been completed in sapphire [61] and most recently within YVO_4, as discussed in chapter 6. The process involves applying a metal film to the surface of a crystal substrate, followed by heating of the substrate to temperatures $\approx$ 1000–2000°C. During heating, ions within the metal layer diffuse into the crystal, and alter the crystal's refractive index. The index profile produced by indiffusion is graded, with the shape dependant on fabrication parameters [44]. The main benefits of the process are the ability to produce waveguides in crystal media, selective doping with active ions, and the possible use of the diffusant ion as both the index modifier and the active ion [62].

As these processes require a supply of diffusant ions to alter the refractive index, selectively shielding areas of the substrate allows the simple production of channel, or more complex waveguide geometries. In the case

of ion exchange and proton exchange, the shielding is completed using a thick layer of metal with features delineated through photolithography and etching. Patterning of the metal source, through the use of a photolithographic lift-off technique, is used to delineate features for indiffusion. The simplicity involved with the production of channel waveguides by ion exchange and indiffusion led to their use for the fabrication of tapered waveguides during this thesis.

UV writing is a relatively new technique for the fabrication of channel waveguides in glass, which relies on the photosensitivity of various glasses to UV radiation. A UV laser is focussed into the glass substrate and induces a refractive index change. Channel waveguides are fabricated by scanning the substrate through the use of a computer controlled translation stage. The main benefit of this method is the flexibility of the waveguide geometries that can be fabricated, without the necessity of lengthy photolithographic procedures [64]. The process is suited to the production of low-loss waveguides ($< 0.2dBcm^{-1}$ [65]), however, as with the other layer alteration processes discussed here, the refractive index change due to this process is low ($\Delta n \approx 10^{-3}$ [63]) leading to the production of low NA waveguides.

Layer deposition methods involve the growth of a new layer on top of a substrate material. The production of high NA and relatively thick layers is possible, with low losses reported for many of the techniques. Epitaxial growth is required for crystalline materials, as it was realised early in the development of waveguide lasers that polycrystalline layers led to high propagation losses [66]. The requirement of epitaxial growth limits the materials that can be grown on a given substrate to those with a close lattice match, and this in turn applies limits to the possible NA of the resulting waveguide. Although these methods are well suited to the production of planar waveguides, the majority do not allow the production of channel waveguides and are therefore not suited to the fabrication of tapered waveguides. As previously discussed, tapered waveguides fabricated by layer alteration suffer from a low NA, which limits efficient diode-pumping. It may be possible to improve the coupling efficiency of

a tapered waveguide laser using a double-clad design [15], with the extra layers grown through the use of a layer deposition process.

Various layer deposition methods are available such as: liquid phase epitaxy (LPE) [67,68], molecular beam epitaxy (MBE) [69], pulsed laser deposition (PLD) [70], Sol-Gel [71] and flame hydrolysis deposition (FHD) [72]. One technique that is inherently well matched to the production of high NA, double-clad waveguides is contact (also referred to as thermal or direct) bonding. This process involves the high-quality polishing of a core and substrate material, which are chemically cleaned and contacted together. Van der Waals forces bond the two materials with a sufficient bond strength to allow mechanical thinning of the core to the required depth [73]. The process can be repeated to cap the core with a superstrate material, or to produce double-clad devices [15]. Contact bonding is an extremely flexible technique, as no lattice match is required between the two materials, however, it is preferable for the materials to share a similar thermal expansion coefficient to inhibit fracture under high power operation. The flexibility in the choice of the materials allows dissimilar material such as Nd:YAG and glass to be bonded, resulting in a very high NA of 0.8 [73]. As no alteration of the material is required during contact bonding, the spectral properties are identical to that of bulk materials and very low-loss waveguides ($0.2dBcm^{-1}$ [14]) can be produced.

1.5 Synopsis

The remainder of this thesis is separated into five chapters, which are organised in the following manner.

The equations that govern light propagation within both a step and graded index waveguide are derived in chapter 2. The step and graded index profiles apply to the ion exchanged and indiffused waveguides fabricated later in the thesis. Laser theory is defined within this chapter, and the effects of the waveguide geometry are discussed. Equations governing the expected laser threshold and slope efficiency are derived, which enables the characterisation of the tapered waveguide lasers discussed in

later chapters.

An overview of the tapered waveguide and the theory of their operation is discussed in chapter 3. Requirements for the design of tapered waveguides are detailed, followed by the analysis of a variety of tapered structures using the beam propagation method (BPM).

The theory, practical requirements and fabrication of thermal ion exchanged waveguides are detailed in chapter 4. The operation of tapered and channel waveguide lasers are detailed under titanium sapphire and broad-stripe diode-laser pumping. Chapter 5 investigates the possibilities of field-assisted ion exchange, with special focus on the production of step-index waveguides.

An initial investigation of indiffusion in YVO_4 is detailed in chapter 6, followed by a discussion of the theory and practicalities required for the production of high power diode-side-pumped tapered waveguides. The fabrication and analysis of planar diffused YVO_4 waveguides is completed, and conclusions are drawn concerning the future of this research.

The final chapter includes the conclusions to the work presented in this thesis, followed by the possibilities for future research.

1.6 Aims and Objectives

1.6.1 Ion Exchanged Tapered Waveguide Lasers

The principle aim in the production of a tapered waveguide laser, using the ion exchange fabrication method in glass, is the production of a $1W$-class laser. The tapered waveguide will be designed to be compatible with diode-end-pumping, whilst producing a diffraction-limited output beam.

A tapered waveguide laser, fabricated in Nd^{3+}-doped BK7, can be assumed to operate with a slope efficiency of $\approx 50\%$. Under this condition, an incident diode-pump power of $\approx 4W$ would be required to achieve an $\approx 1W$ output power, assuming a conservative launch efficiency of 50%.

Diode name	Model no.	Output Power (at 808nm) W	M^2 (slow axis/fast axis)
Diode A	382D-1330E-3-1	4	39×3.2
Diode B	462D-1375E-3-1	2	22×1.9

Table 1.1: Characteristics of the broad-stripe diode-pump sources used for end-pumping the ion exchanged tapered waveguide laser

The diode-pump beam quality, measured by the M^2 value, is fundamental to achieving a reasonable launch efficiency, and can be related to the numerical aperture NA, and size D of the waveguide by the following equation:

$$M^2 = \frac{D \times NA}{\lambda} \tag{1.3}$$

The maximum M^2 of the diode-pump beam, required to attain reasonable launch efficiency, can be calculated by entering values for the NA achieved by the potassium/sodium ion exchange technique in BK7 glass, as used throughout this thesis, and the minimum taper width of $200\mu m$, as discussed in section 1.2.2. It can be seen that a maximum allowable diode pump M^2 of ≈ 40 is required in the width of the tapered waveguide. The depth of the waveguide is determined by the ion exchange technique, with a depth of $\approx 10\mu m$ achievable in reasonable process times. Use of equation 1.3 with $D = 10\mu m$ produces a maximum allowable diode-pump M^2 of ≈ 2, in the depth of the waveguide.

Two broad-stripe diode-lasers were purchased from the supplier, Polaroid, under this rationale. The properties of these diode-lasers conform with the requirements discussed in the previous paragraph and are listed in table 1.1.

Diode A allows access to the power assumed to be necessary for the production of a $1W$-class laser, as previously discussed. However, the superior beam quality of diode B may allow a higher launch efficiency, which would reduce the wasted power and therefore the overall efficiency of the

device, whilst allowing access to output powers of 0.5–$1W$.

The main benefit of the tapered waveguide design is the relatively straightforward method of producing a diffraction-limited output. Tailoring the physical size of the channel section of the tapered waveguide, so that only a single transverse mode is supported in both the depth and width of the channel, should allow near-diffraction-limited output. Theoretically, an output beam quality with an $M^2 \approx 1$ could be attained.

1.6.2 Indiffused Waveguides in Yttrium Vanadate

As discussed in section 1.3.2, it may be possible to diode-side-pump the broad section of a tapered waveguide laser. In relation to end-pumping, the side-pump arrangement allows a lower diode-pump, slow-axis beam quality to be launched into the waveguide. The broad section of the tapered waveguide can be fabricated with any desired length, and is limited only by the substrate size and fabrication constraints. The relatively small substrate size available would limit the broad section length to $\approx 10mm$. Use of equation 1.3 with $D = 10mm$, assuming an identical NA to that of the ion exchange process, sets a maximum limit on the lateral diode-pump beam quality of $M^2 \approx 2000$. However, it is reasonable to assume that the beam quality in the depth of the waveguide would still be limited to $M^2 \approx 2$. Diode-bars with output powers in the order of $50W$ are available with an M^2 approximately equal to these requirements. Diode-bar side-pumping of a tapered waveguide at a power of $\approx 50W$ may allow access to an output laser power of $\approx 10W$, in a near-diffraction-limited beam.

The relatively narrow taper widths of 200–$300\mu m$, obtained over a reasonable substrate length, would require the tapered waveguide to be produced in a material with a high pump absorption coefficient. Yttrium vanadate (YVO_4), doped with $1at\%$ Nd^{3+}, benefits from a maximum absorption coefficient of $37cm^{-1}$, for light polarised parallel to the crystal c-axis. The absorption length of a diode-pump (with its polarisation aligned to the c-axis of the YVO_4 crystal) would be $\approx 300\mu m$. It is therefore possi-

ble to absorb a fraction of at least $1/e$ of the launched diode-power, which theoretically, may allow the production of an efficient diode-side-pumped tapered waveguide laser.

Local doping of the laser ion is required for efficient side-pumping. The process of indiffusion would allow both local doping with the laser ions, and the production of a waveguide in the YVO_4 crystal host. However, indiffusion in YVO_4 has not been studied and, for this reason, the first aim of this section is the determination of the diffusion characteristics of the Nd^{3+} ion in YVO_4. Calculation of the diffusion coefficient of the Nd^{3+} ion, would allow the design and fabrication of waveguides with a suitable doping concentration and waveguide depth, for the production of tapered waveguide lasers. The diffusion characteristics of Gd^{3+} and Ti^{x+} will also be investigated, as these ions may prove to be suitable for index modification, which would allow flexibility over the design of the index and gain profiles.

To highlight the applicability of the indiffusion technique, it is also desirable to produce the first indiffused waveguide in YVO_4. Once this first waveguide has been produced, determination of the waveguide properties would allow later waveguides to be designed with specific waveguide properties. It would be desirable to produce a waveguide that supports a single mode at the Nd^{3+} laser wavelength, however, this may not be possible at this early stage.

1.7 References

[1] T. Maiman. Stimulated Optical Radiation in Ruby. *Nature*, 187 : p493–494, 1960.

[2] J.H Lu, J.R. Lu, T. Murai, K. Takaichi, T. Uematsu, J.Q. Xu, K. Ueda, H. Yagi, T. Yanagitani, A.A. Kaminskii. 36-W diode-pumped continuous-wave 1319-nm Nd : YAG ceramic laser. *OL*, 27(13) : p1120–1122, 2002.

[3] W. Koechner. Solid-State Laser Engineering. *Springer Verlag*, Ch. 2, Berlin, 1999.

[4] R.L. Byer. Diode Laser-Pumped Solid-State Lasers. *Science*, 239 : p742–747, 1988.

[5] R.D. Dupuis. An Introduction to the Development of the Semiconductor Laser. *IEEE Journal of Quantum Electronics*, QE-23(6) : p651–657, 1987.

[6] R.J. Keyes and T.M. Quist. Injection luminescent pumping of CaF_2:U^{3+} with GaAs Diode Lasers. *Applied Physics Letters*, 4(3) : p50–52, 1964.

[7] J. Sebastian, G. Beister, F. Bugge, F. Buhrandt, G. Erbert, H.G. Hansel, R. hulsewede, A. Knauer, W. Pittroff, R. Staske, M. Schroder, H. Wenzel, M. Weyers and G. Trankle. High-Power 810nm GaAsP-AlGaAs Diode Lasers with Narrow Beam Divergence. *IEEE Journal on Selected Topics in Quantum Electronics*, 7(2) : p334–338, 2001.

[8] A. Al-Muhanna, L.J. Mawst, D. Botez, D.Z. Garbuzov, R.U. Martinelli and J.C. Connolly. High-Power ($> 10W$) continuous-wave operation from 100-μm-aperture 0.97-μm-emitting Al-free diode lasers. *Applied Physics Letters*, 73(9) : p1182–1184, 1998.

[9] W.A. Clarkson and D.C. Hanna. Two-mirror beam-shaping technique for high-power diode-bars. *Optics Letters*, 21(6) : p375–377, 1996.

[10] D.V. Pantelic, B.M. Panic and L. Belic. Solid-state laser pumping with a planar compound parabolic concentrator. *Applied Optics*, 36(30) : p7730–7740, 1997.

[11] Y. Wang, I. Hirano and H. Kan. Theoretical study on absorption efficiency for a LD side-pumped Nd:YAG laser with infinite convergence approach. *Infrared Physics and Technology*, 44(3) : p213–225, 2002.

[12] R.J. Beach. Theory and optimization of lens ducts. *Applied Optics*, 35(12) : p2005–2015, 1996.

[13] C. Yelland and W. Sibbett. Stable 4W CW solid-state green source pumped by fibre-coupled diode-laser arrays. *Journal of Modern Optics*, 43(5) : p893–902, 1996.

[14] D.P. Shepherd, C.L. Bonner, C.T.A. Brown, W.A. Clarkson, A.C. Tropper, D.C. Hanna and H.E. Meissner. High-numerical-aperture, contact-bonded, planar waveguides for diode-bar-pumped lasers. *Optics Communications*, 160 : p47–50, 1999.

[15] C.L. Bonner, T. Bhutta, D.P. Shepherd and A.C. Tropper. Double-Clad Structures and Proximity Coupling for Diode-Bar-Pumped Planar Waveguide Lasers. *IEEE Journal of Quantum Electronics*, 36(2) : p236–242, 2000.

[16] J.M. Eggleston, T.J. Kan, K. Kuhn, J. Unternahrer and R.L. Byer. The Slab Geomtery – Part 1: Theory. *IEEE Journal of Quantum Electronics*, QE-20(3) : p289–301, 1984.

[17] S.I. Najafi. Introduction to Glass Integrated Optics. *Artech House*, Ch. 1, Norwood, 1992.

[18] R.G. Hunsperger. Integrated Optics: Theory and Technology. *Springer Verlag*, Ch. 1, Berlin, 1985.

[19] E. Snitzer. Optical Maser Action of Nd^{3+} in a Barium Crown Glass. *Physical Review Letters*, 7(12) : p444–446, 1961.

[20] G. Bouwmans, R.M. Percival, W.J. Wadsworth, J.C. Knight and P. St. J. Russell. High-power Er:Yb fiber laser with very high numerical aperture pump-cladding waveguide. *Applied Physics Letters*, 83(5) : p817–818, 2003.

[21] M. Hofer, M.E. Fermann and L. Goldberg. High-Power Side-Pumped Passively Mode-locked Er-Yb Fiber Laser. *IEEE Photonics Technology Letters*, 10(9) : p1247–1249, 1998.

[22] V. Dominic, S. MacCormack, R. Waarts, S. Sanders, S. Bicknese, R. Dohle, E. Wolak, P.S. Yeh and E. Zucker. 110W fibre laser. *Electronics Letters*, 35 : p1158–1160, 1999.

[23] Y. Jeong, J.K. Sahu, R.B. Williams, D.J. Richardson, K. Furusawa and J. Nilsson. Ytterbium-doped large-core fibre laser with 272W output power. *Electronics Letters*, 39(13) : p977–978, 2003.

[24] J.P. Van der Ziel, W.A. Bonner and L.G. Van Uitert. Coherent Emission from Ho^{3+} Ions in Epitaxially Grown Thin Aluminium Garnet Films. *Physics Letters*, 42A(1) : p105–106, 1972.

[25] C.L. Bonner, C.T.A. Brown, D.P. Shepherd, W.A. Clarkson, A.C. Tropper and D.C. Hanna. Diode-bar end-pumped high-power Nd:$Y_3Al_5O_12$ planar waveguide laser. *Optics Letters*, 23(12) : p942–944, 1998.

[26] J.I. Mackenzie, S.C. Mitchell, R.J. Beach, H.E. Meissner and D.P. Shepherd. 15W diode-side-pumped Tm:YAG waveguide laser at $2\mu m$. *Electronics Letters*, 37(14) : p898–899, 2001.

[27] A. Faulstich, H.J. Baker and D.R. Hall. Face pumping of thin, solid-state slab lasers with laser diodes. *Optics Letters*, 21(5) : p594–596, 1996.

[28] D.C. Hanna, A.C. Large, D.P. Shepherd, A.C. Tropper, I. Chartier, B. Ferrnad and D. Pelenc. A side-pumped Nd:YAG epitaxial waveguide laser. *Optics Communications*, 19 : p229–235, 1992.

[29] J.R. Lee, H.J. Baker, G.J. Friel, G.J. Hilton and D.R. Hall. High-average-power Nd:YAG planar waveguide laser that is face pumped by 10 laser diode bars. *Optics Letters*, 27(7) : p524–526, 2002.

[30] R.J. Beach, S.C. Mitchell, H.E. Meissner, O.R. Meissner, W.F. Krupke, J.M. McMahon and W.J. Bennet. Continuous-wave and passively Q-switched cladding-pumped planar waveguide lasers. *Optics Letters*, 26(12) : p881–883, 2001.

[31] O. Svelto. Principles of Lasers. *Plenum Press*, New York, Fourth Edition, Ch.5, 1998.

[32] H.J. Baker, A.A. Chesworth, D.P. Millas and D.R. Hall. A planar waveguide Nd:YAG laser with a hybrid waveguide-unstable resonator. *Optics Communications*, 191 : p125–131, 2001.

[33] J.I. Mackenzie. High-Brightness Diode-Pumped Waveguide Lasers. *PhD. Thesis*, Ch. 5, University of Southampton - Southampton, 2003.

[34] U. Griebner and H. Sconnagel. Laser operation with nearly diffraction-limited output from a Yb:YAG multimode channel waveguide. *Optics Letters*, 24(11) : p750–752, 1999.

[35] A.F. Milton and W.K. Burns. Mode Coupling in Optical Waveguide Horns. *IEEE Journal of Quantum Electronics*, QE-13(10) : p828–835, 1977.

[36] I. Duport, P. Benech, D. Khalil and R. Rimet. Study of linear tapered waveguides made by ion exchange in glass. *Applied Physics Letters*, 82(9) : p1332–1334, 2003.

[37] H.W. Etzel, H.W. Gandy and R.J Gunther. Stimulated Emission of Infrared Radiation from Ytterbium Activated Silicate Glass. *Applied Optics*, 1(4) : p534–536, 1962.

[38] T.Y. Fan. Solid State Lasers: New Developments and Applications. *Plenum Press*, New York, 1993.

[39] S. Guy, C.L. Bonner, D.P. Shepherd, D.C. Hanna, A.C. Tropper and B. Ferrand. High-Inversion Densities in Nd:YAG: Upconversion and Bleaching. *IEEE Journal of Quantum Electronics*, 34(5) : p900–909, 1998.

[40] N.V. Nikonorov and G.T. Petrovskii. Ion-Exchanged Glasses in Integrated Optics: The Current State of Research and Prospects (A Review). *Glass Physics and Chemistry*, 25(1) : p16–54, 1999.

[41] L. DeShazer. Vanadate Crystals exploit diode pump technology. *Laser Focus World*, 30(2) : p88–93, 1984.

[42] A. Brignon, G. Feugnet, J.P. Huignard and J.P. Pochelle. Compact Nd:YAG and Nd:YVO_4 Amplifiers End-Pumped by a High-Brightness Stacked Array. *IEEE Journal of Quantum Electronics*, 34(3) : p577–585, 1998.

[43] X. Peng, L. Xu and A. Asundi. Power Scaling of Diode-Pumped Nd:YVO_4 Lasers. *IEEE Journal of Quantum Electronics*, 38(9) : p1291–1299, 2002.

[44] P.G. Shewmon. Diffusion in Solids. *McGraw-Hill*, Ch.1, New York, 1963.

[45] R.V. Ramaswamy and R. Srivastava. Ion-Exchanged Glass Waveguides: A Review. *Journal of Lightwave Technology*, 6(6) : p984–1001, 1987.

[46] T. Izawa and H. Nakagome. Optical waveguide formed by electrically induced migration of ions in glass plates. *Applied Physics Letters*, 21(12) : p584–586, 1972.

[47] G. Giallorenzi, E.J. West, R. Kirk, R. Ginther and R.A. Andrews. Optical Waveguides Formed by Thermal Migration of Ions in Glass. *Applied Optics*, 12(6) : p1240–1244, 1973.

[48] G.H. Chartier, P. Jassaud, A.D. de Oliveira and O. Parriaux. Fast fabrication method for thick and highly multimode optical waveguides. *Electronics Letters*, 13 : p763–764, 1977.

[49] V. Neuman, O. Parriaux and L.M. Walpita. Double-alkali effect: Influence of index profile of ion-exchanged waveguides. *Electronics Letters*, 15 : p704–705, 1979.

[50] G.H. Chartier, P. Jassaud, A.D. de Oliveira and O. Parriaux. Optical waveguides fabricated by electric-field controlled ion exchange in glass. *Electronics Letters*, 14(5) : p132–134, 1978.

[51] S.S. Geveorgyan. Single-step buried waveguides in glass by field-assisted copper ion-exchange. *Electronics Letters*, 26(1) : p38–39, 1990.

[52] A. Opilski, R. Rogozinski, M. Blahut, P. Karasinski, K. Gut and Z. Opilski. Technology of ion exchange in glass and its application in waveguide planar sensors. *Œ*, 36(6) : p1625–1638, 1997.

[53] R.V. Ramaswamy and S.I. Najafi. Planar, Buried, Ion-Exchanged Glass Waveguides: Diffusion Characteristics. *IEEE Journal of Quantum Electronics*, QE-22(6) : p883–891, 1986.

[54] C.B.E. Gawith, T.Bhutta, D.P. Shepherd, P. Hua, J. Wang, G.W. Ross and P.G.R. Smith. Buried laser waveguides in neodymium-doped BK-7 by K^+–Na^+ ion-exchange across a direct-bonded interface. *Applied Physics Letters*, 75(24) : p3757–3759, 1999.

[55] T. Bhutta. Novel Rare-Earth-Doped Planar Waveguide Lasers. *PhD. Thesis*, University of Southampton - Southampton, 2002.

[56] P.G. Suchoski, T.K. Findakly and F.J. Leonberger. Stable low-loss proton-exchanged $LiNbO_3$ waveguide devices with no electro-optic degradation. *Optics Letters*, 13(11), p1050–1052, 1988.

[57] J. Amin, M. Hempstead, J.E. Roman and J.S. Wilkinson. Tunable coupled-cavity waveguide laser at room temperature in Nd-diffused Ti:$LiNbO_3$. *Optics Letters*, 19(19), p1541–1543, 1994.

[58] J.K. Jones, J.P. de Sandro, M. Hempstead, D.P. Shepherd, A.C. Large, A.C. Tropper and J.S. Wilkinson. Channel waveguide laser at $1\mu m$ in Yb-indiffused $LiNbO_3$. *Optics Letters*, 20(13) : p1477–1479, 1995.

[59] R.V. Schmidt and I.P. Kaminow. Metal-diffused optical waveguides in LiNbO3. *Applied Physics Letters*, 25(8) : p458–460, 1974.

[60] I.P. Kaminow and J.R. Carruthers. Optical waveguiding layers in $LiNbO_3$ and $LiTaO_3$. *Applied Physics Letters*, 22(7) : p326–328, 1973.

[61] L.M.B. Hickey and J.S. Wilkinson. Titanium diffused waveguides in sapphire. *Electronics Letters*, 32(24) : p2238–2239, 1996.

[62] L.M.B. Hickey. Ti:sapphire waveguide laser by the thermal diffusion of Ti into sapphire. *PhD. Thesis*, University of Southampton - Southampton, 1998.

[63] M. Svalgaard, C.V. Poulsen, A. Bjarklev and O. Poulsen. Direct UV writing of buried singlemode channel waveguides in Ge-doped silica films. *Electronics Letters*, 30(17) : p1401–1403, 1994.

[64] G.D. Emmerson, S.P. Watts, C.B.E. Gawith, V. Albanis, M. Ibsen, R.B. Williams and P.G.R. Smith. Fabrication of directly UV-written channel waveguides with simultaneously defined integral Bragg gratings. *Electronics Letters*, 38(24) : p1531–1532, 2002.

[65] A.K. Mairaj, C. Rizotis, A.M. Chardon, P.G.R. Smith, D.P. Shepherd and D.W. Hewak. Development of channel waveguide lasers in Nd^{3+}-

doped chalcogenide (Ga:La:S) glass through photoinduced material modification. *Applied Physics Letters*, 81(20) : p3708–3710, 2002.

[66] J.P. Wittke. Thin-Film Lasers. *RCA Review*, 33 : p674–694, 1972.

[67] D.L. Lee. Electromagnetic Principles of Integrated Optics. *J. Wiley & Sons*, Ch.7, New York, 1986.

[68] B. Ferrand, B. Chambaz and M. Couchaud. Liquid phase epitaxy: A versatile technique for the development of miniature optical components in single crystal dielectric media. *Optical Materials*, 11 : p101–114, 1999.

[69] T. Bhutta, A.M. Chardon, D.P. Shepherd, E. Daran, C. Serrano and A. Munoz-Yague. Low Phonon Energy, Nd:LaF_3 Channel Waveguide Laser Fabricated by Molecular Beam Epitaxy. *IEEE Journal of Quantum Electronics*, 37(11) : p1469–1477, 2001.

[70] S.J. Barrington. Planar waveguide devices fabricated by pulsed laser deposition. *PhD. Thesis*, University of Southampton - Southampton, 2001.

[71] R.M. Almeida, P.J. Morais and A.C. Marques. Planar waveguides for integrated optics prepared by sol-gel methods. *Philosophical Magazine B*, 82(6) : p707–719, 2002.

[72] M. Kawachi, M. Yasu and T. Edahiro. Fabrication of SiO_2–TiO_2 Glass Planar Optical Waveguides by Flame Hydrolysis Deposition. *Electronics Letters*, 19(15) : p583–584, 1983.

[73] C.T.A. Brown, C.L. Bonner, T.J. Warbuton, D.P. Shepherd, A.C. Tropper and D.C. Hanna. Thermally bonded planar waveguide lasers. *Applied Physics Letters*, 71(9) : p1139–1141, 1997.

Chapter 2

Waveguide Laser Theory

2.1 Introduction

The following chapter details the two fundamental theories that govern the operation of waveguide lasers: electromagnetic theory and laser theory.

Knowledge of the number of propagating modes and their profile is of great importance to waveguide lasers, as the optical confinement offered by the waveguide geometry alters the modes available from those found within bulk lasers. Electromagnetic theory is applied to a planar asymmetric slab waveguide [1], which describes the general operation of the waveguides fabricated during this thesis. The theory is then extended to more accurately model the effects of graded index planar waveguides using the WKB method [2]. Modelling of uniform and graded index planar waveguides is completed to illustrate the effect of the refractive index profile on the guided modes.

Laser theory for a rare-earth doped laser is examined, following the rate equation based analysis of Fan [3] and Risk [4]. Relationships for the threshold power and slope efficiency are derived, and applied to end-pumped waveguide lasers.

2.2 Waveguide Modes

2.2.1 Electromagnetic Theory

Maxwell's equations are the starting point for determining the modal behaviour within any medium. Within an isotropic, source-free medium the electric (E) and magnetic (H) field vectors are related as follows [5]:

$$\nabla \times \underset{\sim}{E} = -\mu \frac{\partial}{\partial t} \underset{\sim}{H} \tag{2.1}$$

$$\nabla \times \underset{\sim}{H} = \varepsilon \frac{\partial}{\partial t} \underset{\sim}{E} \tag{2.2}$$

$$\nabla \cdot \underset{\sim}{E} = 0 \tag{2.3}$$

$$\nabla \cdot \underset{\sim}{H} = 0 \tag{2.4}$$

Where ∇ is the spatial vector operator, μ and ε are the permeability and permittivity of the medium and $\partial/\partial t$ is the partial derivative with respect to time t.

The equations are simplified by separating the temporal and spatial reliance of the fields, by assuming a time harmonic relation of the form:

$$\underset{\sim}{E}(\underset{\sim}{r}, t) = \underset{\sim}{E}(\underset{\sim}{r}) e^{i\omega t} \tag{2.5}$$

Where $\underset{\sim}{E}$ is a complex phasor, and describes only the spatial variation of the vector $(\underset{\sim}{E})$, $\underset{\sim}{r}$ is the position vector $(= x\hat{x} + y\hat{y} + z\hat{z})$, ω is the angular frequency of the field and $i = \sqrt{-1}$.

This allows equations 2.1–2.4 to be rewritten as follows:

$$\nabla \times \underset{\sim}{E} = -i\omega\mu \underset{\sim}{H} \tag{2.6}$$

$$\nabla \times \underline{H} = i\omega\varepsilon\underline{E} \tag{2.7}$$

$$\nabla \cdot \underline{E} = 0 \tag{2.8}$$

$$\nabla \cdot \underline{H} = 0 \tag{2.9}$$

Maxwell's curl equations (equations 2.6 and 2.7), in conjunction with the vector identity (where $\underline{U}$ is any vector):

$$\nabla \times \left(\nabla \times \underline{U}\right) = \nabla \left(\nabla \cdot \underline{U}\right) - \nabla^2 \underline{U} \tag{2.10}$$

allow the calculation of the homogenous wave equation, which relates the variation of the E-field in spatial and temporal dimensions, and allows calculation of the mode profiles within a waveguide:

$$\nabla^2 \underline{E} + \omega^2 \mu\varepsilon \underline{E} = 0 \tag{2.11}$$

The concept of duality is used during the following derivations, to reduce the volume of mathematics required. It has been shown [1] that due to the symmetry of Maxwell's equations, once a solution for one field has been calculated the solution for the other field is found by making the substitutions $E \rightarrow -H$, $H \rightarrow E$, $\mu \rightarrow \varepsilon$ and $\varepsilon \rightarrow \mu$.

2.2.2 Solution of the Wave Equation for an Asymmetric Waveguide

When detailing the methods used to solve Maxwell's equations for waveguide structures, it is common to begin with the symmetric slab waveguide. However, the solutions for this waveguide geometry will be omitted, as the waveguides produced during this thesis are of the asymmetric type. The field solutions for the asymmetric slab waveguide, once derived, are

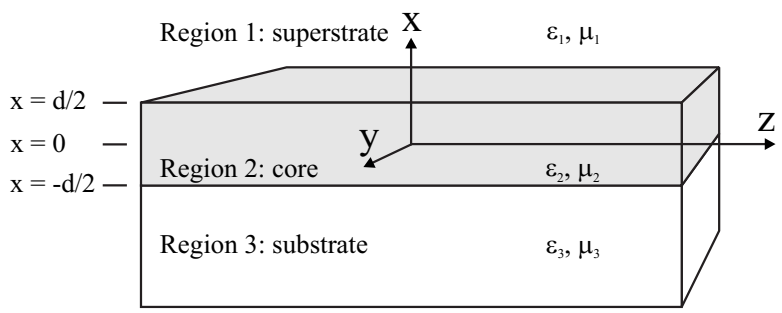

Figure 2.1: The asymmetric waveguide

generally applicable to all three layer waveguides and are readily converted to those required for the symmetric slab waveguide.

The asymmetric slab waveguide, which is assumed to extend infinitely in the y and z directions (figure 2.1), consists of three distinct regions:

1. The superstrate, which is often the surrounding atmosphere and is characterised by ε_1, μ_1
2. The core, characterised by ε_2, μ_2 and depth $= d$
3. The substrate, characterised by ε_3, μ_3

It is often more practical to refer to the refractive index of the waveguide regions, which is calculated via the permittivity of the region: $n_m = \sqrt{\varepsilon_m/\varepsilon_0}$, where ε_0 is the permittivity of free-space and m denotes the waveguide region. For guidance to occur the indices of the three regions must be chosen so that $n_2 > n_1, n_3$. The numerical aperture NA is also an important quantity when discussing waveguides, and is defined:

$$NA = \sin\theta = \sqrt{n_2^2 - n_1^2} \tag{2.12}$$

Where θ is the acceptance angle. The definition of θ is derived from ray optics, and is the angular limit to a ray launched into the waveguide, which will then experience guidance i.e. any rays launched into the waveguide at angles greater than the acceptance angle will not be guided and instead will be refracted out of the waveguide.

The boundary between the core and superstrate or substrate, negates TEM mode propagation within a waveguide structure [6]. Instead, there are two allowed polarisation states: transverse electric (TE) where the electric field is polarised in the y-direction ($E_x = E_z = 0$, $H_z \neq 0$) and transverse magnetic (TM) where the magnetic field is polarised in the y-direction ($H_x = H_z = 0$, $E_z \neq 0$). The quantities E_x, E_y, E_z, H_x, H_y, H_z are the projection of the complex phasors $\underset{\sim}{E}$ and $\underset{\sim}{H}$ onto the x, y and z axes respectively, and therefore do not require the under-bars in their notation.

2.2.2.1 TE Mode Solutions

The fields within the superstrate and substrate are assumed to decay exponentially with increasing distance from the core in the x-direction. Within the core the fields are assumed to have a standing-wave nature in the x-direction, and therefore to be oscillatory in nature. In the direction of propagation (z-direction) the fields are assumed to have a common wavevector, allowing the field solution to be expressed:

$$\underset{\sim}{E}(\underset{\sim}{r}, t) = \underset{\sim}{E}(\underset{\sim}{r})e^{i\omega t}e^{-ik_z z} = \underset{\sim}{E}(\underset{\sim}{r})e^{i(\omega t - k_z z)} \tag{2.13}$$

Where k_z is the wave vector in the z-direction.

Based upon the above assumptions, the proposed TE solutions are as follows:

$$E_y(x,z) = \left\{ \begin{array}{l} A_1 e^{-\alpha_1 x} \\ A_2 \cos\left(k_x x + \Psi\right) \\ A_3 e^{-\alpha_3 x} \end{array} \right\} e^{-ik_z z} \begin{array}{l} \\ \\ \\ \end{array} \begin{array}{l} x > d/2 \\ d/2 \geqslant x \geqslant -d/2 \\ x < -d/2 \end{array} \tag{2.14}$$

Where A_1–A_3 are the amplitude coefficients to the solutions in each region of the waveguide, α_1 and α_3 are the decay coefficients in regions 1 and 3, k_x is the transverse wave vector within the core and the constant Ψ denotes the nature of the mode symmetry, as modes within asymmetric waveguides are neither odd nor even.

Substituting each of the components of equation 2.14 into equation 2.11, allows calculation of the coefficients α_1, α_3 and k_x that satisfy the wave equation. These equations are named the dispersion relations and are of the form:

$$\alpha_1 = \sqrt{k_z^2 - \omega^2 \mu_1 \varepsilon_1} \tag{2.15}$$

$$\alpha_3 = \sqrt{k_z^2 - \omega^2 \mu_3 \varepsilon_3} \tag{2.16}$$

$$k_x = \sqrt{\omega^2 \mu_2 \varepsilon_2 - k_z^2} \tag{2.17}$$

It is a physical requirement that the E and H-fields must be continuous across the interfaces at $x = d/2, -d/2$. This is equivalent to requiring the tangential components of the fields to be equal at the interface. The tangential H-field is determined from Maxwell's curl equations:

$$H_z(x,z) = \frac{i}{\omega \mu_m} \frac{\partial}{\partial x} E_y(x,z) \tag{2.18}$$

The above equation is used to derive the z-component of the H-field within each region of the waveguide:

$$H_z(x,z) = \left\{ \begin{array}{l} \frac{-i\alpha_1}{\omega\mu_1} A_1 e^{-\alpha_1 x} \\ \frac{-ik_2}{\omega\mu_2} A_2 \cos\left(k_x x + \Psi\right) \\ \frac{i\alpha_3}{\omega\mu_3} A_3 e^{-\alpha_3 x} \end{array} \right\} e^{-ik_z z} \begin{array}{l} x > d/2 \\ d/2 \geqslant x \geqslant -d/2 \\ x < -d/2 \end{array} \tag{2.19}$$

The tangential fields for the interface at $x = d/2$ are as follows:

$$E_{\tan}: \; A_1 e^{-\frac{\alpha_1 d}{2}} = A_2 \cos\left(\frac{k_x d}{2} + \Psi\right) \tag{2.20}$$

$$H_{\tan}: \; \frac{-i\alpha_1}{\omega\mu_1} A_1 e^{-\frac{\alpha_1 d}{2}} = \frac{-ik_x}{\omega\mu_2} A_2 \sin\left(\frac{k_x d}{2} + \Psi\right) \tag{2.21}$$

Equation 2.14 can now be simplified using equation 2.20 to state the coefficient A_1 in terms of A_2. Similarly A_3 can be stated in terms of A_2 by manipulation of the tangential components at $x = -d/2$. The field components within each region can now be stated in relation to only the magnitude of the field component within the core:

$$E_y(x,z) = A_2 \left\{ \begin{array}{l} \cos\left(\frac{k_x d}{2} + \Psi\right) e^{-\alpha_1(x-d/2)} \\ \cos\left(k_x x + \Psi\right) \\ \cos\left(\frac{k_x d}{2} - \Psi\right) e^{\alpha_3(x+d/2)} \end{array} \right\} e^{-ik_z z} \begin{array}{l} x > d/2 \\ d/2 \geqslant x \geqslant -d/2 \\ x < -d/2 \end{array} \tag{2.22}$$

The guidance condition for the mode at $x = d/2$ is found by dividing 2.21 by 2.20, and after some manipulation this is stated as follows:

$$\frac{k_x d}{2} + \Psi = \tan^{-1}\left(\frac{\mu_2 \alpha_1}{\mu_1 k_x}\right) \tag{2.23}$$

And at $x = -d/2$:

$$\frac{k_x d}{2} - \Psi = \tan^{-1}\left(\frac{\mu_2 \alpha_3}{\mu_3 k_x}\right) \tag{2.24}$$

These guidance conditions are combined additively to remove the Ψ term to produce the full guidance condition:

$$2k_x d - \varphi_1^{TE} - \varphi_3^{TE} = 2p\pi \tag{2.25}$$

Where $p = 0, 1, 2, ...$ is the mode number and:

$$\varphi_m^{TE} = 2\tan^{-1}\left(\frac{\mu_2 \alpha_m}{\mu_m k_x}\right) \tag{2.26}$$

Where m denotes either region 1 or 3.

The terms φ_1 and φ_3 are the phase changes due to reflection at the superstrate/core and core/substrate interfaces, whereas the term $2k_x d$ is the phase change due to propagation. Taking this into account, the guidance

condition can be physically explained as a statement that the net phase change of a guided mode over one round-trip within the core, must equal an integer multiple of 2π.

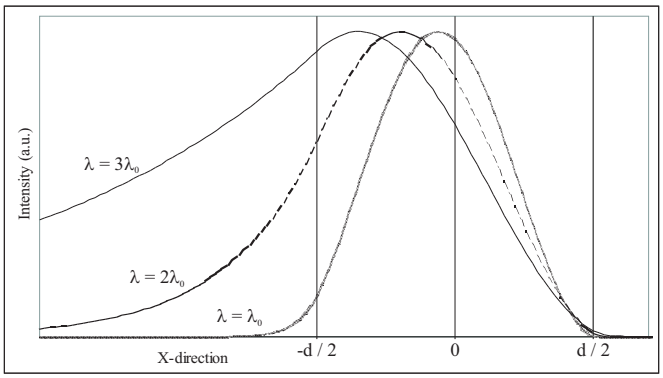

Figure 2.2: TE guided mode profile of fundamental mode for arbitrary λ_0

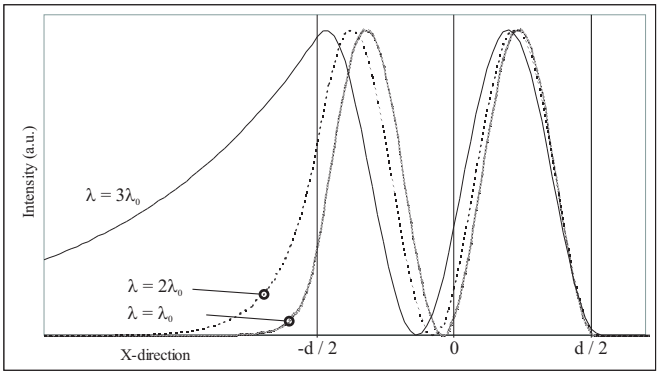

Figure 2.3: TE guided mode profile of first higher order mode for arbitrary λ_0

For illustrative purposes, figures 2.2 and 2.3 show the evolution of the first two TE guided modes with increasing wavelength, and arbitrary values of λ_0, d, n_1, n_2 and n_3. The modes are normalised so that each profile contains equal power. Increasing the wavelength of the guided wave reduces the number of propagating modes, which is equivalent to decreasing the numerical aperture ($NA = \sqrt{n_2^2 - n_1^2}$), or decreasing the depth of the waveguide. The effect of the asymmetric waveguide can be seen by the shift of the peak intensity towards the substrate. Increasing the wavelength of the field reduces the confinement of the mode within the core. The effect of

this increase in wavelength can be seen in the figure by the increasing penetration of the mode 'wings' into the substrate. An increase in wavelength beyond the $3\lambda_0$ shown, with this particular model caused cut-off of the 1^{st} higher order mode.

2.2.2.2 TM Mode Solutions

The TM mode solutions are derived by the direct use of duality, producing:

$$H_y(x,z) = A_2 \begin{Bmatrix} \cos\left(\frac{k_x d}{2} + \Psi'\right) e^{-\alpha_1(x-d/2)} \\ \cos\left(k_x x + \Psi'\right) \\ \cos\left(\frac{k_x d}{2} - \Psi'\right) e^{\alpha_3(x+d/2)} \end{Bmatrix} e^{-ik_z z} \begin{matrix} x > d/2 \\ d/2 \geqslant x \geqslant -d/2 \\ x < -d/2 \end{matrix} \tag{2.27}$$

With guidance condition:

$$2k_x d - \varphi_1^{TM} - \varphi_3^{TM} = 2p\pi \tag{2.28}$$

Where:

$$\varphi_m^{TM} = 2\tan^{-1}\left(\frac{\varepsilon_2 \alpha_m}{\varepsilon_m k_x}\right) \tag{2.29}$$

2.3 Modes in Waveguides with x-Dependent Refractive Index

The previous analysis of an asymmetric waveguide with a uniform core refractive index can be altered to determine the modal characteristics of waveguides with a depth dependant index. Waveguides produced by ion exchange or indiffusion (chapters 4 and 6) exhibit a depth dependant core refractive index $n_2 = n(x)$, with a maximum index n_s at the surface that gradually reduces to the substrate index n_{sub} over the depth of the core (figure 2.4). The shape of the core index profile is dependent on fabrication conditions [7].

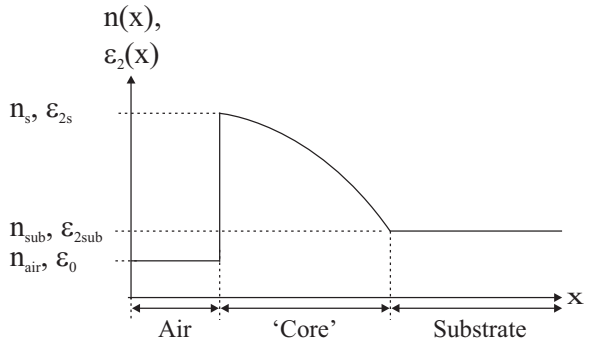

Figure 2.4: Refractive index/permittivity profile of a graded index waveguide

The variation in index is due to variation of the core permittivity, which must be taken into account in the field solutions. The refractive index of the core region is related to the permittivity through the following equation:

$$n(x) = \sqrt{\frac{\varepsilon_2(x)}{\varepsilon_0}} \tag{2.30}$$

The graded index causes some difficulties in solving Maxwell's equations, due to the unclear boundaries of the 'core' region. The WKB method can be used to calculate the number of modes and the effective indices of each mode within a graded index planar waveguide, with any index profile [1, 2]. WKB analysis of planar waveguides is described here to allow physical insight into the operation of graded-index planar waveguides. More complex tapered waveguide structures are analysed using beam propagation software in chapter 3.

2.3.1 The WKB Method

The form of the waveguides produced during this thesis is shown in figure 2.5. The core is defined as the region of high refractive index between the boundaries X_a and X_b. The mode behaviour in this core region is assumed to be similar to that within the asymmetric slab waveguide. Once the boundaries to the graded-index core are identified, it can be expected that

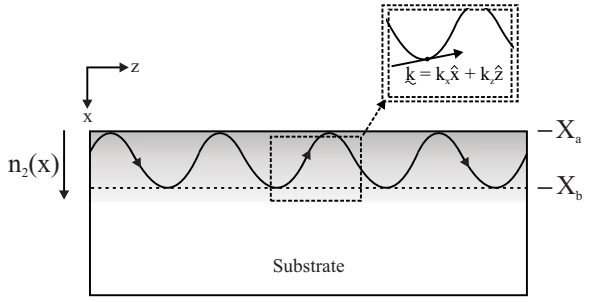

Figure 2.5: Ray path through a graded index asymmetric waveguide

the nature of the fields should be oscillatory within the core, and should decay exponentially on either side of the boundaries.

A mode within the core is related to a wavevector $\underset{\sim}{k}(x)$, which is found by rearranging equation 2.17, taking into account the x-dependence of the permittivity within the core:

$$\underset{\sim}{k}^2(x) = k_x^2(x)\hat{x} + k_z^2\hat{z} = \omega^2\mu_2\varepsilon_2(x) \tag{2.31}$$

Where $k_x(x)$ and k_z are the projections of the wavevector onto the x and z axes respectively.

Equation 2.31 can be rearranged to allow calculation of the wave vector in the x-direction:

$$k_x(x) = k_0\sqrt{n^2(x) - n_{eff}^2} \tag{2.32}$$

Where $k_0 = \omega\sqrt{\mu_0\varepsilon_0}$, $n_{eff} = k_z/k_0 = (\varepsilon_{eff}/\varepsilon_0)^{1/2}$ is the effective refractive index and ε_{eff} is the effective permittivity experienced by the guided mode.

The effective index is defined as being equal to the index at the point where:

$$k_x(x) = k_x(X_a) = k_x(X_b) = 0 \tag{2.33}$$

Hence:

$$n(X_a) = n(X_b) = n_{eff} \tag{2.34}$$

Physically, at depths X_a and X_b, $\underset{\sim}{k}(x)$ is parallel to the z-axis. Mathematically, these points are known as the turning points.

The previously derived guidance condition for an asymmetric slab waveguide is as follows:

$$2k_x d - \varphi_1 - \varphi_3 = 2p\pi \tag{2.35}$$

The equation states that for a guided mode the net phase shift in the x-direction must equal a multiple of 2π. The first term in equation 2.35 is the contribution to the overall phase change due to propagation within the waveguide. This value is altered for a graded index waveguide, as the value of k_x is dependent on x, which is accounted for by integrating with respect to x [1]:

$$2\int_{X_a}^{X_b} k_x(x)dx - \varphi_1 - \varphi_3 = 2p\pi \tag{2.36}$$

To solve equation 2.36, the turning points must be determined. For graded index waveguides with a maximum refractive index at the surface the first turning point X_a can be set to zero [2], and the problem is reduced to finding the turning point X_b.

It is possible to make further simplifications by inspecting the equations for φ_1 and φ_3 [2]. Firstly, at the core/air interface the phase of the TE mode is determined from equation 2.26:

$$\varphi_1^{TE} = 2\tan^{-1}\left(\frac{\mu_2\alpha_1}{\mu_1 k_x(x)}\right) \tag{2.37}$$

Expanding the terms in the above equation, using the dispersion equations 2.15 to 2.17, produces:

$$\varphi_1^{TE} = 2\tan^{-1}\left(\sqrt{\frac{k_z^2 - k_1^2}{k_2^2(x) - k_z^2}}\right) \tag{2.38}$$

Where it has been assumed that $\mu_1 = \mu_2$.

The above equation can be manipulated to take into account the refractive indices of the materials through the identities [1]:

$$\begin{aligned} n_1 &= \frac{k_1}{k_0} \\ n_2(x) &= \frac{k_2(x)}{k_0} \\ n_{eff} &= \frac{k_z}{k_0} \end{aligned} \tag{2.39}$$

After some manipulation using equations 2.39, equation 2.38 becomes:

$$\varphi_1^{TE} = 2\tan^{-1}\left(\sqrt{\frac{n_{eff}^2 - n_1^2}{n_2^2(x) - n_{eff}^2}}\right) \tag{2.40}$$

If the core of the waveguide was dissected laterally into very thin slices so that the refractive index varies negligibly through each slice, then the phase change at the surface of the waveguide can be stated:

$$\varphi_1^{TE} = 2\tan^{-1}\left(\sqrt{\frac{n_{eff}^2 - n_1^2}{n_{surface}^2 - n_{eff}^2}}\right) \tag{2.41}$$

Where $n_{surface}$ is the refractive index of the core at the top surface of the waveguide.

An identical method is used to find the TM phase change at the surface of the waveguide, which produces:

$$\varphi_1^{TM} = 2\tan^{-1}\left(\frac{n_{surface}^2}{n_1^2}\sqrt{\frac{n_{eff}^2 - n_1^2}{n_{surface}^2 - n_{eff}^2}}\right) \tag{2.42}$$

The change in refractive index Δn produced by the ion exchange and in-diffusion methods, as used during this thesis, is small (typically in the

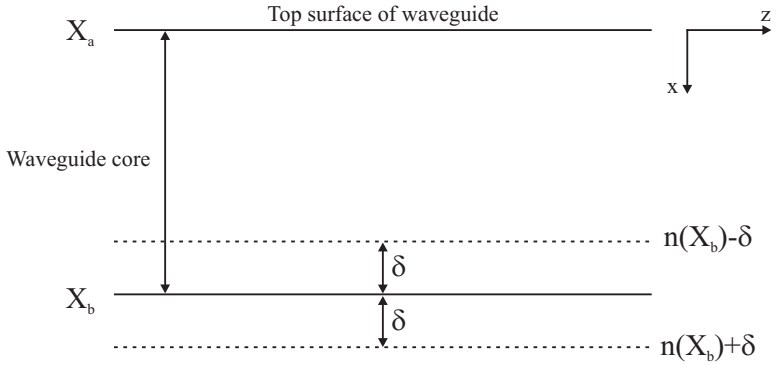

Figure 2.6: The refractive index of a graded index waveguide near the lower turning point X_b

order of 10^-3). Hence, $\Delta n \ll n_3$ and therefore n_{eff}^2 is very close to the value of $n_{surface}^2$, and both are $\gg 1$. For this reason, a waveguide in air (i.e. $n_1 = 1$) would produce a phase change at the top surface of the waveguide of $\varphi_1 \approx \pi$ for both TE and TM modes.

A similar method is used to calculate the phase change at the core/substrate interface, situated at the depth X_b. As with the previous derivation the core is divided laterally into thin sections. The refractive index at the depth X_b is defined as $n(X_b) = n_{eff}$. The refractive index a small distance δ above and below the core, as shown in figure 2.6, can be stated:

$$\begin{aligned} n(X_b - \delta) &= n(X_b) - \delta\frac{\partial n(X_b)}{\partial x} = n_{eff} - \delta\frac{\partial n(X_b)}{\partial x} \\ n(X_b + \delta) &= n(X_b) + \delta\frac{\partial n(X_b)}{\partial x} = n_{eff} + \delta\frac{\partial n(X_b)}{\partial x} \end{aligned} \tag{2.43}$$

Allowing the phase change at the point X_b to be stated for TE modes as:

$$\varphi_3^{TE} = 2\tan^{-1}\left(\sqrt{\frac{n_{eff}^2 - n^2(X_b + \delta)}{n^2(X_b - \delta) - n_{eff}^2}}\right) \tag{2.44}$$

The above equation taken in the limit that $\delta \to 0$ becomes:

$$\varphi_3^{TE} = 2\tan^{-1}(0) \tag{2.45}$$

and hence, $\varphi_3^{TE} = \pi/2$.

An identical method is used to derive the phase change at the core/substrate interface for TM modes, which produces $\varphi_3^{TM} = \pi/2$.

These assumptions remove the distinction between TE and TM modes, but allow the trends in the effective refractive index to be calculated. Substituting equation 2.32 into 2.36, and using the previous simplifications produces:

$$2\int_0^{X_b} k_0\sqrt{n^2(x) - n^2(X_b)}dx - \left(2p + \frac{3}{2}\right)\pi = 0 \tag{2.46}$$

Computer modelling software allows this equation to be solved for each mode p using an iterative technique.

2.3.2 Application of the WKB Method to Ion Exchange and Indiffusion Profiles

The following section utilises the WKB method to model the graded index waveguides produced in the following chapters. Waveguides produced by ion exchange and indiffusion are fundamentally linked by their reliance on the diffusion of a foreign species into a host substrate, which produces an increase in refractive index and therefore the guiding layer. As will be discussed in chapter 6 there are two limits to the diffusion process: the first is that of an infinite diffusion source, this models the behaviour of both a thermal ion exchange process (chapter 4) and an indiffusion which occurs from a source that is not fully depleted (section 6.3.1.1). The refractive index profile follows a complementary error function (erfc) distribution [7]:

$$n(x) = n_3 + \Delta n\ erfc\left(\frac{x}{W}\right) \tag{2.47}$$

Where n_3 is the substrate refractive index, Δn is the maximum change in refractive index, which occurs at the surface and is constant for all effective diffusion depths W. The effective diffusion depth is found when the refractive index of the waveguide falls to erfc(1) of its original value.

The other limit to the diffusion process is that of the instantaneous diffusion, which applies to indiffusions where the source is fully depleted (section 6.3.1.2). This diffusion can be modelled with a Gaussian distribution [7]:

$$n(x) = n_{sub} + \frac{n_{tot}}{\sqrt{\pi}W} \exp\left(-\frac{x^2}{W^2}\right) \tag{2.48}$$

Where n_{tot} is a constant defining the area under the refractive index profile (and is measured in units of index·depth), and W is the effective diffusion depth defined at the e^{-1} point. The maximum refractive index occurs at the surface of the waveguide, but unlike the infinite diffusion the surface index is not constant and is instead a function of n_{tot} and W. For this reason waveguides fabricated with identical values of n_{tot}, at different effective diffusion depths will exhibit different values of surface index.

Equations 2.47 or 2.48 can now be substituted into equation 2.46, and the values of the turning point X_b can be calculated. The value X_b gives the penetration of the mode into the depth of the diffused waveguide. Each successively higher order mode penetrates deeper into the waveguide until it experiences an effective index equal to that of the substrate, at this point the mode is said to be cut-off. The penetration of modes into a diffused waveguide is shown diagrammatically in figure 2.7, for an arbitrary diffusion modelled from equation 2.48, where $\Delta n = n(x) - n_3$.

Once the core boundaries X_a and X_b have been determined, the model can be altered to allow the effective index to be calculated over various effective diffusion depths. In this way the optimum depth of a waveguide that supports a desired number of modes can be calculated. Figures 2.8 and 2.9 show the first six modes supported by a graded index waveguide based upon equations 2.47 and 2.48 respectively, where $\Delta n_{eff} = n_{eff} - n_3$.

For comparison purposes, figure 2.10 shows the first six modes supported by an asymmetric slab waveguide, which were calculated directly from the guidance condition (equation 2.25).

The profiles were calculated using a value of $n_3 = 1.50669$, which corre-

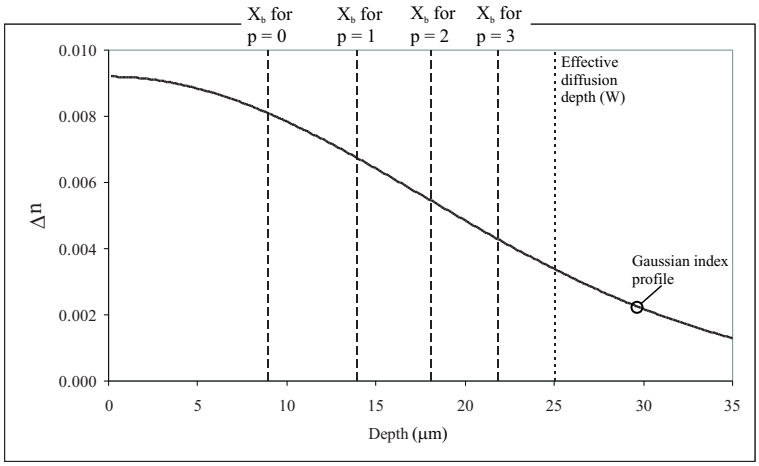

Figure 2.7: Diagrammatic representation of the X_b turning points for successively higher order modes, in a Gaussian shaped graded index waveguide

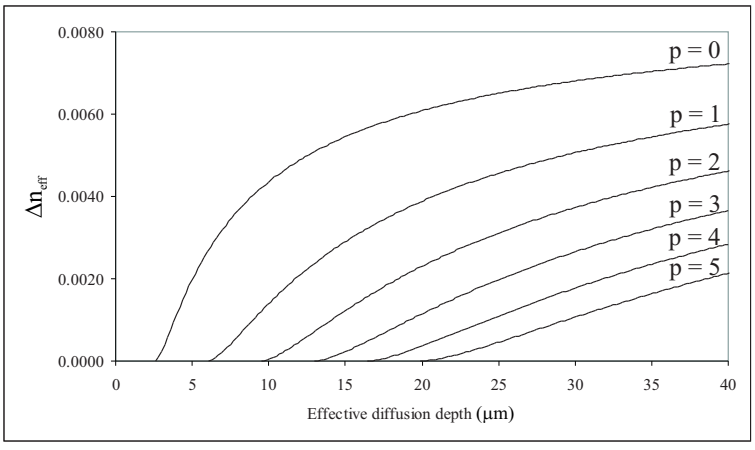

Figure 2.8: Effective index and allowed modes within a complementary error function, graded index waveguide.

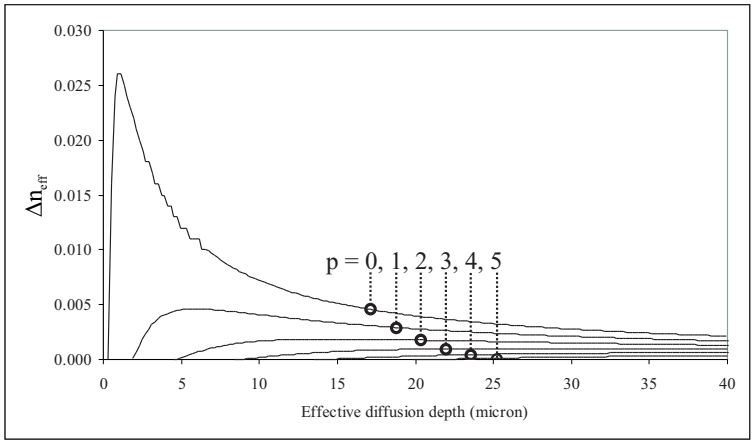

Figure 2.9: Effective index and allowed modes within a Gaussian graded index waveguide.

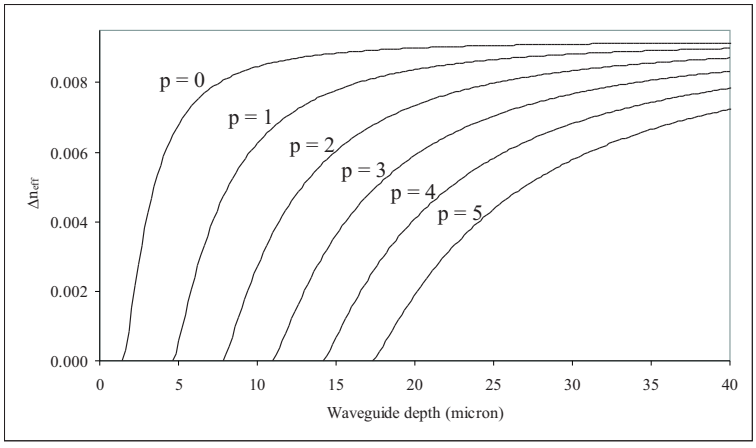

Figure 2.10: Effective index and allowed modes within an asymmetric slab waveguide.

sponds to $1.06\mu m$ radiation propagating in BK7 glass, the substrate material used in the majority of this thesis. Refractive index values of this accuracy (i.e. 10^{-5}) are determined by the glass manufacturer, Schott, using a prism goniometer technique. A surface index of $n_s = 1.51589$ was chosen for the erfc profile, which corresponds to the measured surface index of a waveguide produced by potassium-sodium ion exchange [8]. To allow comparison of the effect of a graded index waveguide, the core index of the slab waveguide was chosen to be equal to this value (i.e. $n_2 = 1.51589$). A value $n_{tot} = 1.761 \times 10^{-7}$ was chosen for the Gaussian profile, as this allowed the waveguide to support 6 modes, offering fair comparison with the previous profiles.

The profiles generated for the diffused waveguides agree with previous analysis [2]. The main difference between the profiles is that a diffusion that follows an erfc profile will support an increasing number of modes as the depth is increased, due to the constant surface index. Diffusions which follow a Gaussian profile are limited in the number of modes that will be supported. The value n_{tot} is finite, and as the depth increases the surface index decreases until the core index is almost identical to the substrate index and the mode becomes that of a bulk laser.

2.4 Laser Theory

2.4.1 Introduction

The following chapter describes the theoretical laser operation of a rare earth (RE) doped waveguide laser. The operation of these lasers is described by the quasi-three-level model originally described by Fan [3]. The quasi-three level model is a powerful tool for describing laser operation as it is inherently applicable to three and four-level laser transitions and accounts for the spatial distribution of the pump and laser fields.

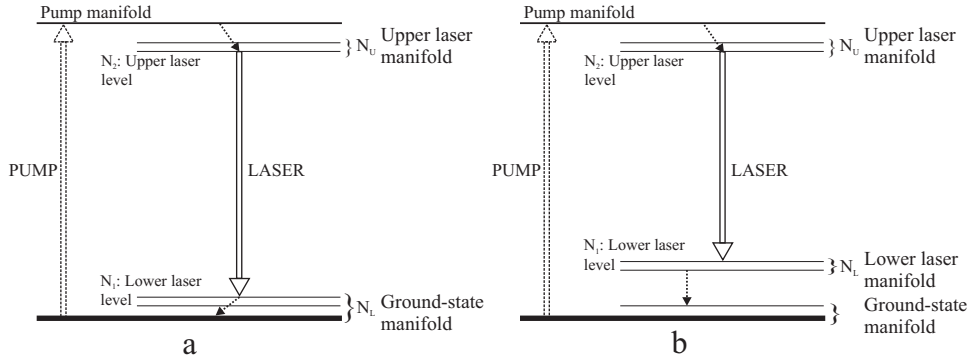

Figure 2.11: Idealised energy levels of: a/ quasi-three-level laser, b/ four-level laser

2.4.2 Quasi-Three Level Laser Operation

The laser ions studied within this thesis are all related to the idealised quasi-three-level and four-level energy level diagrams shown in figure 2.11. Laser action is described by this model as follows: an ion is excited from the ground-state to the pump manifold by absorption of a pump photon, the excited ion then decays non-radiatively to the upper laser level N_2, which is one of the stark levels of the upper laser manifold. The ion undergoes stimulated emission between this level and the lower laser level N_1, which is a stark level of the lower laser manifold.

Due to the rapid non-radiative decay between the stark split levels, the populations of each stark level within a manifold are said to be in quasi-thermal equilibrium, and therefore can be modelled with a Boltzmann distribution [9].

The population densities of the upper laser level N_2 and the lower laser level N_1 are denoted [4]:

$$\begin{aligned} N_1 &= f_1 N_L \\ N_2 &= f_2 N_U \end{aligned} \tag{2.49}$$

Where N_L and N_U are the total population densities of the lower and upper laser manifolds respectively, and f_1 and f_2 are the fractions of the total population within the appropriate stark level of the lower and upper laser

manifold respectively.

The quasi-three-level theory is applied to a four level laser by assuming that the lower laser level is unpopulated (i.e. $N_U = N_1 = 0$), which can only practically occur if the lower laser level is not part of the ground-state manifold.

The following assumptions are made to allow analysis: the energy gap between the upper and lower laser level is assumed to be large enough that in equilibrium (i.e. no pumping), the upper laser level is unpopulated (i.e. $N_U^0 = N_2^0 = 0$) and the lower laser level population is described by $N_1^0 = f_1 N_L^0$. The superscript is used to denote the equilibrium values of the population. Spatial hole burning is neglected, and it is assumed that there is negligible depopulation of the ground state.

A rate equation approach is used to describe the change in population with respect to time t. The upper and lower laser level population densities are described by [4]:

$$\frac{dN_2(x,y,z)}{dt} = f_2 Rr(x,y,z) - \frac{N_2(x,y,z) - N_2^0}{\tau} - \frac{f_2 c\sigma \left(N_2(x,y,z) - N_1(x,y,z)\right)}{n}\Phi\phi(x,y,z) = 0 \tag{2.50}$$

$$\frac{dN_1(x,y,z)}{dt} = -f_1 Rr(x,y,z) - \frac{N_1(x,y,z) - N_1^0}{\tau} + \frac{f_1 c\sigma \left(N_2(x,y,z) - N_1(x,y,z)\right)}{n}\Phi\phi(x,y,z) = 0 \tag{2.51}$$

These equations can be combined to describe population inversion density ΔN using: $\Delta N = N_2 - N_1$:

$$\frac{d\Delta N(x,y,z)}{dt} = (f_1+f_2)\,Rr(x,y,z) - \frac{\Delta N(x,y,z)-\Delta N^0}{\tau} - \frac{(f_1+f_2)\,c\sigma\Delta N(x,y,z)}{n}\Phi\phi(x,y,z) = 0 \tag{2.52}$$

Where $\Delta N^0 = N_2^0 - N_1^0$ is the unpumped population inversion, τ is the upper laser level lifetime, c is the speed of light in a vacuum, σ is the stimulated emission cross-section and n is the refractive index of the gain medium. R is the pump rate, defined as:

$$R = \frac{P_p\left(1-e^{-\alpha_p l}\right)}{h\nu_p} \tag{2.53}$$

Where P_p is the incident pump power, $h\nu_p$ is the pump photon energy and the quantity $1-e^{-\alpha_p l}$ is the fraction of pump energy absorbed in a gain medium of length l with absorption coefficient α_p.

The total number of laser photons Φ in the cavity, ignoring any cavity loss, is given by:

$$\Phi = \frac{2nlP_L}{ch\nu_L} \tag{2.54}$$

Where $h\nu_L$ is the laser photon energy and P_L is the laser power travelling in one direction, hence the inclusion of 2 in the equation.

The quantities $r(x,y,z)$ and $\phi(x,y,z)$ are the spatial distributions of the pump and laser energy, which are normalised as follows:

$$\iiint\limits_{cavity} r(x,y,z)dxdydz = 1,\ \iiint\limits_{cavity} \phi(x,y,z)dxdydz = 1 \tag{2.55}$$

The evolution of the number of photons in the cavity with time can be expressed [4]:

$$\frac{d\Phi}{dt} = \frac{c\sigma}{n}\iiint\limits_{cavity} \Delta N(x,y,z)\Phi\phi(x,y,z)dxdydz - \frac{\Phi}{\tau_c} = 0 \tag{2.56}$$

Where $\tau_c = 2nl/c\delta$ is the cold cavity lifetime and δ is the fractional round-trip loss.

Rearranging equation 2.56 and taking into consideration the condition for laser operation, which is that the round-trip gain G must be equal to the round-trip loss δ [4], produces:

$$G = 2\sigma l \iiint_{cavity} \Delta N(x,y,z)\phi(x,y,z)dxdydz = \delta \tag{2.57}$$

The round-trip loss $\delta = L - \ln R$ is the sum of the 'useful' losses due to transmission through an output coupler with reflectivity R (where the transmission T can be stated $T = -\ln R$ for small values of R), and the loss due to propagation losses in the gain medium L. A statement of the population inversion density can be found by rearranging equation 2.52. The following statements are made to simplify the equation: $f = f_1 + f_2$, and the assumption is made that $\Delta N^0 = -N_1^0$ as in thermal equilibrium $N_1^0 \gg N_2^0$, the equation becomes:

$$\Delta N(x,y,z) = \frac{f\tau R r(x,y,z) - N_1^0}{1 + \frac{f\tau c\sigma}{n}\Phi\phi(x,y,z)} \tag{2.58}$$

The above equation is substituted into equation 2.57 and can be expressed in terms of input and output powers by substituting equations 2.53 and 2.54, and stating that the output power $P_{out} = TP_L$:

$$2\sigma l \int_0^l \int_{-\infty}^{\infty}\int_{-\infty}^{\infty} \frac{\frac{f\tau}{h\nu_p}P_P\eta_{abs}r(x,y,z) - N_1^0}{1 + 2l\frac{P_{out}}{TI_{sat}}\phi(x,y,z)}\phi(x,y,z)dxdydz = L + T \tag{2.59}$$

Where $\eta_{abs} = 1 - e^{-\alpha_p l}$ and $I_{sat} = (h\nu_L)/(f\sigma\tau)$ [4].

Equation 2.59 is the key equation governing laser behaviour above threshold, which relates the physical parameters of the laser ion to the input and output power. The power required to reach threshold P_{th} can be calculated directly by setting $P_{out} = 0$ and $P_P = P_{th}$ [10]:

$$P_{th} = \frac{h\nu_p}{2\sigma l f \tau \eta_{abs}} \left(L + T + 2\sigma l N_1^0\right) \left[\int_0^l \int_{-\infty}^{\infty} \int_{-\infty}^{\infty} r(x,y,z)\phi(x,y,z)dxdydz\right]^{-1} \tag{2.60}$$

highlighting the additional loss suffered by lasers that exhibit reabsorption loss, which is equal to $2\sigma l N_1^0$.

2.4.3 Application to Waveguide Lasers

In the previous analysis of laser operation, the terms that describe the pump and laser distributions were not expanded. The following analysis uses Gaussian distributions to model the behaviour of fundamental pump and laser modes within a waveguide laser. The pump and laser distributions can be expressed as [4]:

$$r(x,y,z) = \frac{2\alpha_P}{\pi \eta_{abs} \omega_{Px} \omega_{Py}} e^{\left(-\frac{2x^2}{\omega_{Px}^2}\right)} e^{\left(-\frac{2y^2}{\omega_{Py}^2}\right)} e^{-\alpha_P z} \tag{2.61}$$

$$\phi(x,y,z) = \frac{2}{\pi \omega_{Lx} \omega_{Ly} l} e^{\left(-\frac{2x^2}{\omega_{Lx}^2}\right)} e^{\left(-\frac{2y^2}{\omega_{Ly}^2}\right)} \tag{2.62}$$

Where ω_{nx} and ω_{ny} are the spot sizes in the x and $y-$directions respectively, and the subscript $n = P$ or L, denotes the pump or laser mode. As the fundamental mode is being considered in this analysis it is possible to use the $1/e^2$ definition of spot size. Substituting the pump and laser distributions into equation 2.60 and integrating, produces:

$$P_{th} = \frac{\pi h\nu_p}{4\sigma f \tau \eta_{abs}} \left(L + T + 2\sigma l N_1^0\right) \sqrt{\omega_{Px}^2 + \omega_{Lx}^2} \sqrt{\omega_{Py}^2 + \omega_{Ly}^2} \tag{2.63}$$

The above equation is identical to that calculated for a four-level laser transition [11], with the addition of the re-absorption loss caused by the population of the lower laser level.

Equation 2.63 indicates that to reduce the threshold power for a given laser transition, the pump and laser spot sizes must be as small as possible, which is an inherent ability of waveguide devices. The propagation loss must also be minimised, which requires careful fabrication and the use of low-loss waveguide fabrication techniques. Minimising the propagation loss is fundamental to efficient operation of four-level lasers, but its importance is reduced with quasi-three-level lasers where the reabsorption loss is usually dominant. A less practical method for reduction of the threshold power is to cool the laser, which reduces the lower laser level population and hence the extra loss term. Cooling was once necessary to achieve lasing with some quasi-three-level lasers before the advent of better spectrally matched pump sources [9].

The slope efficiency η_{SE} of a laser transition indicates the conversion efficiency of pump power to laser power, and with a quasi-three-level laser is determined by numerically evaluating r and ϕ at various input and output powers. A definite formula can be expressed for the four-level laser [11], under the assumptions of low power operation and non-divergent pump and laser modes within the waveguide:

$$\eta_{SE} = \frac{\nu_L}{\nu_P} \frac{T}{L+T} \eta_{abs} \eta_q \eta_{PL} \tag{2.64}$$

Where η_{PL} is a term which describes the overlap of the pump and laser modes:

$$\eta_{PL} = \frac{\omega_{Lx}\omega_{Ly}\sqrt{2\omega_{Px}^2 + \omega_{Lx}^2}\sqrt{2\omega_{Py}^2 + \omega_{Ly}^2}}{\left(\omega_{Px}^2 + \omega_{Lx}^2\right)\left(\omega_{Py}^2 + \omega_{Ly}^2\right)} \tag{2.65}$$

Maximum slope efficiency for a given laser transition is created by minimising the propagation loss, and where possible, reducing the pump spot size below the laser spot size, which minimises η_{PL}. As the pump has a lower wavelength than the laser, the pump mode within a waveguide is smaller or nearly equivalent in size to the laser mode, leading to a good overlap ($\eta_{PL} \approx 0.75$), which indicates the necessity to reduce the propagation loss with this type of laser device. An increase of the slope efficiency

is possible by increasing the transmittance of the output coupler, however, as can be seen from equation 2.63 this also increases the threshold power. For this reason an optimum transmittance must be found to achieve the highest slope efficiency with a reasonable threshold power.

2.5 Summary

The basic theory that determines the modal properties of a planar, asymmetric waveguide has been derived. The theory is not directly applicable to tapered waveguides, as the lateral guidance afforded by this design is not accounted for, which may lead to the conclusion that the theory is extraneous. However, the basic planar, asymmetric waveguide theory lays the foundations for further study, especially that of the WKB method (section 5.2.1) and the theory that determines prism coupling (sections 5.7.2 and 6.6.8). WKB analysis is particularly useful when studying waveguides produced by diffusion-based fabrication techniques, as these methods produce graded index waveguides. WKB analysis of ion exchanged waveguides is completed more thoroughly in section 5.2.1, where it is used to gain insight into the pump and laser mode overlap of waveguide lasers produced by thermal ion exchange.

The basic waveguide theory derived in this section is not extendable to the three-dimensional variations found in the tapered waveguide design. For this reason the next chapter will model tapered waveguides using the beam propagation method (BPM). BPM allows complex waveguides to be analysed, and in this way is more directly applicable to the tapered waveguide.

Basic laser theory has been derived, and has focussed on the derivation of the slope efficiency and threshold power of a quasi-three-level laser. Derivation of quasi-three-level laser theory is vitally important to the later work with the Yb^{3+} ion (section 4.6.3), and can be manipulated to describe the operation of four-level lasers such as the Nd^{3+} ion. The basic laser theory was extended to account for the guidance afforded by the waveguide geometry. The equations derived for the slope efficiency and threshold

power are used extensively throughout chapters 4 and 5. These formulae are used to check for correct operation of the waveguide lasers, to determine the propagation loss of the waveguides, and are extended to allow calculation of the taper loss.

2.6 References

[1] D.L. Lee. Electromagnetic Principles of Integrated Optics. *J. Wiley & Sons*, New York, Ch.2, 1986.

[2] G.B. Hocker and W.K. Burns. Modes in Diffused Optical Waveguides of Arbitrary Index Profile. *IEEE Journal of Quantum Electronics*, QE-11(6) : p270–276, 1974.

[3] T.Y. Fan and R.L. Byer. Modelling and CW Operation of a Quasi-Three-Level 946nm Nd:YAG Laser. *IEEE Journal of Quantum Electronics*, QE-23(5) : p605–612, 1987.

[4] W.P. Risk. Modelling of longitudinally pumped solid state lasers exhibiting reabsorption losses. *Journal of the Optical Society of America B*, 5(7) : p1412–1423, 1988.

[5] F.H. Read. Electromagnetic Radiation. *J. Wiley & Sons*, New York, 1980.

[6] A. Tropper. Fibre and waveguide lasers. *Proceedings of the 52nd Scottish Universities Summer School in Physics*, p39–59, 1998.

[7] P.G. Shewmon. Diffusion in Solids. *McGraw-Hill*, New York, 1963.

[8] R.V. Ramaswamy and R. Srivastava. Ion-Exchanged Glass Waveguides: A Review. *Journal of Lightwave Technology*, 6(6) : p984–1001, 1987.

[9] T.Y. Fan. Solid State Lasers: New Developments and Applications. *Plenum Press*, New York, 1993.

[10] T. Taira, W.M. Tulloch and R.L. Byer. Modelling of quasi-three-level lasers and operation of cw Yb:YAG lasers. *Applied Optics*, 36(9) : p1867–1874, 1997.

[11] W.A. Clarkson and D.C. Hanna. Effects of transverse-mode profile on slope efficiency and relaxation oscillations in a longitudinally-pumped laser. *Journal of Modern Optics*, 36(4) : p483–498, 1989.

Chapter 3

The Tapered Waveguide

3.1 Introduction

High-power, single-spatial-mode, waveguide lasers suffer from contradictory geometrical requirements. High output powers are most efficiently accessed with the use of diode-bar lasers as the pump source [1], which requires a broad planar waveguide to achieve reasonable coupling efficiency. Whereas single spatial-mode operation is gained, most simply, through the two-dimensional confinement offered by the channel geometry [2].

Unstable resonators [1, 3] have been used to gain high coupling efficiency from a diode-bar pumped, planar waveguide laser, and near single-spatial-mode output. However, these resonators require curved mirrors, which in the waveguide geometry requires either a non-monolithic design or complex end-face polishing. A more straightforward, monolithic solution is to attempt to gain the advantages of both the planar and channel geometries by combining them, with the resulting geometry being that of a tapered waveguide. Tapered waveguides can be defined using standard photolithography, with an appropriate mask, allowing the use of conventional channel waveguide fabrication techniques. The reduction in fabrication complexity, combined with the monolithic design, makes tapered waveguides an attractive alternative to unstable resonators. Tapered waveguide lasers also have the attractive quality of producing a

near symmetric output, leading to an improved fibre coupling loss in comparison to planar waveguide lasers. The near symmetric output, in conjunction with planar fabrication techniques, makes the tapered waveguide an attractive laser source for integrated optoelectronic devices.

The operation of a tapered waveguide is discussed in this chapter, with emphasis on the production of a diode-pumped tapered waveguide laser. It is difficult to calculate the modal properties of the varying, three-dimensional shape of a tapered waveguide laser. Basic waveguide theory, as derived in the previous chapter, is not applicable and for this reason the tapered waveguides will be modelled using the beam propagation method (BPM). BPM analysis is completed to test the design criteria of tapered waveguides, and to allow insight into their operation.

3.2 The Tapered Waveguide

The tapered waveguide (figure 3.1) consists of three sections: a planar-like section (named the broad section), a taper and a channel section. The lateral mode size within the channel and broad section of the waveguide are radically different, and would therefore suffer from large coupling losses if the two sections were butted together. This problem is overcome by converting the mode size between the two sections, using an interconnecting taper.

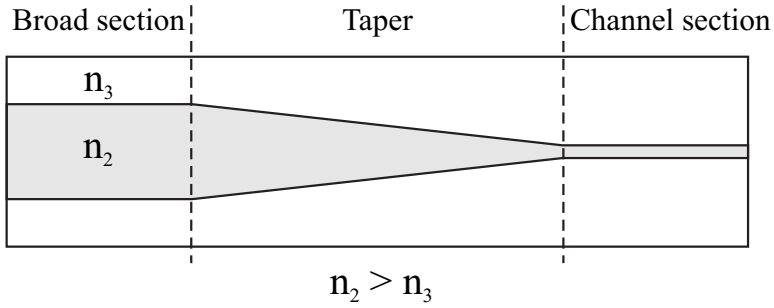

Figure 3.1: Plan view of a tapered waveguide

Single-mode output from the tapered waveguide is produced by designing the channel section to support only a single mode at the laser wave-

length. The taper converts the single-mode within the channel, to a mode of greater lateral size within the broad section. A fundamental operational requirement of the taper is that the mode size conversion must take place without coupling power to higher order modes. This requirement is termed 'adiabatic operation,' and is possible through the use of careful taper design [4,5]. The design criteria required for achieving adiabatic operation will be discussed more rigorously in the following theory section (section 3.3).

The tapered waveguide has many advantages in relation to the production of high-power, single-mode, waveguide lasers. The broad section allows high coupling efficiencies of a diode-pump, whilst the expanded laser mode within this section allows a good overlap between the single-mode laser and the multimoded pump. The taper itself acts as a mode filter, causing relatively large losses to be incurred for modes higher than the fundamental, which inhibits their lasing.

Tapers have been utilised for some time in semiconductor lasers to reduce the power density of the laser mode, and therefore the advent of catastrophic facet damage [6, 7], and to improve mode-matching between the laser output and optical fibres [8]. Tapers have also found use within fibre lasers for the production of a single-mode output [9]. Within the planar geometry tapers have found diverse applications including: improving coupling between diode-lasers and fibre optics [10] or channel waveguides [11], reducing the insertion loss between planar waveguides and fibre optics [12], collimating beams in waveguide interferometers [13] and improving the overlap of modes of different wavelength for non-linear processes [14]. More recently tapered waveguides have been used within active dielectric media for the production of lasers, as detailed in this thesis, and later by Madasamy et. al. [15].

Various fabrication methods have been utilised for the production of tapered waveguides, the majority of which use standard photolithography in conjunction with standard waveguide fabrication techniques, such as ion exchange [5, 12, 15] and proton exchange [11]. Novel fabrication techniques have also been employed, such as post-baking ion exchanged

waveguides in a strong temperature gradient [12], proton exchanged segmented waveguides [14], self-written tapered waveguides [16] and tapered rib waveguides [17]. The requirement of low-loss, wide taper openings and the use of glass as the substrate material, limits the following work to the ion exchange fabrication technique.

3.3 Tapered Waveguide Theory

Burns et. al. [18] derived equations to determine the operation of a tapered waveguide using the effective index method. This method allows insight into the modal properties of a waveguide with two-dimensional confinement [19], and is described in more detail in appendix A.

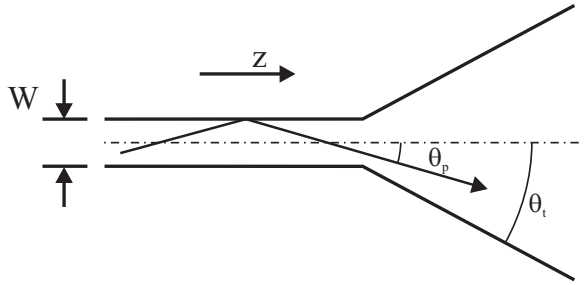

Figure 3.2: Ray path and angle within a tapered waveguide

The ray model of a tapered waveguide (figure 3.2), in conjunction with the effective index method allows the propagation angle θ_p of the ray to be determined [18] (see appendix A for derivation):

$$\cos\theta_p = \frac{n_3 + \Delta n b b'}{n_3 + \Delta n b} \tag{3.1}$$

Where $\Delta n = n_2 - n_3$, is the index difference between the core index n_2, and the substrate index n_3. The variables b and b' are the normalised indices and are defined as [19]:

$$b = \frac{n_{eff}^2 - n_3^2}{n_2^2 - n_3^2} \tag{3.2}$$

$$b' = \frac{n'^2_{eff} - n_3^2}{n_{eff}^2 - n_3^2} \tag{3.3}$$

Where n'_{eff} is the effective index of the fundamental mode in a channel waveguide, and n_{eff} is the effective index of the fundamental mode within a planar waveguide of equal depth.

For small values of Δn, as achieved with the ion exchange process used during this thesis (chapters 4 and 5), equation 3.1 can be simplified using the small angle approximation:

$$\theta_p = \left(\frac{2b\Delta n}{n_3} (1 - b') \right)^{\frac{1}{2}} \tag{3.4}$$

The guidance condition for the fundamental mode of a channel waveguide can be stated (appendix A):

$$V' (1 - b')^{\frac{1}{2}} = 2 \tan^{-1} \left(\frac{b'}{1 - b'} \right)^{\frac{1}{2}} \tag{3.5}$$

With V' defined as the normalised guide width [19]:

$$V' = k_0 W \left(n_{eff}^2 - n_3^2 \right)^{\frac{1}{2}} \tag{3.6}$$

Where W is the guide width, $k_0 = 2\pi/\lambda_0$, and λ_0 is the free-space wavelength.

Substituting equations 3.5 and 3.6 into equation 3.4 produces:

$$\theta_p = \frac{\lambda_0}{2n_3 W} \left(\frac{\tan^{-1} \sqrt{\frac{b'}{1-b'}}}{\frac{\pi}{2}} \right) \tag{3.7}$$

As W increases $n'_{eff} \rightarrow n_{eff}$ and therefore $b' \rightarrow 1$ and the value in the brackets $\rightarrow 1$, which allows the propagation angle to be approximated for modes far from cut-off as:

$$\theta_p = \frac{\lambda_0}{2n_3 W} \tag{3.8}$$

A supposition is made to relate the propagation angle and the taper angle θ_t [18]. If $\theta_t > \theta_p$ then the ray would not 'see' the waveguide wall, no guidance would be experienced and the beam would diverge as if propagating in a bulk medium. For this reason the taper angle is designed so that:

$$\theta_t = \alpha\theta_p \tag{3.9}$$

Where α is a constant: $\alpha \leqslant 1$.

Substituting this into equation 3.8 yields:

$$\theta_t = \frac{\alpha\lambda_0}{2n_3 W} \tag{3.10}$$

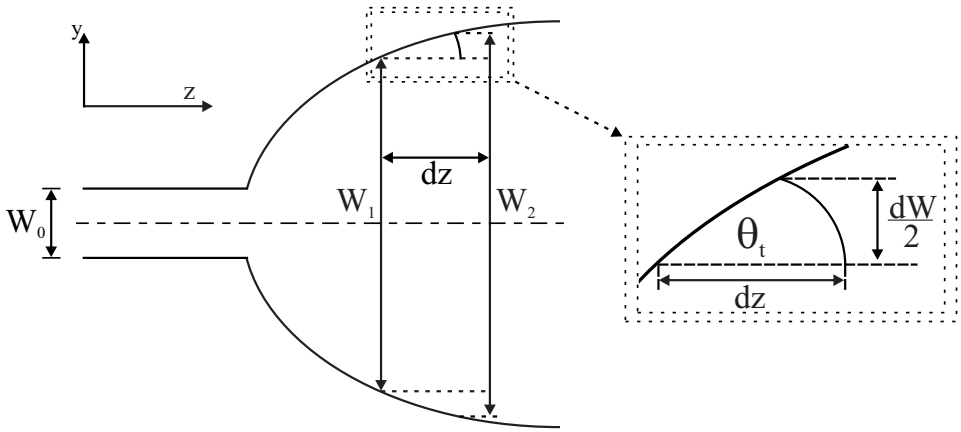

Figure 3.3: Relationship between the change in taper width and the local taper angle

The change in the taper width can be related to the local taper angle (figure 3.3) through:

$$\theta_t = \frac{1}{2}\frac{dW}{dz} = \frac{\alpha\lambda_0}{2n_3 W} \tag{3.11}$$

Rearranging, then integrating the above equation provides an equation that describes a parabola of the form:

$$W^2 = \frac{2\alpha\lambda_0}{n_3}z + W_0^2 \tag{3.12}$$

Where W_0 is the initial channel width of the taper at $z = 0$

The length of the optimum parabolic taper L, can be described by rearranging equation 3.12 for $z = L$, and neglecting W_0 as $W \gg W_0$:

$$L = \frac{W^2 n_3}{2\alpha\lambda_0} \tag{3.13}$$

Parabolic tapers can now be designed using equations 3.12 and 3.13 for a chosen value of α. Milton and Burns [4] recommend that for adiabatic operation $\alpha \leqslant 1$ as values greater than this will cause coupling to higher order modes. It should also be stated that the above equations have been determined using a more rigorous mathematical method that evaluates the mode amplitude overlap along a taper approximated by a series of steps [4, 20]. The analysis is more complicated than that shown here, but produces exactly the same design equation for the parabolic taper.

During this thesis linear and parabolic taper shapes have been investigated. Once parabolic tapers had been designed, following the equations defined above, a photolithographic mask was required to allow fabrication of the waveguides. The mask design and fabrication procedure can be lengthy, so experiments began with an available mask that contained linear tapers. These tapers consisted of a $175\mu m$ wide broad section and a $2.5\mu m$ wide channel section connected by a 0.4° linear taper, which relates to a taper length of $12.5mm$. The adiabatic operation of linear tapers has been investigated by Duport et. al. [5], using BPM to model linear tapers of varying angles. It was found that linear tapers with angles $\leqslant 0.77^\circ$, and lengths of $\approx 2mm$ provided adiabatic operation with less than 5% of power lost to higher order modes. Under this rationale it was decided that the tapers available with this mask should allow reasonable adiabatic performance, and were therefore worth investigation.

3.4 Design of Tapered waveguides

The possibility of diode pumping a tapered waveguide can now be investigated with reference to the geometrical restrictions outlined in the previous section. The depth and width of the broad section required to allow the end-launch of a diode-bar pump, can be calculated from the numerical aperture (NA) of the waveguide and the following equation [21]:

$$D \geqslant \frac{M^2 \lambda}{NA} \tag{3.14}$$

Where M^2 represents the factor that the beam divergence exceeds the diffraction limit, λ is the pump wavelength and D is either the width or depth of the broad section.

The value used for the NA, is that gained from K^+–Na^+ thermal ion exchange (TIE) within BK7 glass, assuming a step index profile. A typical value of $M^2 \approx 1000 \times 1$ is assumed for the M^2 of a diode-bar laser in the slow axis and fast axis respectively. An end-launch of the diode-bar would require a broad section $\approx 5\mu m$ deep, which is easily achieved through ion exchange [22], and $\approx 5mm$ wide. From equation 3.13, it can be shown that a taper length of $\approx 20m$ would be required for adiabatic operation ($\alpha = 1$). It would not be possible to work with a substrate of this size, which negates the possibility of diode-bar end-pumping a tapered waveguide. However, other possibilities exist. The superior slows axis beam quality of a broad-stripe diode ($M^2 \approx 20$–30) would require a broad section width of $\approx 200\mu m$, producing a more manageable taper length of $\approx 30mm$. End-pumping with a broad stripe laser would allow access to incident pump powers up to $4W$ from a single diode (section 4.6.5), and $\approx 8W$ from two polarisation coupled diodes. Theoretically, it should also be possible to side pump a taper of this size with a diode-bar, if the waveguide was produced in a medium with sufficiently high pump absorption (section 6.4).

Three groups of tapered waveguides were investigated during this thesis, with each group being used to test a different aspect of the taper perfor-

mance. Thermal ion exchange (TIE) and field-assisted ion exchange (FAIE) were used to fabricate the waveguides. These methods use standard photolithographic techniques to delineate the taper shape. Details of the features on the photolithographic mask, used during the fabrication of the tapered waveguides, are listed in appendix B.

3.5 Analysis of Tapered waveguides by the Beam Propagation Method

The modal behaviour of complex waveguides, such as tapers, can be studied with commercially available software (Prometheus software published by Kymata, Netherlands) using the beam propagation method (BPM). Analysis of the tapered waveguides was completed to gain qualitive insight into the operation of a tapered waveguide, and to test the design criteria established in the previous theory section.

The finite difference method (FD-BPM) was chosen to model the behaviour of the waveguides, as it has been shown to be accurate for longitudinally varying waveguides with small index differences [23, 24], and allows access to a reasonably fast calculation algorithm [23].

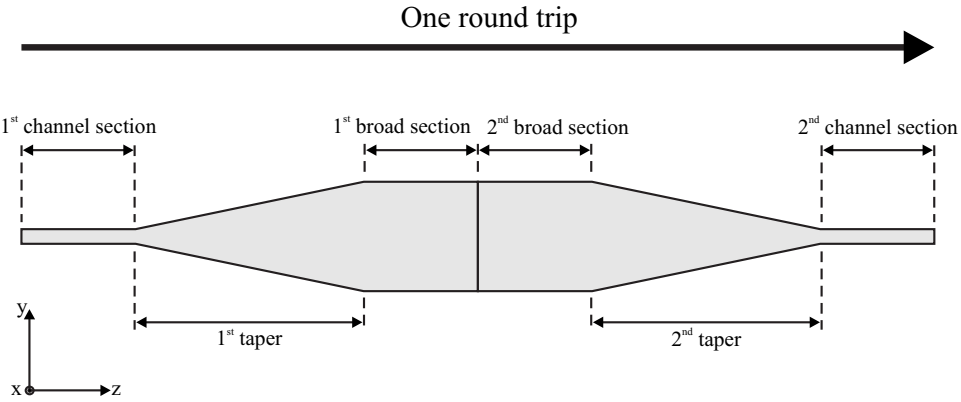

Figure 3.4: Back-to-back taper design used during BPM to model a single round-trip within a laser cavity

FD-BPM operates by evaluating the field at a series of test points that form a grid within the test structure. Two or three dimensional grids are used, depending on whether two or three-dimensional BPM is to be completed,

with the separation between the test points ($\Delta x, \Delta y, \Delta z$), determining the accuracy. Improved accuracy is gained by reducing the spacings between test points, however, the calculation time is dramatically increased as the grid spacings are reduced. Grid spacings of $0.5 \times 0.5 \times 1.0\mu m$ in the x, y and z directions respectively, were used during the following modelling, which allowed evaluation of the narrowest features and resulted in a calculation time of $48hr$ for the 3D models. The structure used during the modelling is depicted in figure 3.4, and consists of two tapered waveguides placed back-to-back, to model a single round-trip within a cavity. The analysis begins by generating a fundamental-mode, start field within the first channel of the structure. The field is propagated by a distance Δz along the z-axis, and the effect on the field in the lateral directions is calculated from the paraxial wave equation, which is a simplification of the wave equation (equation 2.11). This process of propagation, and field evaluation is completed over the length of the structure, allowing the field evolution and resulting output field to be calculated. The model analyses only the effect on the waveguide mode due to propagation through the taper, and does not account for any gain or loss through scattering or absorption.

3.5.1 Two Dimensional Analysis

The structures were modelled to represent a tapered waveguide fabricated by K^+–Na^+ thermal ion exchange (TIE) in BK7 glass. During 2D modelling the core index was assumed to be constant, with the magnitude determined from the known maximum value for K^+–Na^+ TIE within BK7 glass [22].

3.5.2 Investigation of Taper Shape and Adiabatic Operation

Linear and parabolic tapers were modelled using 2D BPM to investigate the effect of the taper shape on the taper performance. Four linear tapers were designed with different taper angles ranging from $0.1°$–$5°$, to investi-

gate the effect of the taper angle on the performance of a linear taper. The length of each linear taper was calculated from the taper angle and width. Four parabolic tapers were designed with lengths identical to the linear tapers, to allow fair comparison between taper shapes. Equation 3.13 was used for the parabolic design, with the constraints placed on the taper length resulting in $\alpha \approx 0.3$–15. The taper design parameters are shown in table 3.1.

Taper number	Taper shape	α value	Taper angle ($^\circ$)	Taper length (mm)	Taper efficiency (%)
PT1	Parabolic	14.60	—	1.0	1.7
LT1	Linear	—	5.00	1.0	0.4
PT2	Parabolic	2.05	—	7.0	33.6
LT2	Linear	—	0.70	7.0	51.1
PT3	Parabolic	1.15	—	12.5	75.2
LT3	Linear	—	0.40	12.5	84.7
PT4	Parabolic	0.29	—	49.5	99.0
LT4	Linear	—	0.10	49.5	99.6

Table 3.1: Taper design parameters for 2D modelling

3.5.2.1 Discussion of Results

An analysis, showing the percentage of power within each mode as it propagates through the tapered waveguide, was completed for each taper. A sample of this analysis, calculated for the parabolic taper PT2, is shown in figure 3.5. At the beginning of propagation all power is confined within the single mode of the first channel. Within the first taper the lateral confinement is reduced, and if the taper is not correctly designed, power is converted from the fundamental mode to higher order modes. However, the taper confines these higher order modes, which results in no overall loss of confined power, even though the percentage of power contained in the fundamental mode has reduced. The broad section also confines the higher order modes, and as no change in the waveguide geometry occurs in this section, the power in each mode stays constant. Coupling between modes occurs again within the second taper, as shown in figure 3.6. The higher order modes are radiated from the waveguide, as the confinement

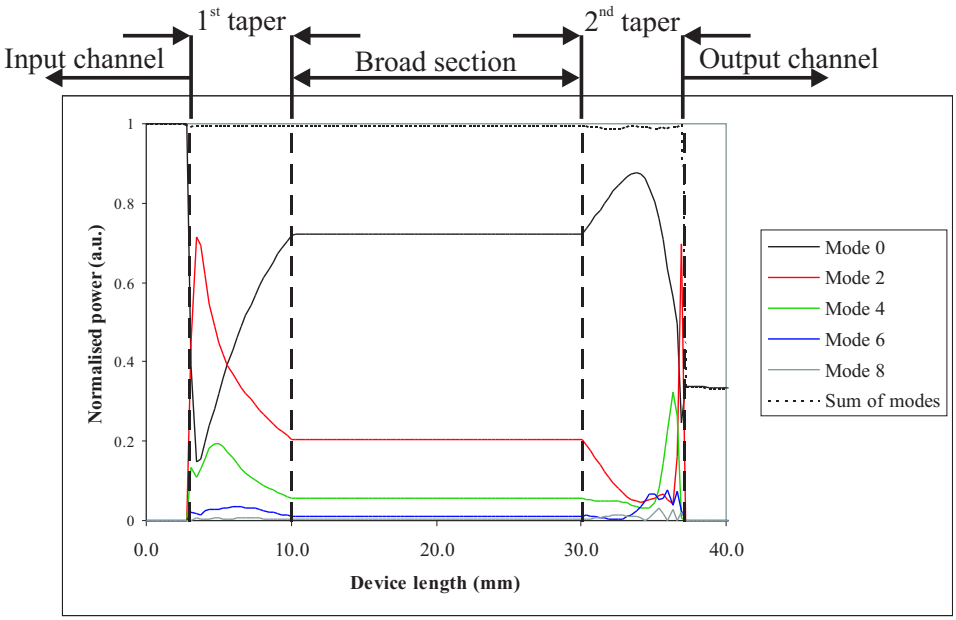

Figure 3.5: Transfer of power from the fundamental mode to higher order modes over one round-trip, within taper PT2

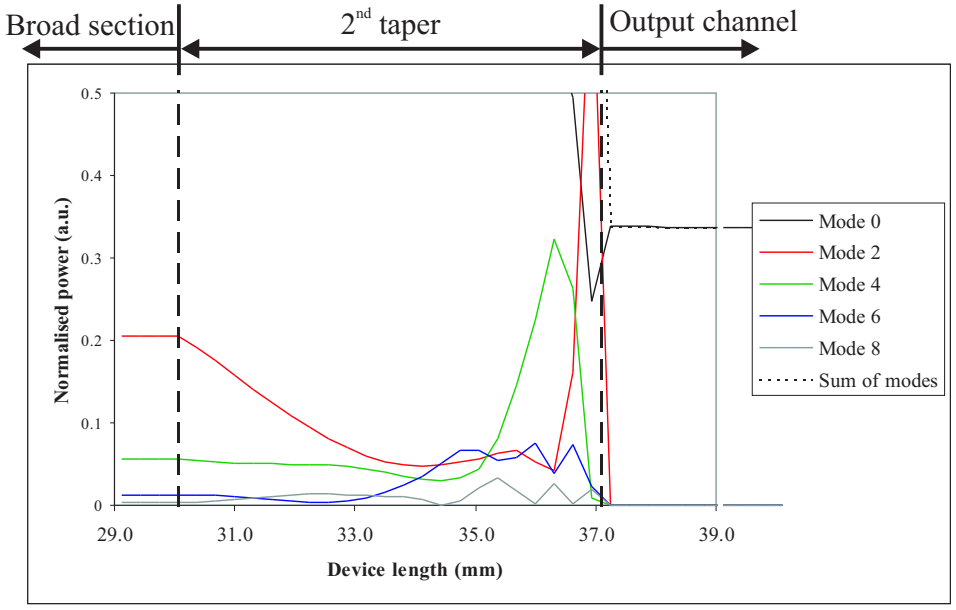

Figure 3.6: Close up of the second taper from figure 3.5

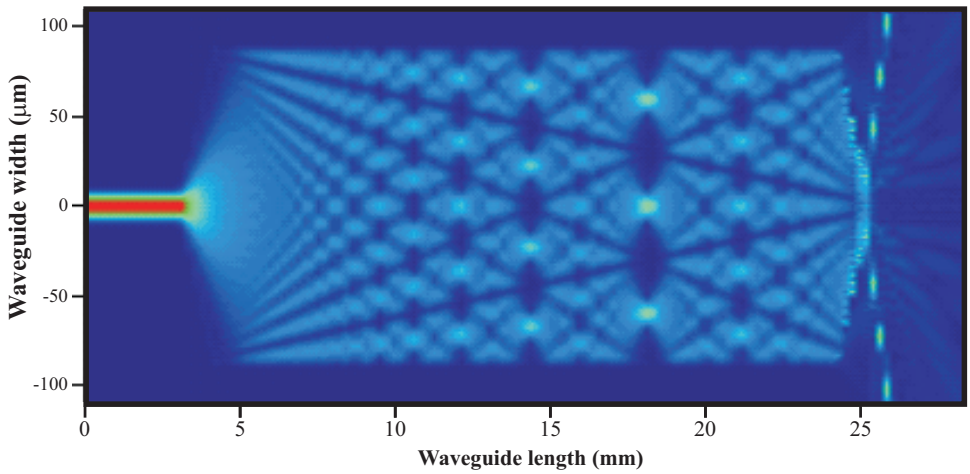

Figure 3.7: Evolution of the intensity in taper LT1 with higher intensities denoted by brighter colours

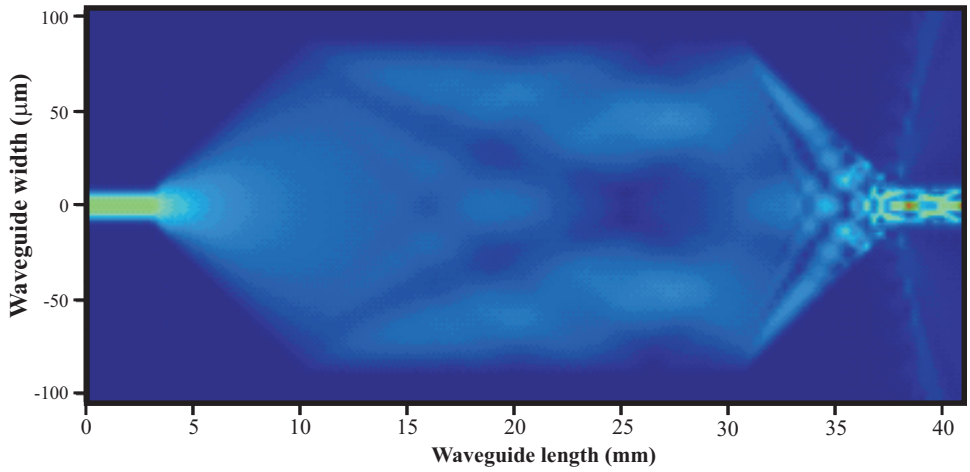

Figure 3.8: Evolution of the intensity in taper LT2 with higher intensities denoted by brighter colours

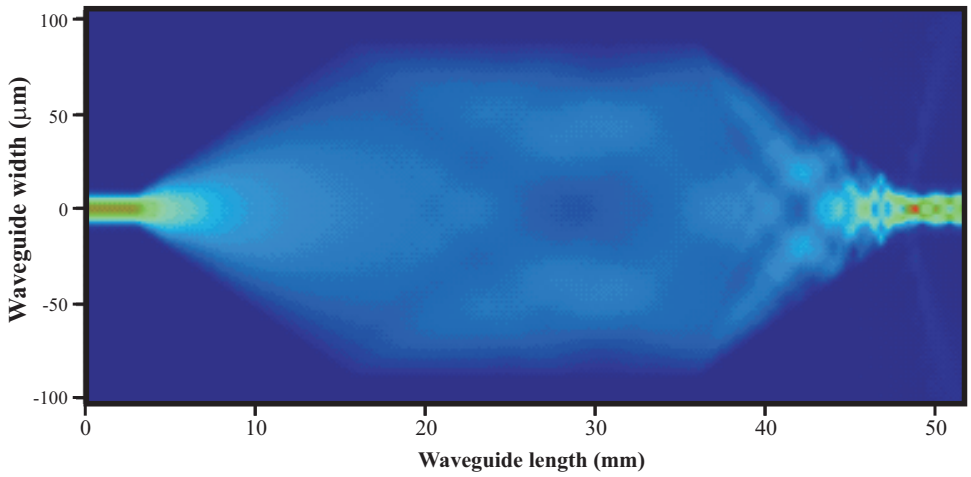

Figure 3.9: Evolution of the intensity in taper LT3 with higher intensities denoted by brighter colours

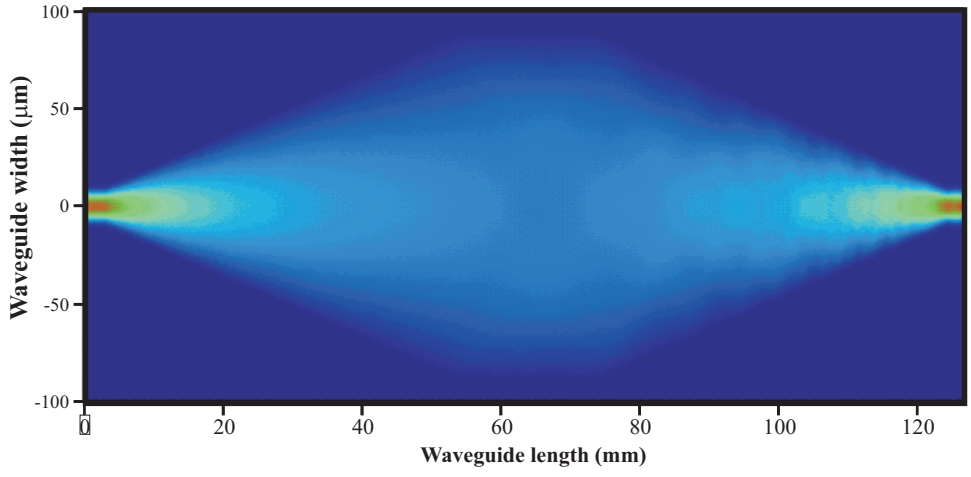

Figure 3.10: Evolution of the intensity in taper LT4 with higher intensities denoted by brighter colours

offered by the taper is reduced, causing a reduction in the overall confined power. At the second channel all modes other than the fundamental have been radiated out of the waveguide, which is illustrated by the convergence of the total power within the waveguide, and the power in the fundamental mode. This behaviour is consistent for all of the modelled waveguides, although the tapers with more stringent design criteria (i.e. smaller taper angles, or lower α coefficients) exhibited far less mode coupling, as can be seen from the improved taper efficiencies shown in table 3.1.

The conversion of power from the fundamental mode can be illustrated by viewing the field as it evolves through the taper. Figures 3.7 to 3.10 shows a diagrammatic representation of the intensity within the four linear tapers, with higher intensities denoted by brighter colours.

As will be discussed in section 3.5.4, the index profile used during the 2D-BPM modelling is not a realistic representation of a tapered waveguide fabricated by ion exchange. However, 2D-BPM allows some qualitive statements to be made concerning the taper operation. The model indicates that linear tapers outperform parabolic tapers, for the $175\mu m$ taper width investigated here. Milton and Burns [4] modelled tapers with widths $\leqslant 50\mu m$; it is possible that parabolic taper efficiency is improved within this narrower regime, which may explain their preference for the parabolic shape.

Some practical assertions must be made to allow implementation of these designs. Although very high taper efficiency is gained through the use of tapers such as LT4 and PT4, the $\approx 5cm$ taper length, in addition to the $2cm$ long broad channel required to gain reasonable absorption of a diode-pump, would result in an impractically large waveguide. In addition to the practicalities concerning waveguide fabrication, an increase in the waveguide length increases the propagation loss, which should be minimised to improve laser performance. It is therefore necessary to make a concession in the taper efficiency to allow fabrication of practical waveguides.

3.5.3 Effect on Performance of Taper End-Face Misalignment

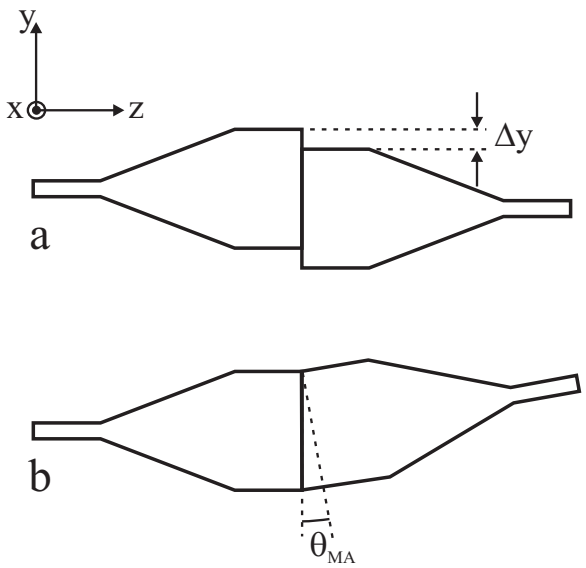

Figure 3.11: The two different types of taper misalignment: a/ lateral displacement, b/angular misalignment

Nelson [25] investigated the effect of taper misalignment on the taper efficiency, with the emphasis on reducing the insertion loss between two tapered waveguides. Two types of taper misalignment were studied: lateral displacement (figure 3.11a) and angular misalignment θ_{MA} (figure 3.11b). Nelson studied the taper efficiency of two separate tapered waveguides butted together at the broad section. The double taper structure (figure 3.4) studied during this chapter is not of this form, and is instead a model of a round-trip within a laser cavity, with the second taper used to model the return of the mode through the taper, after reflection at a mirror. Therefore, there is no possibility of lateral displacement in the tapered waveguide laser, however, angular misalignment is possible.

As will be discussed in section 4.4.3, during fabrication the tapered waveguides are delineated by photolithographic means. During photolithography the waveguides are aligned to be parallel with a polished side-face of the substrate material. Polishing of the substrate end-faces, perpendicular to the axis of the waveguide, is achieved using the polished side-face of the substrate as a reference. Photolithographic techniques are highly accurate

and, if completed correctly, produce a maximum angular misalignment of $0.007°$ (calculated for the waveguides produced during this thesis). Accurate polishing is more difficult, with a particularly poor example of polishing producing an angular misalignment between the end-faces of $0.2°$.

The effect of angular misalignment on the coupling efficiency of the tapered waveguides was investigated using 2D-BPM, identical to that in the previous section. An angular misalignment between 0.00–$0.20°$ was added to the second taper, as shown in figure 3.11b. The effect of this misalignment was studied within tapers PT3 and LT3 (i.e. $175\mu m$ wide, $12.5mm$ long parabolic or linear tapered waveguides). As discussed in the previous section, the use of a step-index profile required for 2D-BPM, is not representative of a waveguide fabricated by TIE. However, the qualitative results found within this section allow an insight into the effect of end-face misalignment on the performance of a tapered waveguide.

3.5.3.1 Discussion of Results

The effect of angular misalignment on the performance of a tapered waveguide was investigated by analysing the efficiency of each taper for various angular misalignments. The results of the analysis are listed in table 3.2. The effect of a $0.2°$ angular misalignment on the intensity within a parabolic and a linear tapered waveguide is shown graphically in figures 3.12 and 3.13.

Table 3.2 highlights the dramatic effect of angular misalignment on the taper efficiency, with a misalignment of only $0.15°$ causing an $\approx 40\%$ decrease in the taper efficiency of the linear taper. These results are consistent with those found by Nelson [25], who also concluded that the angular misalignment must be $\ll 0.2°$. The misalignment causes the excitation of higher order modes that are supported within the broad section, but are radiated from the waveguide within the taper, an effect that can be seen in figures 3.12 and 3.13. Mode coupling is not limited to higher-order, even-modes, as was the case in the previous section, as the angularly misaligned taper is no longer symmetric around the z-axis. The radiation of

Linear taper LT3	
θ_{MA} (°)	Taper efficiency (%)
0.00	84.7
0.05	74.9
0.10	73.6
0.15	49.5
0.20	6.4

Parabolic taper PT3	
θ_{MA} (°)	Taper efficiency (%)
0.00	75.2
0.05	65.2
0.10	41.5
0.15	20.1
0.20	8.5

Table 3.2: Effect of angular misalignment on taper efficiency

Linear taper LT3	
Taper width (μm)	Taper efficiency (%)
50	98.4
100	94.8
150	76.4
175	73.6
250	13.8

Parabolic taper PT3	
Taper width (μm)	Taper efficiency (%)
50	99.4
100	93.6
150	84.1
175	41.5
250	13.0

Table 3.3: Effect of taper width on taper efficiency for a constant angular misalignment of $0.1°$

the higher order modes from the waveguide at the tapered section, causes the reduction in the calculated taper efficiency.

The effect of angular misalignment at the channel end of the taper is less pronounced than at the broad section, as the channel can support only a single-mode, negating excitation of higher order modes. This assumption is reinforced by modelling the effect of a constant $0.1°$ angular misalignment on the taper efficiency for various taper widths. Table 3.3 lists the results of this analysis for a parabolic and linear taper. Both the linear and parabolic taper shapes show a reasonable efficiency up to a taper width of $150\mu m$, however, an increase in the taper width beyond this point causes the taper efficiency to drop dramatically. Consequently, the larger taper widths desired for efficient diode-pumping of a tapered waveguide will require strict control over the alignment during photolithography and polishing.

The effect of angular misalignment was noticed during the laser charac-

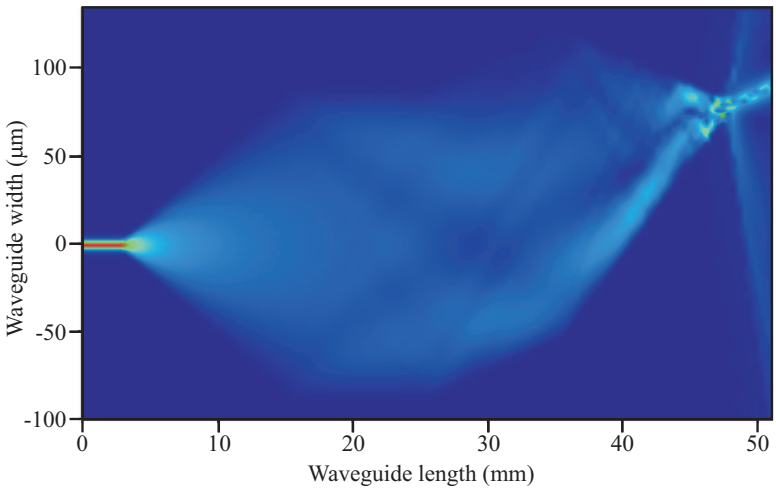

Figure 3.12: Illustration of the effect on the intensity within a linear taper, due to an angular misalignment of $0.1°$

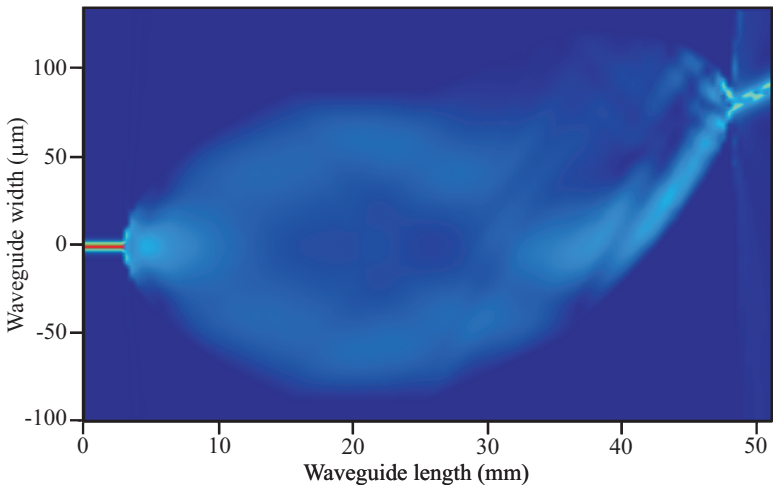

Figure 3.13: Illustration of the effect on the intensity within a parabolic taper, due to an angular misalignment of $0.1°$

terisation of the tapered waveguides fabricated during this thesis. For this reason all waveguide substrates were sent to an independent polishing company where a maximum angular misalignment of 0.02–0.07° was assured.

3.5.4 Three Dimensional Analysis

A constant index profile, as used during the 2D modelling, is a simplification of the TIE process, which in reality produces a graded index in the depth dimension for planar waveguides [26], and in both the depth and width for channel waveguides [27]. The two-dimensional graded index was accounted for during the 3D modelling, through the use of the index profile calculated by Weiss and Srivastava [27] (equation 3.15), which is explained in more detail in section 4.3.2:

$$n_c\left(x,y\right) = n_3 + \Delta n \exp\left(\frac{-x^2}{d_x^2}\right) erfc\left(\frac{y}{d_y}\right) \text{ for } y \geqslant 0 \qquad (3.15)$$

Where $n_c(x,y)$ is the refractive index profile of the channel, n_3 is the substrate refractive index, Δn is the difference between the refractive index at the surface of the waveguide and the substrate, d_x and d_y are the $1/e$ half width and the erfc(1) depth of the channel respectively.

Weiss and Srivastava modelled the index profile for channels up to a maximum width of $10\mu m$; it was believed that the profile would become more planar-like within the relatively wide broad section of the taper. An attempt to model this quasi-planar nature was made through the use of a 'super-Gaussian,' which produces a flatter profile than a standard Gaussian:

$$n_{bc}\left(x,y\right) = n_3 + \Delta n \exp\left\{\left(\frac{-x^2}{d_x^2}\right)\right\}^4 erfc\left(\frac{y}{d_y}\right) \text{ for } y \geqslant 0 \qquad (3.16)$$

Where $n_{bc}(x,y)$ is the refractive index profile of the broad section.

The index profile of the taper was modelled to match the index at the extremes of the channel and broad sections, and to vary gradually between

the sections.

A total channel width of $2d_x = 3.58\mu m$ was calculated from the mask opening used to fabricate the channels, taking into consideration the lateral diffusion found with TIE [27], over the $12hr$ fabrication time used during production of the waveguides. Channels of this width were found to support a single-mode at the $1.06\mu m$ wavelength used during modelling.

The waveguide depths d_y were calculated from previous work completed for the K^+–Na^+ TIE process in BK7 [26, 27] and were found to be $4\mu m$ and $10\mu m$ for the channel and broad section respectively. The width of the mask opening used to form the waveguide, and the ion exchange duration, determine the waveguide depth gained by TIE. This phenomenon causes an additional taper in the depth of the waveguide, which was accounted for during the modelling.

Two tapers of each shape were investigated with 3D-BPM. Parabolic tapers of widths $175\mu m$ and $250\mu m$ were designed with $\alpha = 2$, which would allow investigation of taper widths more suitable for diode pumping. Linear tapers were then designed with identical widths and lengths to allow fair comparison between the taper shapes. The design parameters for these tapers are listed in table 3.4.

Taper number	Taper shape	Taper width μm	α value	Taper angle (°)	Taper length (mm)
PT5	Parabolic	175	2.00	—	11.0
LT5	Linear	175	—	0.45	11.0
PT6	Parabolic	250	2.00	—	22.3
LT6	Linear	250	—	0.32	22.3

Table 3.4: Taper design parameters used during 3D modelling

3.5.4.1 Discussion of Results

Figure 3.14 shows a representation of the index profile generated for taper PT6, which follows the desired profile. The effect of this profile on the field is shown in figure 3.15. The expected lateral spreading of the field

can be seen within the broad section, with the smooth profile indicating little conversion to higher order modes. The results of the power analysis of the four tapers are listed in table 3.5.

Taper number	Taper shape	Taper width μm	Taper efficiency (%)
PT5	Parabolic	175	94.7
LT5	Linear	175	97.6
PT6	Parabolic	250	96.9
LT6	Linear	250	98.0

Table 3.5: Taper efficiency of the four tapers modelled during 3D BPM

Comparisons can be made between 2D and 3D-BPM, by comparing the relatively similar tapers: PT2 & PT5, and LT3 & LT5. Improved taper efficiencies are found with 3D-BPM, which are most noticeable for the parabolic tapers. This has been attributed to the greater confinement of the mode gained through the graded index profile. The taper efficiencies range between 94.7–98.0%, which can be related to taper losses between 0.23–$0.09dB$ per round trip. Channel waveguides fabricated by TIE in BK7 have been measured to have losses of $< 0.2dBcm^{-1}$ [2], leading to the assumption that a taper loss of this magnitude would not radically affect the performance of a tapered waveguide laser.

Although BPM can only provide qualitative results, as there is a degree of uncertainty concerning the exact index profile of the waveguides, the high taper efficiencies gained during this modelling allowed sufficient confidence in the taper design to fabricate tapered waveguides using equation 3.13 with $\alpha = 2$. This design parameter was used to model parabolic tapered waveguides with widths between 175–$250\mu m$. Linear tapers were designed with identical widths and lengths as the parabolic tapers, to investigate the indicated improvement in taper efficiency for the linear shape. The laser results for these waveguides are described in section 4.6.2.

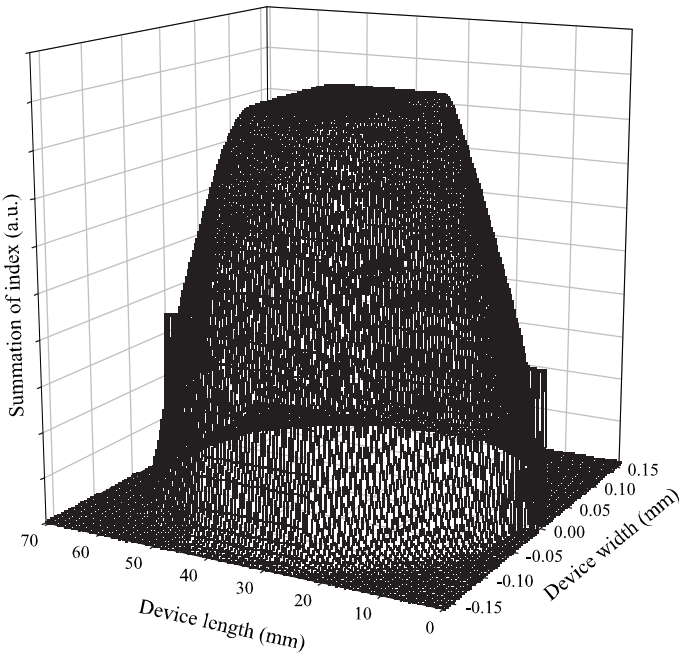

Figure 3.14: Representation of the refractive index profile used during 3D-BPM modelling

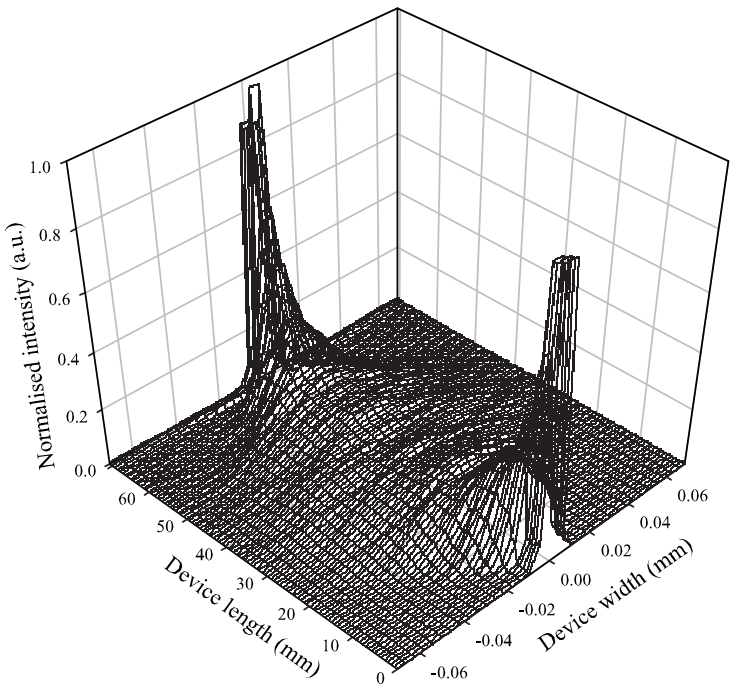

Figure 3.15: Evolution of the intensity within a tapered waveguide

3.6 Summary

The theory behind the design of tapered waveguides has been derived, following the method of Milton and Burns [4]. Equation 3.13 allows a simple method for designing adiabatic tapered waveguides of any width. However, this method is only applicable to tapered waveguides produced with a low Δn (typically $\Delta n \approx 10^{-3}$). It is fortunate that the fabrication methods proposed for the production of a tapered waveguide, create a Δn of this order.

The practical considerations concerned with the production of a tapered waveguide, with an appropriate width for diode-pumping, have been discussed. These considerations led to the design of linear and parabolic tapered waveguides, with widths between 175–$250\mu m$. As previously discussed, the waveguide theory detailed in chapter 2 is not sufficient to detail the operation of complex shaped waveguides, such as a tapered waveguide. However, BPM modelling allows the operation of a tapered waveguide to be explored, and has been used to calculate the taper efficiency of a number of tapers with various widths and lengths.

An initial investigation of the tapered waveguide was completed using 2D-BPM. The simplification of the waveguide into a 2D structure leads to possible errors in the analysis, but allows a number of different tapers to be modelled in a short time, which is an important first step. The results of this analysis indicate that tapers, designed using the Milton and Burns approach, operate adiabatically. Linear tapers seem to operate with a higher taper efficiency than parabolic tapers of equal length and width. However, confidence in this result must be offset against the errors inherent with 2D-BPM. The effect of an angular offset was also investigated with 2D-BPM, and indicated the dramatic effect of a relatively small angular offset (0.10–0.20°) on the performance of a tapered waveguide. The effect of an angular misalignment on the taper efficiency, indicates the care that must be taken over the photolithographic and polishing alignment during fabrication of these devices.

Further analysis of possible taper designs, which were identified with 2D-

BPM, were investigated using 3D-BPM. The 3D-BPM analysis required the addition of a refractive index profile to the taper model, which was completed following the results of Weiss and Srivastava [27]. 3D-BPM analysis led to an improved taper efficiency for each of the four tapered waveguide designs tested. The improvement in the efficiency calculated for each of the tapers has been attributed to the improved confinement afforded by the graded index profile. A taper efficiency $\geqslant 95\%$ was calculated for each taper, which allows some confidence in predicting efficient taper operation from the actual tapered waveguides fabricated and tested in chapters 4 and 5. However, the results generated by BPM analysis can only be seen as indicative of the later performance of the tapered waveguides, due to the errors inherent in the analysis. Further errors may arise from the uncertainty in the actual refractive index profile and maximum refractive index change, produced by the fabrication methods detailed in chapters 4 and 5.

3.7 References

[1] D.P. Shepherd, S.J. Hettrick, C. Li, J.I. Mackenzie, R.J. Beach, S.C. Mitchell and H.E. Meissner. High-power planar dielectric waveguide lasers. *Journal of Physics D*, 34 : p2420–2431, 2001.

[2] S.J. Hettrick, J.I. Mackenzie, R.D. Harris, J.S. Wilkinson and D.P. Shepherd. Ion-exchanged tapered-waveguide laser in neodymium-doped BK7 glass. *Optics Letters*, 25(19) : p1433–1435, 2000.

[3] H.J. Baker, A.A. Chesworth, D.P. Millas and D.R. Hall. A planar waveguide Nd:YAG laser with a hybrid waveguide-unstable resonator. *Optics Communications*, 191 : p125–131, 2001.

[4] A.F. Milton and W.K. Burns. Mode Coupling in Optical Waveguide Horns. *IEEE Journal of Quantum Electronics*, QE-13(10) : p828–835, 1977.

[5] I. Duport, P. Benech, D. Khalil and R. Rimet. Study of linear tapered waveguides made by ion exchange in glass. *Applied Physics Letters*, 82(9) : p1332–1334, 2003.

[6] E.S. Kintzer, J.N. Walpole, S.R. Chinn, C.A. Wang and L.J. Missaggia. High-Power, Strained-Layer Amplifiers and Lasers with Tapered Gain Regions. *IEEE Photonics Technology Letters*, 5(6) : p605–608, 1993.

[7] S.F. Yu. Double-Tapered-Waveguide Distributed Feedback Lasers for High-Power Single-Mode Operation. *IEEE Journal of Quantum Electronics*, 33(1) : p71–80, 1997.

[8] H. Li and D. Huang. Characteristics of semi-conductor laser diode with non-linearly tapered waveguide. *International Journal of Infrared and Millimeter Waves*, 21(5) : p751–757, 2000.

[9] J.D. Minelly, L.A. Zenteno, M.J. Deijneka, W.J. Miller, D.V. Kuksenkov, M.K. Davies, S.G. Crigler and M.E. Bardo. High power diode pumped single-transverse-mode Yb fibre laser operating at 978nm. *Optical Fiber Communication Conference and Exposition 2000, Baltimore*, Post-deadline paper : pPD2-1–PD2-3, 2000.

[10] M. Mashayekhi, T. Touam, W.J. Wang, E. Berolo and S.I. Najafi. Semiconductor device to optical fiber coupling using low-loss glass taper waveguide. *Optical Engineering*, 36(12) : p3476–3477, 1997.

[11] K. Mizuuchi, K. Yamamoto and T. Taniuchi. High-Efficiency Coupling of Laser Diodes in Tapered Proton-Exchanged Waveguides. *Electronics Letters*, 26(24) : p1992–1994, 1990.

[12] H. Zhenguang, R. Srivastava and R.V. Ramaswamy. Low-Loss Small-Mode Passive Waveguides and Near-Adiabatic Tapers in BK7 Glass. *Journal of Lightwave Technology*, 7(10) : p1590–1596, 1989.

[13] I.S. Duport, P. Benech and R. Rimet. New integrated-optics interferometer in planar technology. *Applied Optics*, 33(25) : p5954–5958, 1994.

[14] M.H. Chou, M.A. Arbore and M. M. Fejer. Adiabatically tapered periodic segmentation of channel waveguides for mode-size transformation and fundamental mode excitation. *Optics Letters*, 21(11) : p794–796, 1996.

[15] P. Madasamy, S. Honkanen, D.F. Geraghty and N. Peyghambarian. Single-mode tapered waveguide laser in Er-doped glass with multimode-diode pump. *Applied Physics Letters*, 82(9) : p1332–1334, 2003.

[16] S.J. Frisken. Light-induced optical waveguide uptapers. *Optics Letters*, 18(13) : p1035–1037, 1993.

[17] R.N. Thurston, E. Kapon and A. Shahar. Two-dimensional control of mode size in optical channel waveguides by lateral channel tapering. *Optics Letters*, 16(5) : p306–308, 1991.

[18] W.K. Burns, A.F. Milton and A.B. Lee. Optical waveguide parabolic coupling horns. *Applied Physics Letters*, 30(1) : p28–30, 1977.

[19] D.L. Lee. Electromagnetic Principles of Integrated Optics. *J. Wiley & Sons*, Ch. 5, New York, 1986.

[20] D. Marcuse. Radiation Losses of Tapered Dielectric Slab Waveguides. *The Bell System Technical Journal*, 49 : p273–290, 1969.

[21] D.P. Shepherd, C.L Bonner, C.T.A. Brown, W.A. Clarkson, A.C. Tropper, D.C. Hanna and H.E. Meissner. High-numerical-aperture, contact-bonded, planar waveguides for diode-bar-pumped lasers. *Optics Communications*, 160 : p47–50, 1999.

[22] R.V. Ramaswamy and R. Srivastava. Ion-Exchanged Glass Waveguides: A Review. *Journal of Lightwave Technology*, 6(6) : p984–1001, 1987.

[23] Y. Chung and N. Dagli. An Assessment of Finite Difference Beam Propagation Method. *IEEE Journal of Quantum Electronics*, 26(8) : p1335–1339, 1990.

[24] H.J.W.M. Hoekstra, G.J.M. Krijnen and P.V. Lambeck. On the accuracy of the finite difference method for applications in beam propagating techniques. *Optics Communications*, 94(6) : p506–508, 1992.

[25] A.R. Nelson. Coupling optical waveguides by tapers. *Applied Optics*, 14(12) : p3012–3015, 1975.

[26] J.E. Gortych and D.G. Hall. Fabrication of Planar Optical Waveguides by K^+–Ion Exchange in BK7 and Pyrex Glass. *IEEE Journal of Quantum Electronics*, QE-22(6) : p892–895, 1986.

[27] M.N. Weiss and R. Srivastava. Determination of ion-exchanged channel waveguide profile parameters by mode-index measurements.. *Applied Optics*, 34(3) : p455–458, 1995.

Chapter 4

Tapered Waveguides fabricated by Thermal Ion Exchange

4.1 Introduction

Thermal ion exchange (TIE) is a simple and low cost method of producing high quality, optical waveguides within a glass substrate. The process is not new, as it has been used for over a century to produce strengthened glass [1]. The first passive, planar waveguide was produced using thallium field-assisted ion exchange in 1972 by Izawa and Nakagome [2]; a year later the fabrication process was simplified by Giallorenzi et. al. [3] and the first TIE waveguide was produced. Since this time, ion exchange has been completed in a wide variety of glasses, using a number of different diffusant ions [2–5].

This chapter contains a detailed examination of the ion exchange process, the various factors that must be taken into account before a choice of fabrication parameters can be made, TIE theory, and the TIE fabrication and laser performance of tapered waveguide lasers.

4.2 Thermal Ion Exchange from a Molten Salt

TIE is based on the exchange of ions from a glass with ions from a diffusant source. To preserve clarity the ions originally in the glass will be

called the 'glass ions', whereas the ions from the diffusant source will be termed the 'diffusant ions'. During TIE a glass substrate is placed into a bath of a molten salt that contains diffusant ions. A concentration gradient is formed, as the concentration of diffusant ions is much higher within the salt than in the glass, which causes the diffusant ions to diffuse into the glass. Simultaneously, ions within the glass experience an opposite concentration gradient that causes diffusion out of the glass and into the salt. In this way the properties of the glass can be altered whilst preserving charge neutrality.

The most common method of TIE involves the exchange of glass ions (usually Na^+, K^+ and occasionally Li^+) with diffusant ions from a molten salt. Nitrate and sulphate salts have both been used successfully for this purpose. TIE is usually carried out below the substrate's glass transition temperature (T_g) to maintain the shape and polish quality of the substrate glass. For this reason, nitrate salts are the practical choice for TIE due to their relatively low melting temperatures (200–400°C) in relation to sulphate salts (500–600°C).

A metallic film, evaporated onto the surface of the substrate, can also be used as the source of diffusant ions. However, the majority of diffusant ions do not produce stable metallic films, limiting this method to the exchange of silver [6] and copper [7]. A recent novel ion exchange technique involves contact bonding a potassium rich glass to a glass with a lower potassium concentration [8]. The heating process required for contact bonding allows diffusion from the potassium rich glass and the creation of an ion exchanged waveguide. Although this process benefits from the one-step production of buried waveguides, it is limited to the production of planar waveguides and is therefore not suitable for tapered waveguide fabrication.

4.2.1 Effect of Ion Exchange on Refractive Index

The change in the refractive index of the substrate glass caused by ion exchange, is due to the different values of polarisability and ionic radius

of the exchanging ions. The refractive index of an oxide glass can be expressed by means of the refraction of its components [9, 10]:

$$n = 1 + \frac{R_0}{V_0} \tag{4.1}$$

Where n is the refractive index, R_0 the molecular refraction of oxygen atoms and V_0 the molar volume of oxygen atoms. The change in refractive index caused by ion exchange, can be expressed:

$$\Delta n = \frac{\chi}{V_0}\left(\Delta R - R_0\frac{\Delta V}{V_0}\right) \tag{4.2}$$

Where Δn is the change in refractive index, χ is the fraction of ions within the glass exchanged by ions from the melt, ΔR and ΔV are the alteration of R_0 and V_0 caused by the ion exchange.

Equation 4.2 is useful for showing the two contributions that create Δn. The first component of the equation is the contribution to Δn from the difference in the polarisabilities of the exchanged ions, whereas the second component is the contribution to Δn from the change in glass volume, produced by the different ionic radii of the exchanged ions.

As previously mentioned, TIE is usually completed below the glass transition temperature of the substrate glass. The viscosity of a glass increases substantially below the glass transition temperature, which is accompanied by solid-like behaviour, whilst above this temperature the glass begins to exhibit fluid-like behaviour [11]. Therefore, the glass is prevented from relaxing the stress caused by exchanging ions of different ionic radii [12] during TIE performed below the glass transition temperature. Lateral expansion of the glass is prevented by the substrate's resistance to bending, which causes expansion of the glass in the direction normal to the surface [13]. The stress created by the TIE process results in the production of a stress induced refractive index difference, with the anisotropy of these stresses producing a birefringent waveguide.

The stress induced contribution to the overall change in refractive index is dependent on the physical properties of the exchanging ions. Albert and

Ions	Δn(Calculated)	Δn(Experiment)
K^+—Na^+	0.0003	0.008
Ag^+—Na^+	0.082	0.09

Table 4.1: Calculated and experimentally determined values for Δn, showing that Fantone's method for determining the refractive index of TIE waveguides does not adequately describe the process

Ion	Polarisability ($\times 10^{-30} m^3$)	Ionic Radius ($\times 10^{-10} m$)
Na^+	0.43	0.95
K^+	1.33	1.33
Ag^+	2.40	1.26

Table 4.2: Polarisability and ionic radii of three diffusant ions

Yip [14] investigated this phenomenon in soda-lime glass with K^+—Na^+ and Ag^+—Na^+ ion exchange. It was found that for Ag^+ ion exchange the value for Δn calculated by equation 4.2, was in good agreement with the value found by experimental methods (table 4.1). However, for K^+ ion exchange the calculated value was much lower than that measured experimentally. The difference in the calculated and experimentally measured value of Δn for K^+ ion exchange is attributed to formation of stress in the glass.

The reason that stress induced effects are apparent for K^+ ion exchange, but not for Ag^+ ion exchange, becomes clear from table 4.2. During Ag^+–Na^+ ion exchange, Δn is dominated by the contribution of the relatively large difference in the polarisability of the two ions. Stress induced effects are still present, but are negligible when compared to the polarisability difference. Alternatively, with K^+–Na^+ ion exchange the polarisabilities of the two ions are more similar, making a lower contribution to Δn, whereas the difference in ionic radius is greater, allowing stress induced effects to become the dominant factor.

4.2.2 Physical Properties of Diffusant Ions

A number of diffusant ions have been used for TIE, these mainly being the monovalent alkali metal ions: Li^+ [4], K^+ [3], Rb^+ [5], and Cs^+ [5], although other monovalent metal ions have also been used successfully, namely Tl^+ [2], Ag^+ [3] and Cu^+ [7].

The use of each diffusant ion is accompanied by inherent advantages and drawbacks. Thallium, for example, produces a relatively large increase in index ($+0.1$ to $+0.2$) and can easily produce waveguide depths of up to $10\mu m$, which allows the simple fabrication of multimode waveguides. However, thallium is extremely toxic, and therefore requires more stringent safety considerations during fabrication. Silver ion exchange also produces a large increase in refractive index (+0.1), but has a tendency to reduce to the metallic state if incorporated into the glass in high concentrations, which increases absorption losses in the waveguide. Table 4.3 shows the most commonly used diffusant ions and their properties in silicate glasses.

Ion	Δn$\times10^{-4}$	δn$\times10^{-4}$	W_0 µm	α dBcm^{-1}	Note
Ag^+	1000	0–10	50	<0.2	Tendency to reduce to metallic state
Tl^+	1000–2000	0–50	12	<0.1	High toxicity
Li^+	120	2	10–70	1	High losses
K^+	90	2–20	15–20	<0.1	Low Δn
Rb^+	150–200	2–10	15	0.1	-
Cs^+	400	2	8	0.2	Low diffusion rates, surface degradation

Table 4.3: Properties of diffusant cations, from reference [15]

Where δn is the birefringence, W_0 is the attainable waveguide depth, and α is the optical loss.

The following work with TIE requires the production of waveguides, which support only a single-mode in depth. Taken on its own, this requirement allows the use of any of the above diffusant ions, as the number of modes supported by the waveguide is a function of Δn and the depth of the waveguide. A single mode waveguide could therefore be produced us-

ing any of the above diffusant ions, by simply tailoring the depth of the waveguide.

To decide upon the correct diffusant ion, some practical assertions must be made. Firstly, a diffusant ion that produces a small Δn is more suited to the fabrication of single-mode waveguides, and secondly, a diffusant ion that causes no detrimental effects upon the substrate glass would be preferable. A diffusant ion that fulfills both of these specifications is the potassium ion. Potassium ion exchange produces a relatively low Δn to facilitate the simple production of single mode waveguides, whilst allowing reasonable depth. It has no history of producing surface defects, or other undesirable chemical effects when used with BK7 glass. Potassium nitrate is cheap, commercially available in high purity form (99+% KNO_3) and melts at 333°C which is below the T_g of most silicate glasses.

4.2.3 Properties of Substrate Glass

TIE as a process for the production of optical waveguides has been used for over thirty years. In this time there has been relatively little progress in the production of glasses with compositions specifically designed to improve ion exchange characteristics [15]. Some work has been completed on the production of new glasses with individually tailored properties, for example: glasses doped with fluorine to inhibit the reduction of silver ions after silver ion exchange, or glasses with increased sodium content to reduce waveguide production times. These glasses are still in their infancy, and for this reason information on the glass, and the glass itself, are not as readily available as the more established glasses.

A good candidate glass for TIE has to adhere to a number of specifications:

- Good optical characteristics
- High mobility of alkali ions within the glass
- High T_g in relation to the melting point of desired ion exchange salt

- Chemically durable with ion exchange salt and other waveguide fabrication processes
- Ability to dope with rare earth ions for lasing applications

A glass that performs well in all of these categories and is both cheap and readily available is Schott BK7. BK7 is one of the predominant glasses for use as a substrate during ion exchange, and consequently has the additional advantage that there is a large catalogue of research work already completed with the glass. The manufacturer Schott, produce the glass in the undoped form and doped with different laser ions in various quantities. Table 4.4 shows a compositional analysis of undoped Schott BK7 [15]. Both undoped and $1.5wt\%$ Nd^{3+}-doped BK7 were used for fabrication of passive and active waveguides during this thesis.

Investigation of Yb^{3+}-doped ion exchanged waveguides began after the initial work with Nd^{3+}-doped waveguide lasers had been completed. It would have been preferable to have performed the ion exchange in Yb^{3+}-doped BK7, as the ion exchange characteristics of this glass were well understood. However, due to complications with the glass manufacturer, it was not possible to purchase Yb^{3+}-doped silicate glass for a period of six months, which would set back research considerably. A compromise was decided upon, as the manufacturer could produce Yb^{3+}-doped phosphate glass. For this reason the Yb^{3+} laser performance was studied using $12wt\%$ Yb^{3+}-doped IOG-1, a relatively new phosphate glass that had been specially developed for active ion doping and ion exchange. The composition of undoped IOG-1 is detailed in table 4.4 [16]. Phosphate glasses are known to be less chemically durable than silicate glasses, with some documentation surrounding the particular problem of ion exchange. However, Veasey et. al. [16], have successfully created Yb^{3+}:IOG-1 and Yb^{3+}–Er^{+}co-doped IOG-1 waveguide lasers using the ion exchange process, proving the reliability of IOG-1 for this purpose.

As discussed in chapter 2, quasi-three-level lasers suffer from an increased threshold power due to the reabsorption loss. The reabsorption loss can be reduced either by cooling the laser gain medium, which is impractical, or

Composition of BK7	
Constituent	wt%
SiO_2	70.36
B_2O_3	11.35
Na_2O	9.55
K_2O	7.05
Ba_2O	0.43
CaO	0.31
Al_2O_3	0.28
SO_3	0.05
MgO	0.01
Fe_2O_3	0.01
Other oxides	0.6

Composition of IOG-1	
Constituent	wt%
P_2O_5	60
Na_2O	24
Al_2O_5	13
La_2O_5	3

Table 4.4: Composition of BK7 and IOG-1 glasses

by reducing the length of the laser gain medium. Within a tapered waveguide the broad section of the taper is the only waveguide region that can support the multimode output of a diode-laser, and for this reason is the only waveguide region that requires doping. The reasonably large size of the tapered waveguide, if uniformly doped, would lead to a large reabsorption loss. However, this loss could be minimised by doping only the broad section, and fabricating the taper and channel sections in undoped glass. A laser of this form (figure 4.1) would benefit from a minimised reabsorption loss, in conjunction with the tapered waveguide benefits of efficient diode-pumping and single-mode output. A 'hybrid' substrate glass with doped and undoped sections can be fabricated by bonding two glass samples together. Glass of this form has been utilised for the production of lossless waveguide splitters fabricated by TIE [17, 18] and has recently become commercially available [19]. After bonding and substrate preparation of the hybrid glass, ion exchange can be utilised to form tapered waveguides.

The hybrid glass produced for this work consisted of $1.5wt\%$ Nd^{3+}-doped BK7 bonded to undoped BK7. The bonding process was extremely simple: $50 \times 30 \times 20mm$ blocks of doped and undoped BK7 were polished to optical quality on the $50 \times 20mm$ face, and were placed side-by-side on an alumina sheet with the polished faces in contact. The glass blocks and the

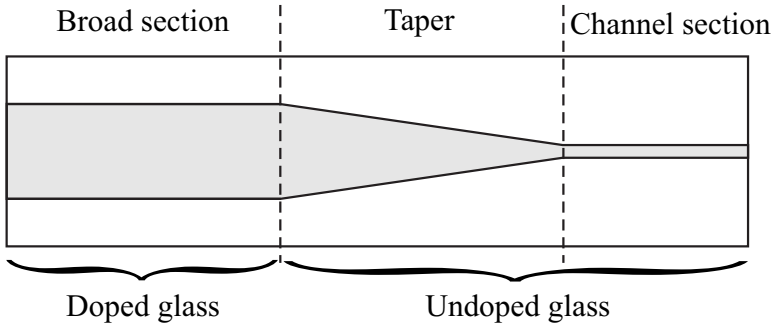

Figure 4.1: Design of a tapered waveguide laser fabricated in hybrid doped/undoped glass

alumina sheet were placed within an oven which was heated to $100℃$ at a rate of $1℃min^{-1}$, and held at this temperature for $15hr$. The oven was then ramped to $715℃$ at a rate of $1℃min^{-1}$ and held at this temperature for $1hr$ before being cooled to room temperature at $1℃min^{-1}$. No deformation of the glass was noticed after the process. The resulting bond was strong enough to allow mechanical dicing and polishing of the hybrid block into $45 \times 15 \times 2mm$ waveguide substrates. A problem due to incorrect photolithography was noticed after the first TIE of the hybrid substrate, and for this reason the substrate was re-polished and a second TIE was completed. Although misaligned photolithography is not desirable, it did allow the bond strength to be rigorously tested, and the substrate was found to be unaffected by this somewhat brutal testing. The laser performance of waveguides fabricated in this glass are discussed in section 4.6.4.

4.3 Diffusion Theory

The following section describes a theoretical model of the concentration profile of diffusant ions within an ion exchanged waveguide. The refractive index profile can then be described, as the concentration and refractive index profiles are directly proportional [1].

The coordinate system used in the following diffusion equations is shown in figure 4.2.

The nonlinear diffusion equation, which describes the concentration pro-

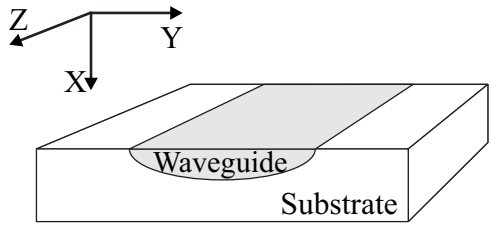

Figure 4.2: Coordinate system used in derivation of diffusion equations

file of diffusant ions 'A' is as follows [20]:

$$\frac{\partial c}{\partial t} + \frac{1}{1-(1-M)\,c}\mu_A \underset{\sim}{E} \cdot \nabla c = \frac{D_A}{1-(1-M)\,c}\nabla^2 c \tag{4.3}$$

where t is time, $c = c(x, y, z, t) = c_A/c_B^0$ is the normalised diffusant ion concentration, c_A is the concentration of diffusant ions, c_B^0 is the concentration of glass ions present in the glass before ion exchange, $M = \mu_A/\mu_B$ is the ratio of the mobilities of the diffusant and glass ions, D_A is the diffusion coefficient of the diffusant ions and E is the electric field, incorporating both externally applied field and any internal field arising from space charge effects. The derivation of equation 4.3 can be found in appendix B.

4.3.1 One Dimensional Solution of the Diffusion Equation

The following section describes the solution of the one dimensional diffusion equation, which is expressed:

$$\frac{\partial c}{\partial t} + \frac{1}{1-(1-M)\,c}\mu_A \underset{\sim}{E}\frac{\partial c}{\partial x} = \frac{D_A}{1-(1-M)\,c}\frac{\partial^2 c}{\partial x^2} \tag{4.4}$$

The equation can be further simplified with consideration of the diffusant and glass ion properties. The mobilities of potassium and sodium ions within BK7 glass are suitably similar making $M \approx 1$:

$$\frac{\partial c}{\partial t} + \mu_A \underset{\sim}{E}\frac{\partial c}{\partial x} = D_A\frac{\partial^2 c}{\partial x^2} \tag{4.5}$$

The boundary conditions relevant to the planar ion exchange are as follows:

$$\begin{aligned} c\,(x,0) &= 0 \\ c(0,t) &= c_s \\ c(\infty,t) &= 0 \end{aligned} \tag{4.6}$$

where c_s is the concentration of the diffusant ion at the surface of the glass.

The solution of equation 4.5 is found using Laplace transform techniques [21] and is given by:

$$\frac{c}{c_s} = \frac{1}{2}\left[\text{erfc}\left(\frac{x-\mu_A E t}{2\sqrt{D_A t}}\right) + \exp\left(\frac{\mu_A E x}{D_A}\right)\cdot \text{erfc}\left(\frac{x+\mu_A E t}{2\sqrt{D_A t}}\right)\right] \tag{4.7}$$

Where erfc is the complementary error function.

During TIE no external field is applied. If the field due to space charge effects is assumed to be negligible [22] then $E = 0$, and the solution can be simplified to:

$$\frac{c}{c_s} = \text{erfc}\left(\frac{x}{W_0}\right) \tag{4.8}$$

where:

$$W_0 = 2\sqrt{D_A t} \tag{4.9}$$

Equation 4.8 is the solution of the simplest form of the nonlinear diffusion equation, which is applicable to planar waveguides produced by TIE. The effective depth of the profile W_0 is found when the argument of the complementary error function equals unity i.e. $c/c_s = erfc(1)$ when $x = 2\sqrt{D_A t}$. Equation 4.9 shows the square root dependence of depth on the ion exchange time.

As already stated, the refractive index and concentration profiles are known

to be linearly related, allowing the refractive index profile of a one dimensional waveguide to be stated as follows:

$$n(x,y) = n_3 + \Delta n \cdot erfc\left(\frac{x}{2\sqrt{D_A t}}\right) \tag{4.10}$$

Where $n(x,y)$ is the refractive index profile Δn the maximum change in refractive index measured at the surface of the waveguide and n_3 is the substrate refractive index.

4.3.2 Two Dimensional Solution of the Diffusion Equation

Two dimensional solutions to the diffusion equation describe channel waveguides, but are complicated by the lack of accurate boundary conditions at the mask edges. For this reason the two dimensional solution is often solved numerically [10]. Assumptions made over the choice of boundary conditions vary depending on the author, and no single definitive solution has been proposed. The problems with boundary conditions are further compounded when considering the constantly changing shape of tapered waveguides, which are the subject of this thesis. The diffusion equation must then be solved in three dimensions, and to date no work has been completed on the solution of this problem. The relevance of channel waveguides to this work must also be considered, as they are used only to verify the results from the tapered waveguide. For these reasons a different approach was taken to the solution of the two dimensional diffusion equation.

Weiss and Srivastava [23] experimentally derived the two dimensional refractive index profile of a TIE channel waveguide:

$$n\,(x,y) = n_3 + \Delta n \exp\left(\frac{-x^2}{d_x^2}\right) erfc\left(\frac{y}{d_y}\right) \text{ for } y \geqslant 0 \tag{4.11}$$

Where $n(x,y)$ is the refractive index profile, n_3 is the substrate refractive index, Δn is the maximum refractive index measured at the surface and centre of the waveguide and d_x and d_y are the $1/e$ half width and $erfc(1)$

depth of the waveguide respectively.

Equation 4.11 was formulated by computer modelling TIE channel waveguides fabricated using various mask openings and exchange times. The effective indices were calculated and compared to the effective indices of the waveguides measured using a prism coupler. Differences between the calculated and measured indices were reduced by iterating the calculation until agreement was found.

4.4 Fabrication

The samples produced by TIE underwent almost identical fabrication steps. The only differences between samples were the 'patterning' of the sample i.e. planar, channel or tapered waveguide and the type of substrate glass used. The following section details the standard fabrication technique used for the production of tapered waveguides by TIE.

4.4.1 Sample Preparation

Blocks of undoped BK7, 1.5wt% neodymium-doped BK7 and 12 wt% ytterbium-doped IOG-1 were purchased from HV Skan, the UK Schott glass supplier. Hybrid $1.5wt\%$ neodymium-doped BK7/BK7 glass was fabricated in house. The glass blocks were cut into $2mm$ thick samples and the top surface was polished to optical quality. If photolithography was required on the sample, one edge was also polished to act as a reference to attain parallelism of the waveguide structure with the substrate side-wall, which in turn can be used to ensure perpendicularity of the substrate end-faces to the waveguide.

The polished sample requires cleaning in readiness for the fabrication of waveguide structures. Residual polishing wax was removed by a $10min$ clean in 1,1,1 trichloroethane in a room temperature bath. Organic impurities are removed with a $20min$ clean, at $50°C$ in acetone, under ultrasonic agitation. As acetone evaporates it precipitates water vapour from the air,

causing dirt to accumulate on the samples surface. To prevent this effect, the sample is rinsed in isopropanol before the acetone can evaporate. The residual isopropanol is then removed by washing the sample for 2 minutes, in running deionised (DI) water. The sample is then dried in a $120℃$ oven for $30min$.

At this point the sample should be clean of any organic impurities, however, there will be a number of inorganic particulates on the samples surface. These can be removed in one of two ways: a 'Piranha' wash, or a wash in fuming nitric acid. The Piranha wash is a 4:1 mixture of sulphuric acid and hydrogen peroxide, held at $60℃$ for 20 minutes. It is effective, but highly exothermic, which can crack samples through thermal shock. After some problems with samples cracking, it was decided to use a fuming nitric wash. The fuming nitric wash is carried out in 100% nitric acid for 3 minutes at room temperature. This wash has a number of advantages: it is as effective as Piranha, does not adversely affect the samples, requires less time and is less complicated as no mixing of chemicals is required. Both of the washes require a dry sample, as any water present on the sample will initiate a strong exothermic reaction. After the inorganic particulates have been cleaned from the sample, it is washed in running DI water to remove residual acid, and dried in a $120℃$ oven for 30 minutes.

4.4.2 Deposition of an Ion Exchange Mask

The production of channel and tapered waveguides by TIE, requires a system of selectively blocking diffusant ions from reaching the surface of the glass. An 'ion exchange mask' is utilised for this purpose. The ion exchange mask can be made of any material that is stable, does not react with any of the chemicals used in the fabrication process and is readily added to, and removed from, the surface of the glass. Aluminium and titanium are predominantly used as they are both stable, relatively easy to evaporate and their acid etching properties are well understood. Aluminium was used during this thesis, as it possesses a low melting point and is relatively cheap. A $250nm$ thick layer of aluminium has been shown to fully block the diffusant ions [13]. A layer of this thickness was coated onto the

surface of the glass using an Edwards 309 thermal evaporator.

4.4.3 Photolithography

Standard photolithography is the delineation of a desired pattern onto the samples surface. In its broadest sense it is a three step process: the deposition of a layer to be patterned (section 4.4.2), the deposition and patterning of a photoresist layer, and finally, the transfer of the pattern from the photoresist onto the lower layer.

Once the mask layer has been applied, a layer of photoresist, a light sensitive polymer, is spun onto the sample. Layers of photoresist are produced by dripping the liquid photoresist onto the surface of the glass, then spinning the sample to produce a homogeneous layer. The thickness of the layer is defined by the spin speed and duration. A $1\mu m$ thick layer of Shipley-1813 photoresist was created by spinning at $6000rpm$ for a duration of $60s$. A layer of this thickness allows the reproducible fabrication of the $2.5\mu m$ wide channels used with this work. After spinning, the sample is 'soft baked' at $90^{\circ}\mathrm{C}$ for $30min$, which hardens the photoresist, reducing its viscosity and allowing it to be contacted to a photolithographic mask without sticking. A pattern from the photolithographic mask detailed in appendix B, is transferred into the photoresist using a mask-aligner. Ultraviolet (UV) exposure causes the photoresist to dissolve when developed, which exposes the aluminium mask. Exposure times between 10.5–$12s$ were used depending on the UV intensity, which ranged between 3–$9Wcm^{-2}$, depending on the age of the UV bulb. The patten in the photoresist is opened by developing in Shipley MF-319 developer for $50s$, followed by a wash in DI water to stop further development. Finally the sample is 'hard baked' at $120^{\circ}\mathrm{C}$ for $30min$, which dries the sample and removes all solvents from the photoresist, producing a hard, acid resistant layer.

Transfer of the pattern from the photoresist into the ion exchange mask is completed by etching the aluminium in a mixture of acids tailored for the removal of aluminium. A $90s$ etch for $3min$ at $60^{\circ}\mathrm{C}$ is required to open the

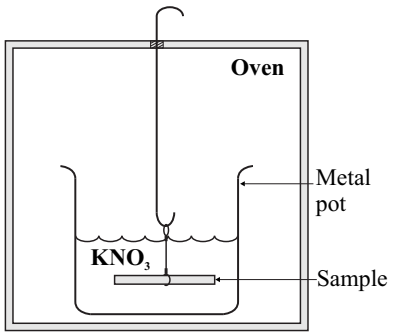

Figure 4.3: Schematic of the apparatus used to produce TIE waveguides

aluminium film, followed by a wash in DI water to remove residual acid. The now redundant photoresist layer is removed with a $20min$ clean, at 50℃ in acetone, under ultrasonic agitation. The sample is rinsed in isopropanol, then DI water and finally dried for $30min$ in a 120℃ oven.

4.4.4 Production of Waveguides by TIE

TIE from a molten salt is a particularly straightforward fabrication technique. A pot is filled with potassium nitrate to a depth of approximately $5cm$. The pot must be metal - in this case stainless steel - as the potassium nitrate adheres to the sides of the pot, which causes glass pots to shatter as the potassium nitrate contracts during cooling. The sample is held with a stainless-steel wire noose, attached to a hook. The entire apparatus is held within an Instron SFL ion exchange oven (figure 4.3).

The oven is turned on and ramps up to 395 ± 2℃ at 6℃min^{-1}. After approximately $1.5hr$ the contents of the oven reach thermal equilibrium. The sample is submerged in the salt and TIE begins. An ion exchange time of $12hr$ was found to produce a waveguide depth that supported a single mode for propagation at a wavelength of $1.06\mu m$ [23]. After $12hr$ the sample is raised above the salt and the oven is shut down and allowed to cool to room temperature over an hour, again at a ramp rate of ≈ 6℃min^{-1}, to avoid problems due to thermal shock. Faster ramp rates may cause damage and were not investigated during this thesis. Once the sample has cooled to room temperature it is removed from the oven, the residual

potassium nitrate is washed off in DI water and the sample is dried in a $120^{\circ}\mathrm{C}$ oven. Patterned samples require a $3min$ etch in aluminium etchant at $60^{\circ}\mathrm{C}$ to remove the ion exchange mask, before being washed and baked to dry.

4.4.5 Fabrication of TIE Waveguides in IOG-1 Glass

Due to the different composition of IOG-1 glass, a different TIE duration is required for the production of single mode waveguides at the Yb^{3+} laser wavelength, although all other fabrication steps are identical. The fabrication of these waveguides followed the work of Veasey et. al. [16], and required a temperature of $375^{\circ}\mathrm{C}$ and a TIE duration of $5hr$.

The undoped-BK7, Nd:BK7 and the hybrid Nd:BK7/BK7 exhibited no visible surface degradation due to the TIE process. The only visible indication that TIE had been completed was a slight swelling of the substrate's surface. Waveguides fabricated within IOG-1 glass by TIE exhibited severe surface degradation after the ion exchange in the form of white patches that resembled etch damage, and large cracks up to $\approx 3\mu m$ in depth. Further to this surface damage, it was found that the ion exchange sensitised the glass to the aluminium etchant used to remove the ion exchange mask. Consequently, after removal of the mask it was found that the waveguides had also been removed.

Phosphate glasses are known to be less chemically durable than silicate glasses [16], and are known to react with various chemicals used during fabrication of TIE waveguides. IOG-1 was developed for the production of active waveguides through the ion exchange process and it was therefore surprising to find extensive damage. Discussion with the glass manufacturers and Dr. Norman Sanford from N.I.S.T. (Boulder, Colorado), led to the conclusion that the damage is caused by inclusion of water in the glass during fabrication. Although water itself does not damage the glass, it appears to sensitise the glass to damage from the ion exchange salts and the various acids used during fabrication. For this reason attempts were made to remove water from all fabrication equipment and from the ion

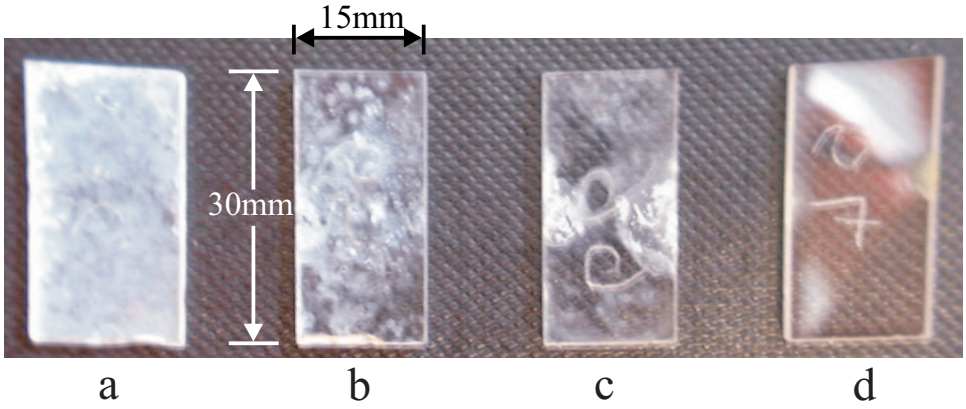

Figure 4.4: IOG-1 glass post-TIE, a/ no aluminium in melt, b/ $\approx 0.02g$ aluminium included in melt, c/ $\approx 0.04g$ aluminium included in melt, d/ IOG-1 heated in oven, but no TIE

exchange salt. One problem is that water is required as a solvent to remove excess ion exchange salt from the substrate after TIE. Although this processing step could not be removed, it was minimsed by washing the sample with a DI water gun, which allows faster removal of the salt than washing the substrate in a weir. Future work with this glass may benefit from investigation into other solvents for the removal of the salt; methanol may be a promising solution, as like water, it is a polar-covalent molecule that may dissolve the salt. Other steps for drying the sample were also followed, and involved: baking the sample at 120°C for at least $2hr$ before any processing step, baking the ion exchange salt at 395°C for $12hr$ in a nitrogen atmosphere prior to TIE and storing the sample in a desiccator between processing steps.

Improvements in the surface degradation were also found by including aluminium wire in the ion exchange salt, as the aluminum appears to act as a gettering agent, and in this way removes water dissolved in the salt. Figure 4.4 shows the surface degradation of four planar TIE samples with increasing amounts of aluminium included in the melt. Further work may benefit through the use of an aluminium source with a greater surface area than wire. Aluminium powder, although possessing the greatest surface area per weight, may settle on the surface of the substrate and block the ion exchange. A more appropriate solution may be the use of aluminium 'lump' that is readily purchased, and has a large surface area but will not

float in the molten salt.

Further work is required to improve the ion exchange of IOG-1 glass. Only one sample, which will be discussed in section 4.6.3, survived the ion exchange process with little degradation.

4.5 Direct Characterisation

Measurement of the concentration profile, and therefore the refractive index profile, is possible through the use of secondary ion mass spectroscopy (SIMS). SIMS analysis utilises a pulsed beam of ions to bombard the surface of a test sample, which etches an $\approx 50\mu m$ diameter pit into the surface of the sample. The constituents of the pit are trapped magnetically and analysed with a mass spectrometer to determine which elements are present, and their concentration. The etch rate is calculated by dividing the total pit depth (measured by interferometric techniques) by the total number of pulses. An etch rate of $\approx 1nm$ per pulse was measured in BK7, with an overall etch of $\approx 4\mu m$ required to provide sufficient data to fit to a theoretical profile. An overall process time of $\approx 8hr$ was required per TIE sample, making SIMS analysis very expensive, and for this reason only two TIE samples were analysed: sample 'PL' a planar sample, and sample 'BC' that contained $175\mu m$ wide broad channels. Both samples were fabricated in undoped BK7, under identical conditions using the standard procedure outlined in section 4.4.

SIMS does not produce a value of the actual concentration, and instead produces a value termed the 'count'. The count is a figure which incorporates the concentration of the detected element in each pulse, the sensitivity of the mass spectrometer to that element and the magnitude of the ion beam current. It is possible to calibrate the profiles by analysing a sample of known ion concentration, if such a sample is available. However, calibrating SIMS data generated from TIE waveguides is straightforward as the maximum index increase n_s at the surface of the waveguide is known for K^+–Na^+ ion exchange in BK7 [23].

SIMS analysis measures the concentration of an ion through the depth of the sample. The one-dimensional index profile $n(x)$ of a TIE waveguide can be modelled by altering equation 4.8, assuming that the diffusant ion concentration is linearly related to the refractive index change [1]:

$$n(x) = n_3 + \Delta n \text{erfc}\left(\frac{x}{W_0}\right) \tag{4.12}$$

Where n_3 is the refractive index of the substrate, Δn is the maximum refractive index at the surface of the waveguide, x is the coordinate in the depth of the sample and W_0 is the $erfc(1)$ depth of the waveguide.

Equation 4.12 was fitted to the calibrated SIMS data using a least squares method and commercially available computational software. The least squared method is a powerful tool for attaining the closest fit, but the value itself does not allow great insight into the quality of the fit. For this purpose a straightforward method was devised to allow calculation of the quality of fit. The residual r is defined as the magnitude of the difference between the SIMS data point x_s and the fitted data point x_f:

$$r = \sqrt{(x_s - x_f)^2} \tag{4.13}$$

The residual is expressed as a percentage of the initial data point, to gain the percentage residual r_p:

$$r_p = \frac{r}{x_s} \times 100 \tag{4.14}$$

The average percentage residual $\bar{r}_p$, is a measure of the average percentage error between the fitted profile and the raw data, which is expressed:

$$\bar{r}_p = \frac{1}{n}\sum_{i=1}^{n} r_{p_i} \tag{4.15}$$

Where n is the number of data points. In an attempt to be concise, this value will be called the 'error in fit'. A good fit is shown by a low $\bar{r}_p$, with a value $\bar{r}_p = 0$ indicating a perfect fit.

4.5.1 Discussion of SIMS analysis

Figures 4.5 and 4.6 show the calibrated SIMS data and theoretical profiles generated for both samples. The fitting procedure allowed calculation of the $erfc(1)$ waveguide depth for the planar and broad channel waveguide, which were $5.3 \pm 0.6\mu m$ and $4.7 \pm 0.8\mu m$ respectively.

An error in fit, summarised using the $\bar{r}_p$ value, of 12.0% and 16.6% was calculated for the planar and broad channel respectively. The error in fit is larger than that attained for later work with indiffused waveguides (chapter 6). The main difference in the fit is located within the first $\approx 1\mu m$ of the profile, where theory predicts a shallower curve than that measured by SIMS analysis. However, the tail of the profile attains a much closer fit to theory. The cause of the steeper curve measured by SIMS may lie with the initial assumption made to allow calculation of the one-dimensional diffusion profile. The mobilities of the Na^+ and K^+ ion, although similar, are not exactly equal as was assumed. The effect of an unequal ionic mobility is a stalling of the ion exchange process. The sodium ions diffuse out of the glass at a faster rate than the potassium ions can diffuse into the glass, which leads to the formation of a space charge region below the surface of the glass. The space charge regions produces an electric field which is orientated in such a way that the indiffusing K^+ ions are assisted in their diffusion, whereas the diffusion of the Na^+ ions is inhibited [5]. The increased rate of K^+ diffusion, and reduced rate of Na^+ diffusion, reduces the space charge effect, and therefore the electric field, until equilibrium is reached. This process of increasing and decreasing diffusion occurs over the entire duration of the ion exchange and may account for the difference between the SIMS profile and the theoretically expected profile. However, the error in fit is slight and limited to the first micron of the sample's depth which leads to the conclusion that the theoretical profile is sufficient for the description of the refractive index profile of a TIE waveguide. The relative waveguide depths attained for the broad channel and planar waveguide are as expected from theory, i.e. that planar waveguides attain a greater diffusion depth than channel waveguides.

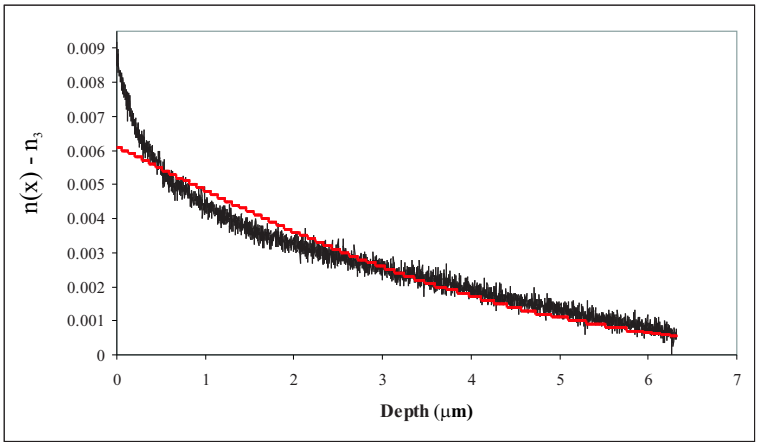

Figure 4.5: SIMS data for sample PL in black, theoretical profile in red

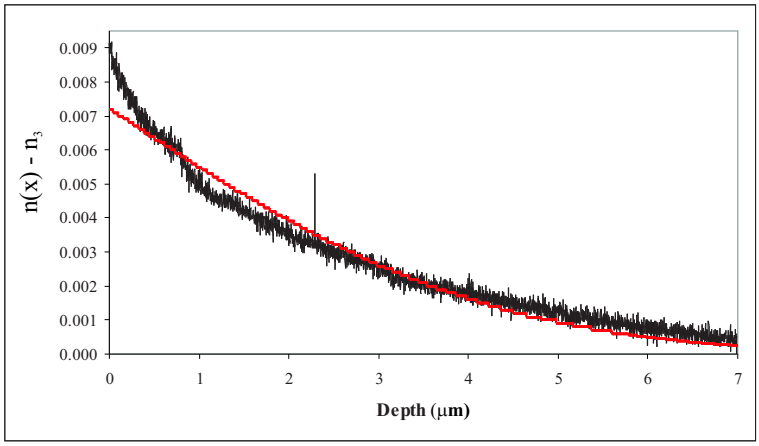

Figure 4.6: SIMS data for sample BC in black, theoretical profile in red

The SIMS analysis completed for the TIE waveguides exhibits a reasonable correlation with the theoretically derived index profile, which allows confidence in both techniques. The lateral resolution of SIMS does not allow analysis of the channel section of the tapered waveguide, which may have allowed confirmation that a taper in the depth of the sample is created due to ion exchange through different mask apertures. The SIMS analysis of TIE waveguides has proved useful when analysing samples fabricated by field-assisted ion exchange (section 5.6.1), as it allows the vastly different refractive index profiles gained from each method to be highlighted.

4.6 Optical Characterisation of TIE Waveguides

The following sections list the optical characterisation techniques used to analyse TIE waveguides. The features on each of the waveguides used during this investigation are listed in table 4.5.

Sample number	Substrate glass	Features	Mask group from appendix B
LT1	Nd:BK7	$175\mu m$ wide linear tapers and $2.5\mu m$ wide channels	Group 1
PLT	Nd:BK7	175, 200 & $250\mu m$ wide parabolic tapers, 175, 200 & $250\mu m$ wide linear tapers and $2.5\mu m$ wide channels	Group 3
LT2	Nd:BK7	175, 200 & $250\mu m$ wide linear tapers and $2.5\mu m$ wide channels	Group 1
BC	Nd:BK7	$175\mu m$ wide broad channels	Group 2
YBIOG	Yb:IOG-1	175, 200 & $250\mu m$ wide linear tapers and $2.5\mu m$ wide channels	Group 2
HYBK7	Hybrid Nd:BK7	175, 200 & $250\mu m$ wide linear tapers and $2.5\mu m$ wide channels	Group 2

Table 4.5: Features of TIE waveguides

Sample LT1 was the first sample produced during this thesis and was used to characterise the simple linear tapers that were available at the time. PLT was developed to investigate the adiabatic properties of parabolic and linear tapers of different widths. Linear tapers were found to outperform

parabolic tapers for widths $> 175\mu m$ and for this reason later waveguides were fabricated with linear tapers only. Diode pumping of sample LT1 was limited by the low pump absorption within the $6mm$ long broad section, and for this reason sample LT2 was fabricated with a $20mm$ long broad section. Linear tapers of different widths were fabricated on sample LT2 to test the effect of taper width on the laser performance. YBIOG and HYBK7 were fabricated to test the performance of Yb^{3+}-doped IOG-1 and the hybrid glass respectively.

4.6.1 Preliminary investigation of a Tapered Waveguide

Preliminary optical characterisation was carried out using the apparatus shown in figure 4.7.

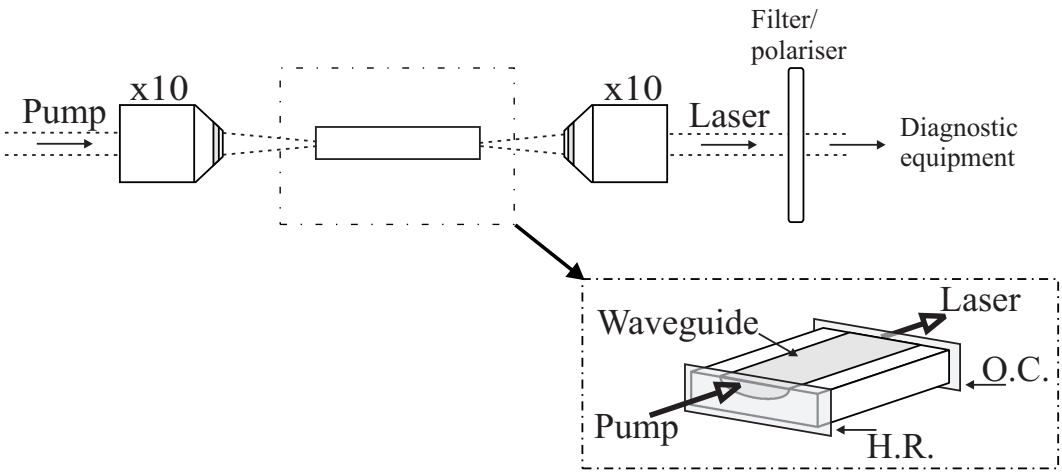

Figure 4.7: Apparatus for optical characterisation. Inset, close-up of laser cavity

Initial investigation of the tapered waveguide laser was completed using sample LT1. The sample was fabricated with six identical tapers, each consisting of a $175\mu m$ wide, $6mm$ long broad channel, a $12.5mm$ long linear taper and a $2.5\mu m$ wide, $6mm$ long channel section. $2.5\mu m$ wide channels were also fabricated on this sample for comparison purposes.

Light from a titanium sapphire laser was end launched into a channel, or the narrow end of a taper, with a $\times 10$ microscope objective found to provide the greatest launch efficiency, which produced a spot size of $\approx 3\mu m$.

Another $\times 10$ objective was used to focus the output from the waveguide onto diagnostic equipment.

A laser cavity was created by bonding dielectric mirrors onto the end faces of the sample, using the surface tension of a very thin layer of fluorinated liquid for adhesion. Threshold measurements were completed using two highly reflecting (HR) mirrors with $> 99.9\%$ reflectivity at the lasing wavelength ($\approx 1.06\mu m$) and a transmission of 87% at the pump wavelength ($\approx 808nm$).

The titanium sapphire laser was tuned to $808nm$ and a RG1000 filter (transmittance of $< 10^{-5}$ at $808nm$, and 68% at $1.06\mu m$) was placed in the output beam to block residual pump light. The laser output was detected using a silicon photodiode and displayed on an oscilloscope. Optimisation of the launch was completed by adjusting the position of the waveguide and tuning the titanium sapphire laser to find the lowest threshold power at the onset of lasing. The incident threshold power was measured at a position before the launch objective.

The launch efficiency of this optimised configuration was measured to allow calculation of the absorbed power threshold. The titanium sapphire laser was tuned off the Nd^{3+}absorption. The RG1000 filter and end face mirrors were removed and a masked power meter replaced the silicon photodiode. A mask was used to ensure that only light emitted from the waveguide was incident on the power meter. The launch efficiency into a channel was calculated at 78%. A launch efficiency of 78% was also assumed for the tapered waveguide, as the channel waveguide is identical in size to the channel end of the tapered waveguide. Taking the launch and absorption efficiencies into account with the transmission of the input mirror and the launch objective, produced absorbed power thresholds of 3 and $5mW$ for a channel and taper respectively. The higher threshold measured for the taper is due to the pump beam diverging after exiting the $6mm$ long narrow section of the taper, meaning a greater area is subject to pumping.

Investigation of the lasing properties required optimisation of the output

coupler (OC). Four sets of output mirrors were available, with transmission values ranging between 14–32% . The threshold and output power of a tapered waveguide laser were investigated for each output mirror, with a transmission of 23% found to provide the optimum output coupling for the available pump power. Absorbed power thresholds of 5 and 15mW were measured with this output coupler for a channel and taper respectively.

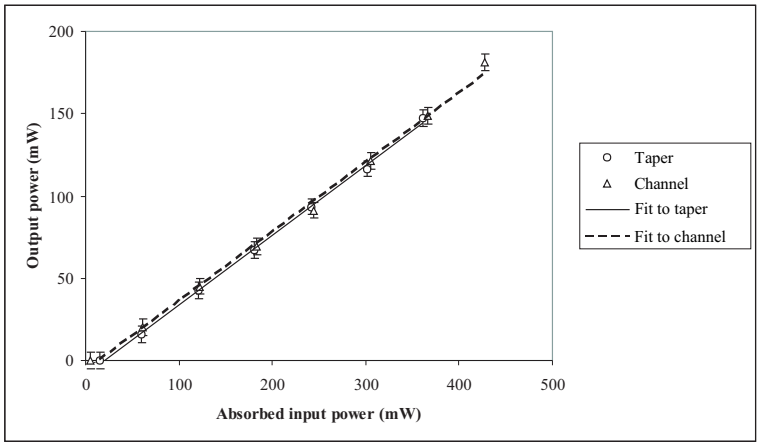

Figure 4.8: Slope efficiency of a tapered and channel waveguide fabricated on sample LT1

Almost identical slope efficiencies, with respect to absorbed power, were calculated for the tapered waveguide and channel laser of $42 \pm 3\%$ (figure 4.8). As discussed in chapter 2, the slope efficiency can be related to the waveguide loss through the equation:

$$\eta_{SE} = \frac{\lambda_P}{\lambda_L}\left(\frac{-\ln R}{-\ln R + L}\right)\eta_{PL}\eta_q \tag{4.16}$$

Where λ_P is the pump wavelength, λ_L is the laser wavelength, R is the reflectivity of the output coupler and L is the remaining fractional round-trip loss, which is assumed to be dominated by the propagation loss. A 100% spatial overlap between the pump and laser modes ($\eta_{PL} = 1$) and a 100% quantum efficiency ($\eta_q = 1$), were assumed.

Calculation of the round trip propagation loss (L_p) in $dBcm^{-1}$ is calculated using the value of L from equation 4.16 with:

$$L_p = \frac{-10\log(e^{-L})}{2l_c} \tag{4.17}$$

Where l_c is the cavity length in cm.

A propagation loss of $0.2dB$ was calculated for both the channel and tapered waveguides. The loss calculation can be confirmed through use of the threshold power equation, as defined in chapter 2. Rearranging equation 2.63, assuming no re-absorption loss and using the assumption that the pump and laser mode radii are identical, which is a reasonable assumption within a channel waveguide produces:

$$P_{th} = \frac{\pi hc}{4\sigma\tau\lambda_P}\left(L - \ln R\right) 2\omega_{Lx}\omega_{Ly} \tag{4.18}$$

Where h is Planck's constant, c is the speed of light, σ is the stimulated emission cross-section, τ is the upper laser level lifetime, λ_P is the pump wavelength, R is the mirror reflectivity, ω_{Lx} is the laser mode radius in the x-direction and ω_{Ly} is the laser mode radius in the y-direction. L is the round-trip propagation loss, identical to that in equation 4.16.

Use of the calculated laser mode radii of the channel waveguide, the measurement of which is discussed later in this section, with the absorbed threshold power of $3mW$ measured for this waveguide in a laser cavity formed from two HR mirrors, produces a loss of $0.2dBcm^{-1}$. As an identical value was calculated for the propagation loss by both methods, it can be seen as an accurate description of the propagation loss within the TIE waveguide.

Although the tapered waveguide suffered from a higher threshold power than the channel waveguide, the slope efficiency was nearly identical, implying negligible additional loss due to the tapered structure. The implication of this result is that the taper must be operating adiabatically. To confirm the modal properties of the tapered waveguide laser, the output was investigated using both a CCD camera and a Coherent Modemaster M^2 meter.

Figure 4.9 shows the output from a channel and taper. Both can be seen to

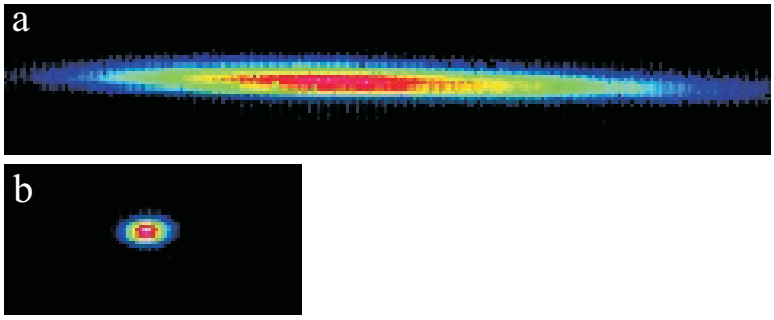

Figure 4.9: Spatial output modes of: a/ $175\mu m$ wide linear taper, b/ $2.5\mu m$ wide channel

be asymmetric and single-lobed, where the single-lobe is an indication of single-mode operation. The mode radii within the cavity were calculated using Gaussian optics and the mode widths measured on the CCD camera. The mode radii in the x and y direction were calculated at 5x3μm for the channel waveguide and 49x3μm for the tapered waveguide. A highly asymmetric mode was expected (and desired) in the tapered waveguide. The slight asymmetry within the channel waveguide was also expected as potassium ion exchange is naturally asymmetric [23].

Measurements of the M^2 value were used to confirm the near-diffraction-limited nature of the output from the tapered and channel waveguides. Values of $M_x^2 = 1.5$ and $M_y^2 = 1.6$ were measured from the output of the broad section of the tapered waveguide laser. These values improved to $M_x^2 = 1.1$ and $M_y^2 = 1.0$, if the output was obtained from the channel section of the taper. The output from the channel section of the tapered waveguide is comparable to that obtained from a standard channel laser fabricated on the same substrate: $M_x^2 = 1.2$ and $M_y^2 = 1.0$.

It appears that, despite the simple linear design, adiabatic expansion has been achieved. Further work on the optimisation of the taper shape and width is detailed in the following section.

4.6.2 Comparison of Parabolic and Linear Tapers

The theoretical operation of parabolic and linear tapered waveguides was investigated in section 3.5, which concluded that linear and parabolic tapers of widths in the order of $200\mu m$ seem to operate with a similar taper efficiency. The effect of taper shape on laser performance was experimentally investigated using apparatus identical to that in section 4.6.1. Sample PLT was fabricated with linear and parabolic tapers of varying widths (see table 4.6), under identical conditions as sample LT1.

Taper shape	Taper Width (μm)	Taper length (mm)	Channel length (mm)	Threshold Power (mW)	Slope Efficiency (%)
linear	175	11.0	15	40	18
linear	200	14.3	11.7	35	21
linear	250	22.3	3.7	42	19
parabolic	175	11.0	15	34	23
parabolic	200	14.3	11.7	55	11
parabolic	250	22.3	3.7	115	5
channel	2.5	—	46.0	27	22

Table 4.6: Features and laser performance of sample 32

The tapered waveguides in sample PLT were fabricated with a $2cm$ long broad section, as it was found that the $6mm$ length of the broad section, as used with sample LT1, was too short to allow reasonable absorption of a diode-pump source. The use of a $2cm$ long broad section would therefore allow efficient pumping with either a titanium sapphire, or a diode laser. However, this requirement substantially increases the substrate size, and substrates over $45mm$ cannot be fabricated due to limitations of the processing equipment. For this reason the $2cm$ length of the broad channel set a $25mm$ limit on the combined length of the taper and the channel section. As discussed in chapter 3, parabolic taper length is related to width through the equation [27]:

$$L = \frac{W^2 n_3}{2\alpha\lambda_0} \tag{4.19}$$

Where W is the taper width, L the taper length, λ_0 the free-space wavelength, n_3 is the refractive index of the substrate and α is a coefficient that determines the adiabatic performance of the taper. The parabolic tapers were designed with an α value of 2, producing a taper length of $11mm$ for a $175\mu m$ wide taper, which is similar to the length of taper used on sample LT1 ($12.5mm$). Linear tapers were then designed with the same length and width as the parabolic tapers to allow fair comparison of their properties.

The taper shapes were evaluated by a comparison of threshold power and slope efficiency, the results of which are shown in table 4.6. The best results of a standard 2.5μm wide channel are also listed for comparison. Graphical representations of the slope efficiency and threshold power with respect to absorbed power, are shown in figures 4.10 and 4.11 respectively. The linear tapers operate with a comparable slope efficiency and threshold power to the channel waveguide, independent of the taper width. The laser performance of the 175μm wide parabolic taper was superior to every linear taper, however, as the width of the parabolic taper increases there is a sharp drop in the slope efficiency, accompanied by a sharp increase in the threshold power.

The effect of the taper shape and maximum taper width on the propagation loss is shown in figure 4.12. A loss of $0.25dBcm^{-1}$ was calculated for the channel waveguide, which is a typical value for a TIE waveguide of this type. Knowledge of the background propagation loss allows calculation of the additional loss due to the tapered structure. The similar slope efficiency measured for each linear taper leads to a similar taper loss, with a maximum of $1.4dB$. However, the loss due to the parabolic taper rises to $\approx 4dB$ for the $200\mu m$ wide taper, and increases to $\approx 14dB$ for the $250\mu m$ wide taper. Figure 4.12 indicates that increasing the parabolic taper width causes an almost linear increase in the taper loss, whereas the loss due to a linear taper is reasonably constant for the widths investigated here. The additional loss caused by the parabolic tapers was attributed to non-adiabatic operation, an assumption that was reinforced by the distinctly multimode operation observed when viewing the output with a CCD camera (figure 4.13).

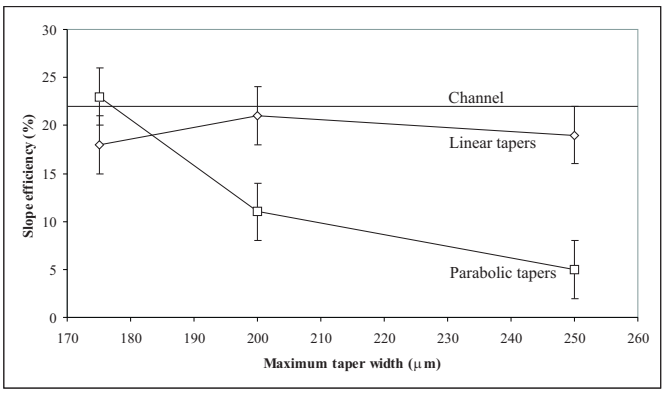

Figure 4.10: Slope efficiencies of linear and parabolic tapered waveguides and a channel waveguide

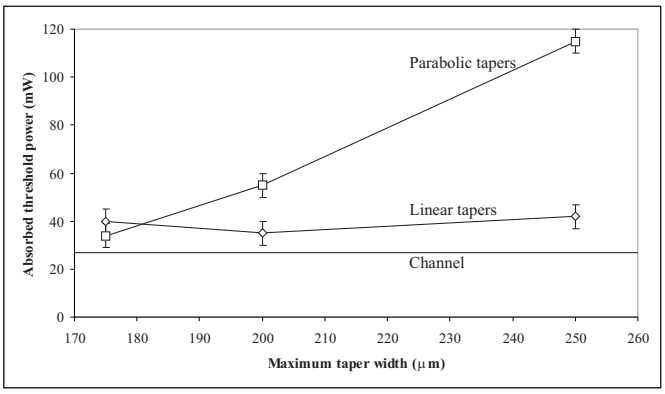

Figure 4.11: Absorbed threshold power of linear and parabolic tapered waveguides and a channel waveguide

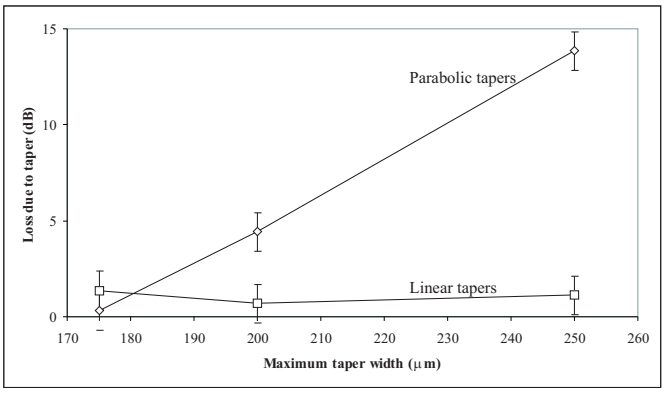

Figure 4.12: Propagation loss of linear and parabolic tapered waveguides and a channel waveguide

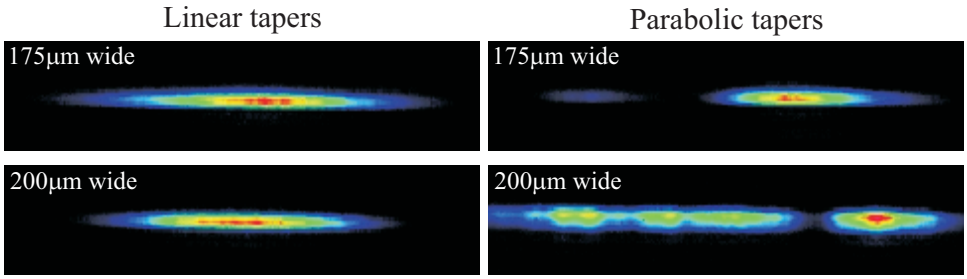

Figure 4.13: Spatial output modes of linear and parabolic tapers

The laser performance of the linear and parabolic tapered waveguides indicates that parabolic tapers are most suited to small expansions of a laser mode ($\leqslant 175\mu m$) and they may even out-perform linear tapers over this range. However, there is a significant drop-off in the performance of parabolic tapers at expansions over $175\mu m$. Linear tapers have been shown to operate adiabatically up to widths of $250\mu m$ for an expansion coefficient of $\alpha = 2$. As no drop-off in performance has been seen up to this point, it seems reasonable to assume that the performance of linear tapers will be maintained past the $250\mu m$ tested here. The substrate size is limited by the fabrication facilities, so it would not be possible to design wider linear tapers using the parabolic equation of Milton and Burns (equation 4.19) with $\alpha = 2$. Increasing the α coefficient would allow wider tapers to be fabricated with lengths similar to that investigated here, although the adiabatic operation of linear tapers with $\alpha > 2$ has not yet been explored.

4.6.3 Waveguides in Ytterbium doped IOG-1

$2.5\mu m$ wide channel waveguides, fabricated in sample YBIOG, were characterised using a titanium sapphire laser as the pump source, and identical apparatus as used in section 4.6.1, although a $6\times$ microscope objective was found to provide a superior launch into the waveguide. Laser cavities were created using either the Fresnel reflectance from the waveguide end-faces ($R = 0.04$), or high reflectance (HR) mirrors at the laser wavelength ($R > 99.9\%$).

Lasing occurred for a range of pump wavelengths between 909–$970nm$.

The laser wavelength was dependant on the reflectivity of the cavity mirrors. Lasing was observed at $1017.5 \pm 1.5nm$ for a cavity that utilised only Fresnel reflections, and also for a cavity with an HR input coupler and output coupling from the Fresnel reflection. Use of an HR mirror for both the input and output coupler produced simultaneous lasing at $1037 \pm 1.5nm$ and $1051 \pm 1.5nm$.

The absorption coefficient at the pump wavelength of $909nm$ was measured spectroscopically at $12.2cm^{-1}$ for the $12wt\%$ Yb-doped IOG-1 glass. The measured absorption coefficient relates to an absorption length of $8.2mm$, and for this reason 100% absorption of the pump was assumed over the $44mm$ long waveguide. The threshold and slope efficiency with respect to absorbed power were measured for each combination of mirror reflectivities, and the results of this analysis are summarised in table 4.7. The launch efficiency and propagation loss were calculated by fitting values to the off-absorption transmission of the channel waveguide, and resulted in a launch efficiency of 60% and a propagation loss of $0.6dBcm^{-1}$.

The spatial output mode of the channel waveguide laser, imaged onto a CCD camera, exhibited a smooth Gaussian profile in both axes, indicating single mode operation, and allowing the validation of the fabrication parameters used to produce these devices. The size of the laser mode at the camera, in conjunction with the known distance between the camera and waveguide end-face, allowed calculation of waveguide mode radii: $W_x = 7.7\mu m$, $W_y = 3.2\mu m$, which were used to calculate the expected threshold power of the channel laser.

Assuming a value of unity for both the pump absorption, and the pump and laser overlap, allows calculation of the expected slope efficiency and threshold power through the use of equations 4.16 and 4.18. The calculated values are listed in table 4.7.

The similarity between the experimental and calculated values of the absorbed threshold power and slope efficiency validates the initial assumption of a 60% launch efficiency and $0.6dBcm^{-1}$ propagation loss. The measured loss is higher than the Nd:BK7 channel waveguide laser ($0.2dBcm^{-1}$),

Cavity type	Absorbed threshold power mW		Slope Efficiency %	
	Experimental	Calculated	Experimental	Calculated
Fresnel/Fresnel	259	176	74	75
Fresnel/HR	194	128	46	65
HR/HR	74	68	–	–

Table 4.7: Laser results for a channel waveguide in IOG-1

but is similar to the $0.5dBcm^{-1}$ measured by Veasey et. al. within similar channel waveguides [16]. The surface degradation due to TIE, although minimal on this sample, may contribute to the measured loss and therefore may be reduced by optimising the TIE fabrication.

The tapered waveguide lasers did not operate under titanium sapphire pumping. The pump laser was launched into the $2mm$ long channel section of the tapered waveguide, however, as the absorption length within this material is $8.2mm$ only $\approx 38\%$ of the pump will be absorbed in the channel section. The remaining pump power entering the taper will diverge, requiring a greater area to be pumped and producing a higher threshold power. Scaling the pump diameter up to typical values within a $175\mu m$ wide taper, increases the threshold power to $\approx 1W$. The titanium sapphire pump laser is limited to powers $< 1W$, so the tapered waveguides could not reach threshold under this low-power pumping. However, access to higher pump powers made available from broad-stripe diode-lasers would allow the successful lasing of these waveguides. The low-loss operation of the channel waveguides coupled with the known adiabatic properties of the linear tapers, allows some confidence in predicting reasonable laser performance from the tapered waveguides.

The operation of a tapered waveguide laser fabricated on a hybrid Yb^{3+}-doped/undoped substrate would also be of great interest, as this may allow the reabsorption loss to be minimised. The properties of the hybrid glass substrate are the focus of the next section.

4.6.4 Tapered Waveguides in Hybrid BK7

The laser performance of the hybrid Nd:BK7/BK7 waveguides was investigated using identical apparatus to that in section 4.6.1, and a titanium sapphire pump source. Figure 4.14 illustrates the $175\mu m$ wide, linear tapered waveguides and $2.5\mu m$ wide channel waveguides that were tested during this analysis. A laser cavity was created by bonding mirrors onto the waveguide end-faces using the surface tension of flurionated liquid for adhesion. An HR mirror was used as the input coupler, with two different output couplers: an HR, and a mirror with 77% reflectivity at the laser wavelength.

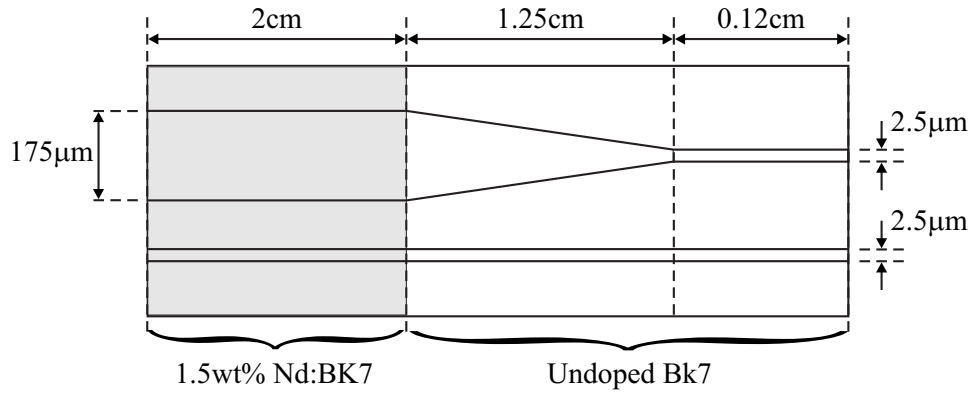

Figure 4.14: Schematic of the waveguides produced in the hybrid Nd:BK7/BK7 glass (sample HYBK7)

Launching into a channel, or the channel end of a taper, was accomplished with a 60% launch efficiency. The pump absorption of the $2cm$ long Nd-doped glass section was measured at 92% for an HR/HR cavity, and was assumed to be 100% for an HR/$R = 77\%$ cavity, as the output coupler is HR at the pump wavelength. Although the hybrid glass is intended for use as a substrate material for quasi-three-level laser operation, this initial investigation utilised the four-level transition of the Nd^{3+} ion to assess the quality of the bonded glass. The slope efficiency and threshold power with respect to absorbed power were measured for both a channel and a tapered waveguide laser, the results of which are listed in table 4.8. The waveguide mode radii were calculated from the radii of the laser output measured on a CCD camera, and the distance between the camera and

the waveguide end-face. Mode radii of $W_x = 5.4\mu m$, $W_y = 3.4\mu m$ were measured for the channel waveguide and $W_x = 47.0\mu m$, $W_y = 3.4\mu m$ for the output from the broad section of the $175\mu m$ wide taper. Both of these results are comparable to the mode radii measured for a channel and a $175\mu m$ wide linear tapered waveguide fabricated in standard Nd:BK7 (section 4.6.1). Single-mode operation was observed for both the channel and tapered waveguide, as would be expected due to the identical fabrication procedures as used for previous BK7 samples. The calculation of the mode radii allowed the loss to be calculated from the threshold power using equation 4.18. The loss was also calculated from the measured slope efficiency using equation 4.16. The results of this analysis are listed in table 4.8

Feature	Absorbed threshold power mW	Slope efficiency %	Loss	
			from SE $dBcm^{-1}$	from P_{th} $dBcm^{-1}$
channel	0.8	50	0.07	0.05
$175\mu m$ wide linear taper	13.4	38	0.13	0.1

Table 4.8: Laser performance of hybrid glass channel and tapered waveguides

The slope efficiency measured for both the channel and tapered waveguide are comparable to those found for sample LT1 (section 4.6.1), which is approximately half the length of the hybrid waveguides. This is an initial indication of the low loss operation of the bond in the hybrid glass. Surprisingly, the hybrid waveguides appear to benefit from a lower loss than the waveguides fabricated within standard Nd:BK7 ($0.2dBcm^{-1}$). The hybrid waveguides were the last waveguides produced during this thesis, and for this reason the low loss may be due to experience gained in TIE fabrication. An alternative reason may be an improved end-face perpendicularity, leading to lower losses as discussed in section 3.5.3. These results lead to the conclusion that the bond loss within this glass is negligible compared to the propagation loss. The tapered waveguide suffers from a slightly higher loss than the channel waveguides, which may be due to imperfections in the bond causing a small degree of higher order mode excitation, followed by the radiation of these higher order modes at the

taper.

Further work is required to investigate the performance of these waveguides at the $946nm$, quasi-three-level transition of the Nd^{3+} ion, which would allow the effect of this glass on the reabsorption loss to be calculated.

The low-loss nature of this bonding process may allow access to some exciting areas of research. The hybrid glass, in conjunction with the properties of the tapered waveguide, presents the possibility of minimising the reabsorption loss and producing single-mode output, whilst allowing efficient end-pumping with a broad-stripe diode-laser. Compact, efficient, ytterbium-doped single-mode, pump lasers operating at the truly three-level $980nm$ wavelength are a requirement for erbium-doped amplifiers. Diode-pumped, tapered waveguide lasers fabricated in hybrid glass, are a possible route to this goal.

4.6.5 Diode pumping of Tapered Waveguides

The goal of the work with TIE tapered waveguides, is the production of waveguides that are compatible with high-power, laser-diode pump sources. Two different broad-stripe diode-lasers were purchased from the supplier, Polaroid. The characteristics of each diode-laser, measured after the collimating fibre lens, are listed in table 4.9.

Diode name	Model no.	Emitter size (slow axis/fast axis) μm	M^2 (slow axis/fast axis)	Maximum Power W
Diode A	382D-1330E-3-1	200×1	39×3.2	4
Diode B	462D-1375E-3-1	100×1	22×1.9	2

Table 4.9: Characteristics of broad stripe diode pump sources

The apparatus used for the following work is shown in figure 4.15. The launch optics comprised a cylindrical focussing lens for the slow axis (lens 1, $f = 19mm$) and a cylindrical focussing lens for the fast axis (lens 2, $f = 6.35mm$).

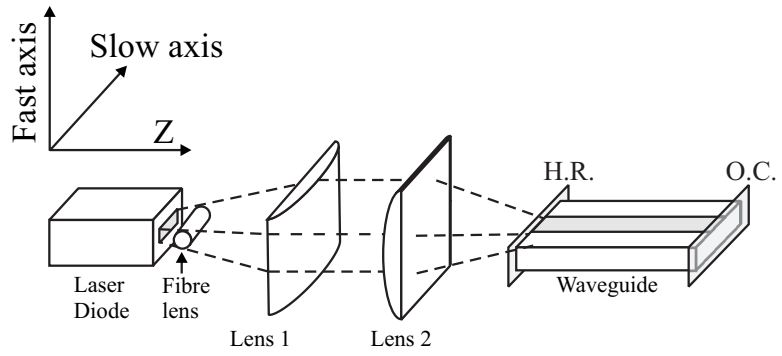

Figure 4.15: Experimental set up for diode-pumping

The diode-pumped performance of sample LT1 was initially investigated using diode A. An output coupler with 23% transmittance, and a HR input coupler were used to create the laser cavity. An incident threshold power of $600mW$ and a maximum output power of $25mW$ were measured. Although a higher threshold power and lower slope efficiency were expected with diode pumping, the degradation in performance was not expected to be this severe. A low launch efficiency and low pump absorption were considered to be the most likely causes of these poor results, as both would be reduced with diode pumping relative to titanium sapphire pumping.

The absorption coefficient measured in bulk $1.5wt\%$ doped Nd:BK7 was found to have a peak absorption coefficient of $0.9cm^{-1}$. Sample LT1 was fabricated with a $6mm$ long broad section over which only 42% of the incident pump power is absorbed. Very little double pass absorption can occur in a tapered waveguide as all power in modes other than the fundamental will be coupled out of the waveguide at the taper. For this reason sample LT2 was fabricated, under identical conditions as used for sample LT1, but with a $2.5cm$ long broad channel to increase the pump absorption to 89%.

The measurement of launch efficiency with a titanium sapphire laser is a straightforward process, as the laser wavelength can be tuned off the Nd^{3+} absorption. The emission from a diode-laser cannot be tuned to this degree, thus waveguides were fabricated in undoped BK7 to allow the diode-laser launch efficiency to be measured. Two $25mm$ long undoped BK7 substrates were used to produce a planar waveguide and a $175\mu m$

wide broad channel waveguide under identical fabrication conditions as used for sample LT1.

Unfortunately, the power output from diode A was found to have dropped to half its original value, so later experiments were completed with diode B. Using diode B and the launch optics described above, a launch efficiency of 30% was measured in an undoped broad channel, this low value being attributed to the NA of the waveguide being unable to confine the relatively large pump divergence in the vertical direction. Lens 2 was replaced with a $f = 12.7mm$ cylindrical lens to reduce the divergence, and produced spot size radii of $108 \times 10\mu m$ in the x and y-directions respectively. The use of the new launch optics produced a 60% launch efficiency in an undoped broad channel at low power, which decreased to 54% at the maximum pump power. The launch efficiency in the planar waveguide was measured at 67% and did not change with increasing power, indicating that the reduction of the launch efficiency in a broad channel at high power, is caused by reduction of the diode-laser beam quality in the slow axis.

Previous work with a titanium sapphire pump source used the $2.5\mu m$ wide channel waveguides for comparison purposes. It is not possible to use channel waveguides for this purpose when diode-pumping, due to the very low launch efficiency into a channel waveguide of this size. A new waveguide laser, sample BC, was produced for comparison purposes, and was fabricated with $175\mu m$ wide, $18mm$ long broad channels in Nd:BK7, under identical conditions as used for sample LT1.

The incident power thresholds of samples LT1, LT2 and BC were almost identical at 250–$300mW$. However, the slope efficiencies were quite different: 27.5%, 12.9% and 2.2% for BC (broad channel), LT2 ($2cm$ long broad section, $175\mu m$ wide taper) and LT1 ($0.6cm$ long broad section, $175\mu m$ wide taper) respectively. The lower slope efficiency of LT1 can be attributed to the low (42%) pump absorption, which was not accounted for in the calculation of slope efficiency. However, the pump absorption of samples LT2 and BC are similar: 89% and 100% respectively, with sample BC achieving a value of 100% due to double-pass absorption. Therefore, the superior

Sample no.	Features	Propagation loss $dBcm^{-1}$	Taper loss dB	η_{PL} %
LT2	175, 200 & 250μm wide linear tapers and 2.5μm wide channels	0.25	0–1.4	49–70
BC	175μm wide broad channels	0.25	–	65

Table 4.10: Results of overlap calculation during diode-pumping

slope efficiency of the broad channel laser, in relation to sample LT2, is not limited to the improved pump absorption. During the slope efficiency calculations a pump and laser mode overlap factor η_{PL} of 100% was assumed, which is a valid assumption when pumping with a fundamental-mode titanium sapphire laser. However, the overlap of the multimode diode-pump and the fundamental-mode laser will be $< 100\%$. The overlap factor was calculated using equation 4.16, assuming a background propagation loss of $0.25dBcm^{-1}$, a pump absorption factor as previously stated, and a taper loss between 0–$1.4dB$; the results of this analysis are listed in table 4.10.

The overlap factor calculated for sample LT2 is dependent on the value assumed for the taper loss, however, it can be as low as 49% which would reduce the slope efficiency in relation to sample BC, which benefits from an overlap of 65%. The decrease in the overlap factor for the tapered waveguide explains the reduction in the slope efficiency of this laser compared to the broad channel laser. The graded index profile gained from the TIE process constrains the fundamental mode of the laser to a greater degree than higher order modes, a phenomenon that is modelled and discussed in section 5.2.1. The overlap factor could be improved through the production of step-index tapered waveguides by field-assisted ion exchange, which forms the basis of the following chapter.

4.7 Summary

The design and fabrication of the first dielectric, planar tapered waveguide laser was discussed in this chapter. The laser performance of the initial linear tapered waveguide exhibited a slope efficiency of 42% and losses of $0.2dBcm^{-1}$, comparable to that of a channel waveguide fabricated on the same substrate. The laser performance of parabolic and linear tapered waveguides allowed calculation of the taper loss for each shape and for taper widths of 175–$250\mu m$. The loss due to a parabolic taper increases with an increase in the taper width, whereas linear taper losses have been shown to be reasonably constant for all the widths investigated. Linear tapers are therefore more suited to diode-end-pumping, and it is reasonable to assume that the taper loss will be maintained for expansion to widths $> 250\mu m$. The adiabatic performance of the linear tapered waveguides has been verified by the low-loss operation and the measured single-mode laser output.

Channel waveguides fabricated in Yb^{3+}-doped IOG-1 glass have also exhibited good laser performance with propagation losses of $0.6dBcm^{-1}$ and a maximum slope efficiency of 75%. The threshold power of the Yb^{3+}-doped channel waveguides are higher than that measured for identical devices fabricated in Nd:BK7, due to the reabsorption loss of this quasi-three-level laser ion. The available pump power was not sufficient for the tapered waveguide lasers to reach threshold, however, the higher pump power available from a diode-laser should allow lasing. The low loss nature of the channel waveguides combined with the known adiabatic properties of the linear tapered waveguides allows some confidence in predicting reasonably efficient performance from these devices.

A new hybrid glass has been fabricated and early testing of this glass has produced losses of $0.05dBcm^{-1}$ and $0.1dBcm^{-1}$ for a channel and a tapered waveguide laser respectively. Both waveguide lasers exhibit a slope efficiency comparable to that measured for waveguides fabricated in standard Nd:BK7. The low loss indicates a good bond quality, and should allow further testing of the laser performance at the $946nm$ Nd^{3+} transi-

tion. However, a more useful laser device may be formed from tapered waveguides fabricated in a hybrid Yb^{3+}-doped/undoped glass substrate, allowing access to the highly three-level $980nm$ transition for pumping erbium doped amplifiers.

Initial results from a tapered waveguide laser, end-pumped with a broad-stripe diode-laser, have shown a degradation in laser performance in relation to titanium sapphire pumping. The mechanisms involved with the performance degradation have been investigated, and imply that an improvement in the performance could be attained through the use of wider tapers to improve launch efficiency, a longer broad section to improve pump absorption and a move to a step-like index profile to improve the pump and laser overlap. The production of waveguides with a step-like index profile is discussed in the following chapter.

4.8 References

[1] R.V. Ramaswamy and R. Srivastava. Ion-Exchanged Glass Waveguides: A Review. *Journal of Lightwave Technology*, 6(6) : p984–1001, 1987.

[2] T. Izawa and H. Nakagome. Optical waveguide formed by electrically induced migration of ions in glass plates. *Applied Physics Letters*, 21(12) : p584–586, 1972.

[3] G. Giallorenzi, E.J. West, R. Kirk, R. Ginther and R.A. Andrews. Optical Waveguides Formed by Thermal Migration of Ions in Glass. *Applied Optics*, 12(6) : p1240–1244, 1973.

[4] G.H. Chartier, P. Jassaud, A.D. de Oliveira and O. Parriaux. Fast fabrication method for thick and highly multimode optical waveguides. *Electronics Letters*, 13 : p763–764, 1977.

[5] V. Neuman, O. Parriaux and L.M. Walpita. Double-alkali effect: Influence of index profile of ion-exchanged waveguides. *Electronics Letters*, 15 : p704–705, 1979.

[6] G.H. Chartier, P. Jassaud, A.D. de Oliveira and O. Parriaux. Optical waveguides fabricated by electric-field controlled ion exchange in glass. *Electronics Letters*, 14(5) : p132–134, 1978.

[7] S.S. Geveorgyan. Single-step buried waveguides in glass by field-assisted copper ion-exchange. *Electronics Letters*, 26(1) : p38–39, 1990.

[8] C.B.E. Gawith, T.Bhutta, D.P. Shepherd, P. Hua, J. Wang, G.W. Ross and P.G.R. Smith. Buried laser waveguides in neodymium-doped BK-7 by K^+–Na^+ ion-exchange across a direct-bonded interface. *Applied Physics Letters*, 75(24) : p3757–3759, 1999.

[9] S.D. Fantone. Refractive-index and spectral models for gradient-index materials. *Applied Optics*, 22(3) : p432–440, 1983.

[10] A. Opilski, R. Rogozinski, M. Blahut, P. Karasinski, K. Gut and Z. Opilski. Technology of ion exchange in glass and its application in waveguide planar sensors. *Optical Engineering*, 36(6) : p1625–1638, 1997.

[11] P.G. Debenedetti and F.H. Stillinger. Super cooled liquids and the glass transition. *Nature*, 410 : p259–267, 2001.

[12] A. Brandenburg. Stress in Ion-Exchanged Glass Waveguides. *Journal of Lightwave Technology*, LT-4(10) : p1580–1593, 1986.

[13] K. Tsutsumi, H. Hirai and Y. Yuba. Characteristics of swelling of sodium-potassium ion-exchanged glass waveguides. *Electronics Letters*, 22(24) : p1299–1300, 1986.

[14] J. Albert and G.L. Yip. Stress induced index change for K–Na ion exchange in glass. *Electronics Letters*, 23(14) : p737–738, 1987.

[15] N.V. Nikonorov and G.T. Petrovskii. Ion-Exchanged Glasses in Integrated Optics: The Current State of Research and Prospects (A Review). *Glass Physics and Chemistry*, 25(1) : p16–54, 1999.

[16] D.L. Veasey, D.S. Funk, P.M. Peters, N.A. Sanford, G.E. Obarski, N. Fontaine, M. Young, A.P. Peskin, W.C. Liu, S.N. Houde-Walter, J.S.

Hayden. Yb/Er-codoped and Yb-doped waveguide lasers in phosphate glass. *Journal of Non-Crystalline Solids*, 163& 264 : p369–381, 2000.

[17] P. Camy, J.E. Roman, F.W. Willems, M. Hempstead, J.C. van der Plaats, C. Prel, A. Beguin, A.M.J. Koonen, J.S. Wilkinson and C. Lerminiaux. Ion-exchanged planar lossless splitter at $1.5\mu m$. *Electronics Letters*, 32(4) : p321–323, 1996.

[18] Y. Jaouen, L. du Mouza, D. Barbier, J.M. Delavaux and P. Bruno. Eight-Wavelength Er-Yb Doped Amplifier: Combiner/Splitter Planar Integrated Module. *IEEE Photonics Technology Letters*, 11(9) : p1105–1107, 1999.

[19] S.D. Conzone, J.S. Hayden, D.S. Funk, A. Roshko and D.L. Veasey. Hybrid glass substrates for waveguide device manufacture. *Optics Letters*, 26(8) : p509–511, 2001.

[20] H.J. Lilienhof, E. Voges, D. Ritter and B. Pantschew. Field-Induced Index Profiles of Multimode Ion-Exchanged Strip Waveguides. *IEEE Journal of Quantum Electronics*, QE-18(11) : p1877–1883, 1982.

[21] C.R. Wylie. Advanced Engineering Mathematics. *McGraw-Hill*, Ch.8, New York, 1995.

[22] R.G. Walker, C.D.W. Wilkinson and J.A.H. Wilkinson. Integrated optical waveguiding structures made by silver ion-exchange in glass. 1: The propagation characteristics of stripe ion-exchanged waveguides; a theoretical and experimental investigation. *Applied Optics*, 22(12) : p1923–1928, 1983.

[23] M.N. Weiss and R. Srivastava. Determination of ion-exchanged channel waveguide profile parameters by mode-index measurements. *Applied Optics*, 34(3) : p455–458, 1995.

[24] T. Findakly. Glass waveguides by ion exchange: a review. *Optical Engineering*, 24(2) : p244–250, 1985.

[25] R.V. Ramaswamy and R. Srivastava. Recent advances in ion-exchanged optical waveguides and components. *Journal of Modern Optics*, 35(6) : p1049–1067, 1987.

[26] J.E. Gortych and D.G. Hall. Fabrication of Planar Optical Waveguides by K^+–Ion Exchange in BK7 and Pyrex Glass. *IEEE Journal of Quantum Electronics*, QE-22(6) : p892–895, 1986.

[27] A.F. Milton and W.K. Burns. Mode Coupling in Optical Waveguide Horns. *IEEE Journal of Quantum Electronics*, QE-13(10) : p828–835, 1977.

Chapter 5

Tapered Waveguides fabricated by Field Assisted Ion Exchange

5.1 Introduction

Interest in the ion exchange technique for the production of integrated optoelectronic (IOC) devices, was initiated due to the planar nature of ion exchange fabrication, combined with the relative simplicity of producing complex waveguide geometries [1]. IOC's often require the coupling of channel waveguides to optical fibres, for applications such as data transmission. The insertion loss, which is a measure of the loss caused by coupling radiation from a waveguide to an optical fibre, is increased with waveguides fabricated by thermal ion exchange (TIE), due to the mismatch between the graded index of the waveguide and the step-index of the fibre [2]. The development of field-assisted ion exchange (FAIE) was driven by a desire to minimise this problem.

The FAIE process is almost identical to that of TIE, with the addition of an external electric field applied across the substrate. The electric field creates an extra force that drives the ion exchange, with a field of sufficient magnitude allowing the production of a refractive index profile with negligible thermal diffusion characteristics [3]. Waveguide production times can be dramatically reduced with FAIE, as the rate of waveguide production is dependent not only on the diffusion temperature, as is the case with TIE, but also on the magnitude of the applied field. The dominance

of the electric field over the thermal diffusion, combined with the flexibility of its application, allows some control over the refractive index profile [4]. Most importantly, it is relatively simple to produce a step-like index profile [5]. As discussed in section 4.6.5, the poor laser performance of a diode-pumped, TIE fabricated, tapered waveguide laser, was partially attributed to the reduced overlap of the multimode pump and single mode laser. Tapered waveguides fabricated with a step-like index profile would benefit from a greater pump and laser overlap, possibly allowing an improvement in the diode-pumped laser performance.

The following chapter describes the FAIE process and details the production and testing of FAIE tapered waveguide lasers.

5.2 Improvement of Pump and Laser Overlap with FAIE

A reason for the poor slope efficiency gained with diode-pumped TIE tapered waveguide lasers (section 4.6.5), in relation to the results gained with titanium sapphire pumping (section 4.6.1), may be a reduction in the overlap between the multi-mode pump and single mode laser. The slope efficiency of a four-level laser is linearly related to the pump and laser mode overlap factor (equation 2.64), and is therefore crucial to the laser performance. TIE produces a graded index in both the width and the depth of the waveguide, which constrains the fundamental laser mode to a higher degree than higher order diode-pump modes. An improvement in the overlap factor is possible through the use of a step-index waveguide, as will be shown in this section.

The following analysis is limited to the overlap of the pump and laser modes within the depth of the broad section of the tapered waveguide, for the following reasons:

1. The tapered waveguide lasers have been designed so that the majority of the pump power is absorbed within the broad section of the taper, therefore it is only necessary to analyse the effect of the pump

and laser overlap within this region.

2. The flattening of the index profile across the width of the broad section, as discussed in section 3.5.4, indicates that the reduction in overlap is occurring in the depth of the waveguide.

5.2.1 Pump and Laser Overlap

The reduction in the pump and laser mode overlap of a graded index waveguide, relative to one with a step-index, can be highlighted through the use of WKB analysis, as described in section 2.3.1. WKB analysis allows calculation of the supported modes at the pump and laser wavelengths, and the effective core boundaries of these modes. The effective core boundaries for a mode within a graded index waveguide, are denoted at the points X_a and X_b [6]. Fabrication methods such as TIE produce a maximum index at the surface of the waveguide, so the first effective core boundary is situated at this depth (i.e. $X_a = 0$) [6]. The boundary X_b is different for each mode of the waveguide, with higher modes producing successively greater values of X_b. It is possible to gain an indication of the pump and laser overlap by studying the effective core boundary.

WKB analysis was completed for a $10\mu m$ deep TIE waveguide, which models the behaviour of the waveguides that underwent diode-pumping. The one-dimensional refractive index profile of a K^+–Na^+ TIE waveguide in BK7 glass [7], as detailed in section 4.3.1, was used during this analysis. The waveguide was found to support two modes at the pump wavelength $\lambda_P = 808nm$, and one mode at the laser wavelength $\lambda_L = 1.054\mu m$. The resulting effective core boundaries for the pump and laser mode are listed in table 5.1.

The results of the WKB analysis show that the fundamental laser mode is greater in size than the fundamental pump mode, allowing full extraction of the power in this pump mode. However, the first higher order pump mode is $\approx 50\%$ larger than the fundamental laser mode. The effect of this mismatch can not be calculated, as the power within each pump mode is not known. However, the method does indicate that the overlap will be

Mode no.	Wavelength μm	X_b μm
0	1.054	5.04
0	0.808	4.16
1	0.808	7.92

Table 5.1: Effective core boundaries of a TIE waveguide

reduced in relation to a step index waveguide, in which all three of the calculated modes would have equal sized core boundaries.

Further evidence for the reduced pump and laser overlap with a graded index waveguide was calculated using commercial 2D mode solving software based on the effective index method, which allows the mode profiles of a waveguide structure to be plotted.

A $175\mu m$ wide, $10\mu m$ deep broad channel waveguide was modelled, with the refractive index of the core region described by equation 3.16. A step index waveguide of identical physical size was also modelled, with the core refractive index chosen to allow the waveguide to support an identical number of modes as the graded index waveguide. The mode intensity profiles calculated at the pump and laser wavelengths are shown in figure 5.1 for the graded index waveguide, and in figure 5.2 for the step index waveguide. Figures 5.3 and 5.4 show the overlap of the pump and laser modes at the midpoint of the waveguide, for a graded index and step-index waveguide respectively.

Figure 5.1 confirms the results of WKB analysis, and shows that the pump 00 mode within a TIE waveguide is smaller than the laser 00 mode, which should allow full extraction of the power in this mode. However, the majority of power within the second mode is poorly matched with the 00 mode of the laser, leading to a reduced power extraction from this pump mode. The poor overlap of these modes is shown more clearly in figure 5.3.

The improvement in the overlap gained from a step-index profile can be seen in figure 5.2. The 00 mode of the pump and laser are well matched,

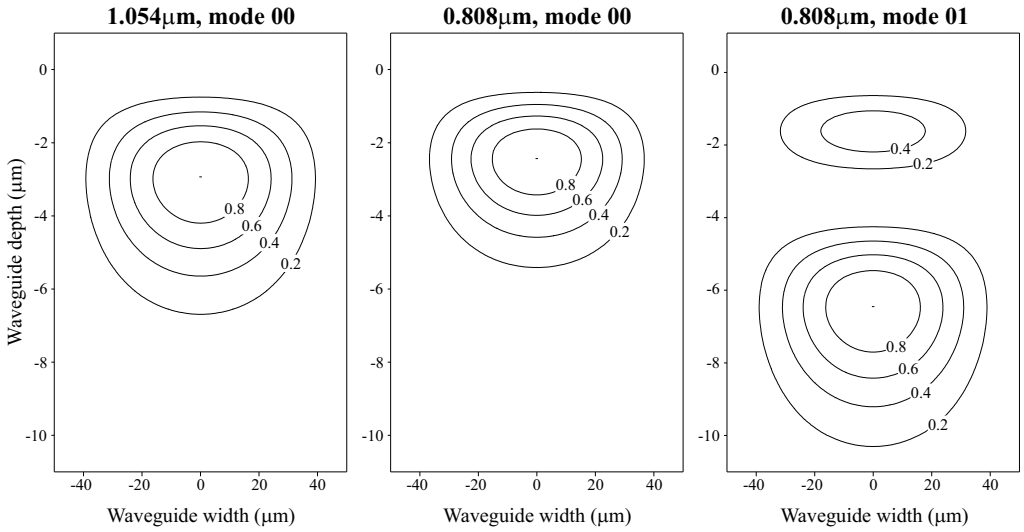

Figure 5.1: Intensity of pump and laser modes in a TIE waveguide, calculated by the effective index method

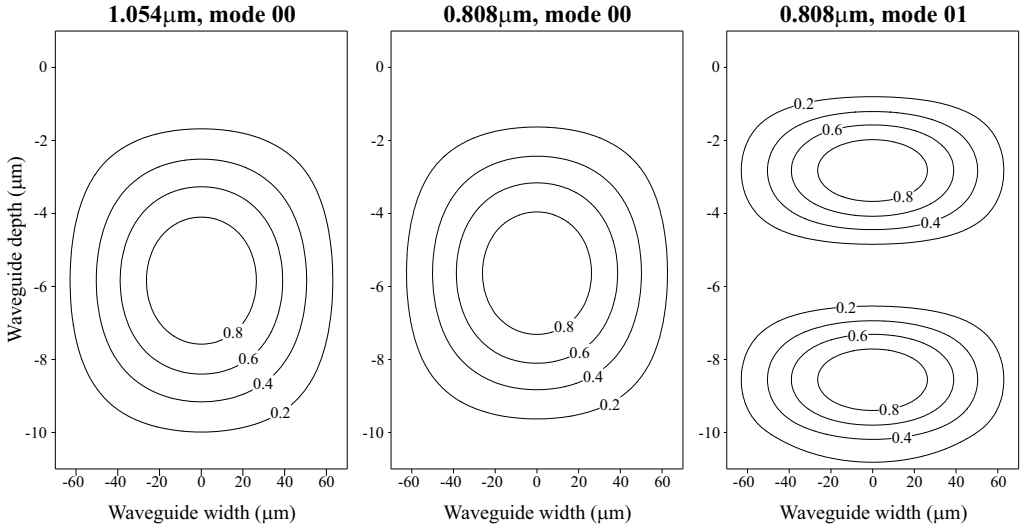

Figure 5.2: Intensity of the pump and laser modes in a step-index waveguide, calculated by the effective index method

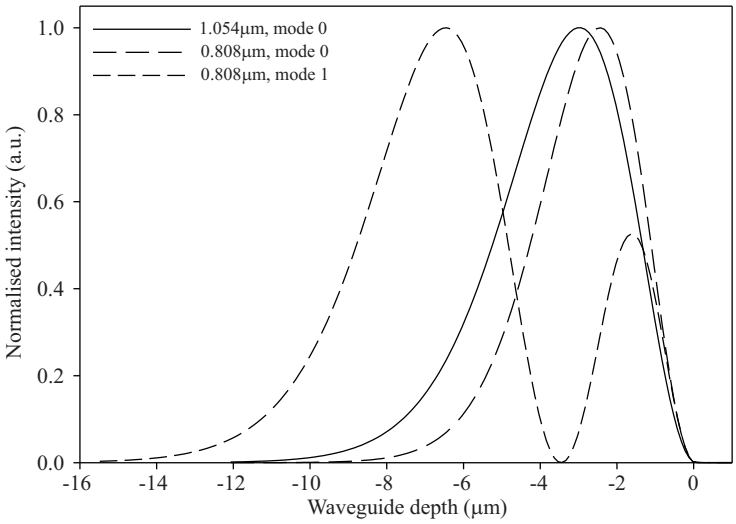

Figure 5.3: Overlap of the pump and laser modes at the centre of a graded index waveguide

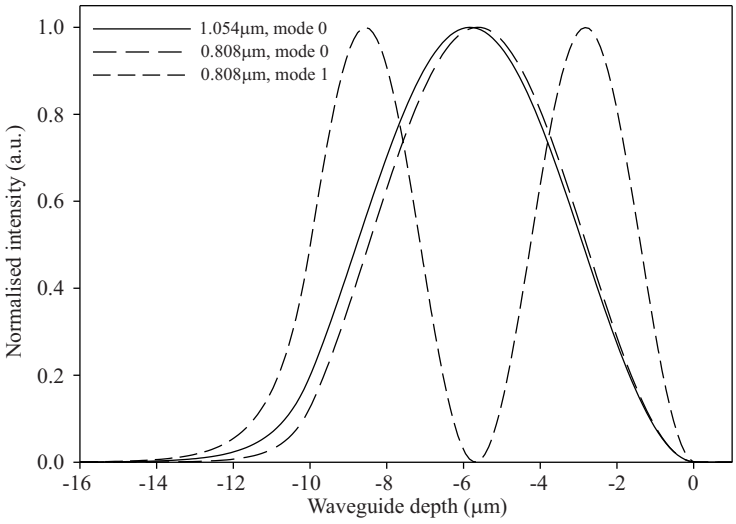

Figure 5.4: Overlap of the pump and laser modes at the centre of a step-index waveguide

allowing full extraction of the power in this mode. The overlap of the 00 mode laser and 01 mode pump is shown in figure 5.4. Although the pump mode is larger than the laser mode, leading to some reduction in power extraction, the overlap of these two modes is greater than that gained with a graded index profile.

The following sections detail the production of tapered waveguides, fabricated with a step-index profile by FAIE, in an attempt to gain access to the improved pump and laser mode overlap made possible by this fabrication technique.

5.3 FAIE Diffusion Theory

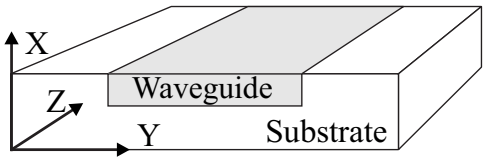

Figure 5.5: Coordinates used in diffusion equations

The theory which describes the FAIE process is very closely linked with TIE theory, and is derived from the same non-linear diffusion equation:

$$\frac{\partial c}{\partial t} + \frac{1}{1-(1-M)\,c}\mu_A \underset{\sim}{E} \cdot \nabla c = \frac{D_A}{1-(1-M)\,c}\nabla^2 c \tag{5.1}$$

Where the coordinate system is shown in figure 5.5, t is time, $c = c(x,y,z,t) = c_A/c_B^0$ is the normalised concentration of diffusant ions, c_A is the concentration of diffusant ions, c_B^0 is the concentration of exchanger ions present in the glass before ion exchange, $M = \mu_A/\mu_B$ is the ratio of the mobilities of the diffusant and exchanger ions and D_A is the diffusion coefficient of the diffusant ions. The electric field E is made up of contributions from space-charge effects and the applied field.

Assumptions of equal mobility and boundary conditions, as used in section 4.3.1, allows the one-dimensional linear diffusion equation to be solved through Laplace transform techniques [8], producing:

$$\frac{c}{c_s} = \frac{1}{2}\left[erfc\left(\frac{x-\mu_A Et}{2\sqrt{D_A t}}\right) + \exp\left(\frac{\mu_A Ex}{D_A}\right)\cdot erfc\left(\frac{x+\mu_A Et}{2\sqrt{D_A t}}\right)\right] \quad (5.2)$$

Where erfc is the complementary error function and c_s is the normalised concentration of diffusant ions at the surface of the waveguide.

It is at this point that TIE and FAIE theory diverge. The profile depth for TIE waveguides is defined at $x = W_0 = 2\sqrt{D_A t}$, as defined by equation 4.9. This definition of depth is determined by assuming that the value of E is negligible, and therefore occurs when $c/c_s = \text{erfc}(1)$. During FAIE the value for E is no longer negligible and another definition of profile depth must be determined.

With sufficiently large values of E, the second term of equation 5.2 becomes negligible, as the erfc term approaches zero for increasing x at a faster rate than the growth of the exponential term, allowing the following approximation [3]:

$$\frac{c}{c_s} \approx \frac{1}{2}\left[erfc\left(\frac{x-\mu_A Et}{2\sqrt{D_A t}}\right)\right] \quad (5.3)$$

The contribution to the overall waveguide depth is now separated into two parts: that resulting from thermal diffusion $W_0 = 2\sqrt{D_A t}$ and that resulting from the ions being driven by the electric field W_F, where:

$$W_F = \mu_A Et \quad (5.4)$$

Ramaswamy and Najafi [3] found that the approximation described in equation 5.3, is reasonable when the profile depth due to the electric field is $\geqslant 2.5\times$ the profile depth due to the thermal diffusion:

$$\mu_A Et \geqslant 5\sqrt{D_A t} \quad (5.5)$$

The Einstein relation is utilised to state μ_A in terms of D_A [9]:

$$\mu_A = \frac{D_A \phi_A e}{kT} \tag{5.6}$$

Where ϕ_A is the valence of the diffusant ion, e is the electronic charge, k is the Boltzmann constant and T is the absolute temperature.

Equation 5.5 can now be rearranged for E in terms of D_A only:

$$E_R = \frac{5kT}{\phi_A e \sqrt{D_A t}} \tag{5.7}$$

Where E_R is the electric field strength required to produce waveguides with negligible thermal diffusion characteristics.

Use of $D_A = 1.6\mu m^2 hr^{-1}$ at $T = 673K$ for the potassium ion in BK7 [10], with an average value of $t = 1hr$, used during the following FAIE fabrication, produces $E_R = 2.3 \times 10^5 Vm^{-1}$. During the following FAIE experiments a minimum voltage of $2kV$ was applied across the $3mm$ thick samples, resulting in an applied electric field of $E = 6.7 \times 10^5 Vm^{-1}$. It should be noted that the FAIE experiments were completed at a temperature of $T = 508K$. However, values for the diffusion coefficient were not available at these temperatures. The diffusion coefficient and temperature are related by the Arrhenius equation [11]:

$$D_A = D_0 e^{\left(-\frac{E_A}{kT}\right)} \tag{5.8}$$

Where D_0 is the diffusion constant, E_A is the activation energy for the ion exchange and k is Boltzmann's constant.

As k is a constant and D_0 and E_A are constants of the potassium ion exchange process in BK7. It can be seen that the diffusion coefficient decreases exponentially with decreasing temperature. A reduction in temperature causes the numerator of equation 5.7 to decrease linearly, whereas the denominator decreases by the square root of an exponential reduction, and therefore increases the required field strength E_R. Without knowledge of the diffusion constant and activation energy for the K^+–Na^+ TIE process, it is not possible to predict the actual E_R value required for the

production of a step-like index profile at $508K$. However, previous work with potassium–sodium FAIE [12] has produced waveguides with a step-like index profile using the FAIE conditions stated in the previous paragraph. Analysis of the index profiles of FAIE waveguides, detailed in section 5.6.1, validated this assumption.

If the electric field applied during the FAIE experiments exceeds the value required to overcome thermal diffusion characteristics, it may be possible to neglect all diffusion characteristics. Under this assumption the one-dimensional diffusion equation can be stated [5]:

$$\frac{c}{c_s} = \delta\left(\mu_A E t - x\right) \tag{5.9}$$

Where δ is the unit step function. The unit step function is defined as follows:

$$\delta(\theta) = \begin{cases} 0 \text{ for } \theta < 0 \\ 1 \text{ for } \theta \geqslant 0 \end{cases} \tag{5.10}$$

Where θ is the argument of the unit step functions, and is used only to describe the functions operation.

This definition states that the resulting concentration profile will be maintained at the surface concentration c_s for all depths $\leqslant \mu_A E t$, and at the point $x = \mu_A E t$ the concentration drops to zero instantaneously.

5.4 Practicalities of the FAIE Process

Due to the similarity between TIE and FAIE, identical considerations are required concerning the choice of the glass and diffusant ion. This process was simplified, in relation to the work of this thesis, as a direct comparison was required between tapered waveguides produced by TIE and FAIE, limiting the ion exchange to K^+–Na^+ FAIE in BK7 glass.

The apparatus required for FAIE has not been standardised to the same

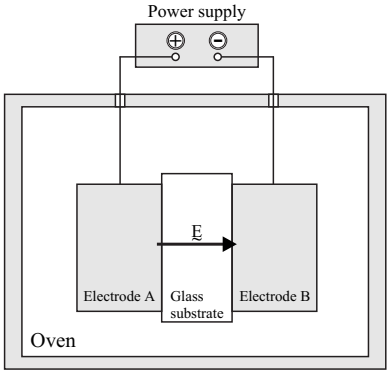

Figure 5.6: Simplified schematic of the FAIE fabrication process

extent as that used for TIE. A basic schematic of FAIE apparatus is shown in figure 5.6. Electrode A is often a molten nitrate salt [1,2], but can also be a metal film for the ion exchange of stable metals such as silver [13] and copper [14]. During this thesis a source of potassium ions was required, limiting the material to potassium nitrate.

A power supply creates a potential difference across the glass substrate, generating an electric field that drives diffusant ions from electrode A into the glass. Glass ions are driven out of the substrate and into electrode B, which is often a molten salt, as glass ions such as sodium can cause degradation of metal electrodes [15]. However, the use of a molten salt for both electrodes can cause difficulties with short circuiting, as it is very difficult to isolate two molten salts under a high electric field. The use of a metal film for electrode B can reduce these complications, with gold often chosen for its low reactivity [5, 15]. It has been shown during this work that an aluminium electrode of sufficient thickness ($\approx 800nm$) can withstand the ionic degradation, and in relation to gold, offers the benefits of low cost and ease of evaporation.

The optimum temperature for FAIE suffers from contradictory requirements. High temperatures increase the diffusant ion mobility (equation 5.6), and as the profile depth $W_F = \mu_A E t$, allows waveguides to be produced over short times with relatively weak electric fields. However, higher temperatures increase the unwanted thermal diffusion and limit the materials that can be used for building and sealing the FAIE apparatus. Lower

temperatures minimise thermal diffusion, but necessitate the use of a high electric field strength to produce waveguides in a reasonable time, requiring high voltages, and therefore more stringent safety measures.

During the following work the relatively low temperature of $235℃$ was chosen to produce a step-like index profile by minimising thermal diffusion. Sanford et.al. [12], produced FAIE waveguides that supported a single-mode at $\lambda = 1.05\mu m$, at this temperature, with an electric field strength of $E = 2.7kVmm^{-1}$. This work was used as the starting point of the following experiments. Pure potassium nitrate melts at $333℃$, and would therefore be solid at this temperature. To overcome this problem a $61{:}39$ eutectic mix of potassium and calcium nitrate, which melted at $200℃$, was used as the diffusant ion source.

The reproducibility of the FAIE process is known to be lower than that of the TIE process [16]. The majority of FAIE waveguides are produced using the voltage applied across the glass sample, and therefore the electric field, as the control parameter. Klein et.al. [17] proposed a method to improve reproducibility by using the current, and therefore the accumulated charge, as the control parameter. If the assumption is made that the K^+ and Na^+ ions are the only mobile ions within the glass, and that the ion exchange operates on a one-for-one exchange basis, then the total charge transferred across the glass is directly proportional to the number of exchanged ions, and therefore the waveguide size. Although little previous work has been completed with charge-controlled FAIE, it was assumed that this may overcome reproducibility problems and was used during the following work.

FAIE apparatus requires a somewhat more complex design than that shown in figure 5.6. The glass substrate and electrodes are held within a 'FAIE cell', as detailed in figure 5.7. The BK7 sample is placed into one half-cell (figure 5.7a), and a seal is created by bolting the second half of the cell on top of the first (figure 5.7b). A combination of a silicone rubber O-ring and PTFE tape was found to be the optimum sealant. After sealing the cell, the eutectic mixture of nitrate salts is added into the salt chamber in powder form, at room temperature. Electrical connections are made di-

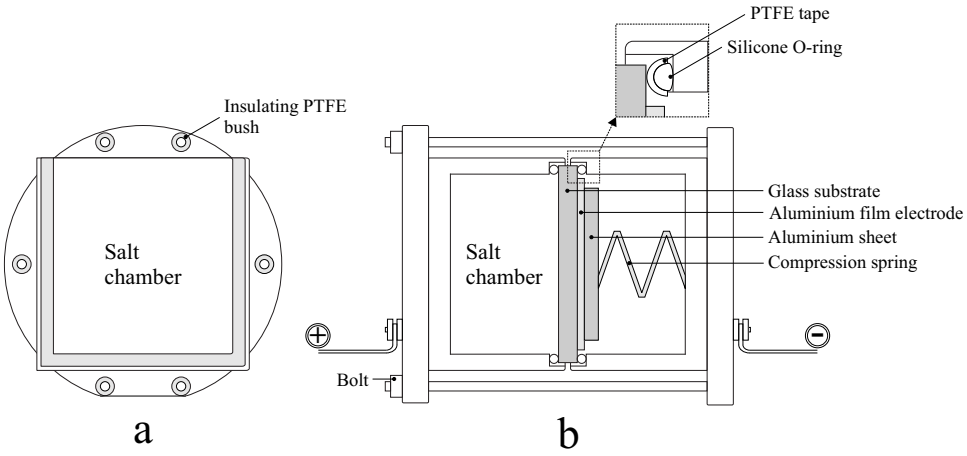

Figure 5.7: FAIE fabrication apparatus used during this thesis: a/ side-view of one half-cell, b/ plan-view of both half-cells and glass substrate

rectly to each half-cell, allowing a uniform field to be created over the glass sample. The salt electrode is connected to the power supply through the conductivity of the cell, and the aluminium film electrode is connected to the power supply through the cell conductivity, a conducting compression spring and a $2mm$ thick aluminium sheet.

5.5 Fabrication of FAIE Waveguides

Samples of undoped and 1.5wt% Nd^{3+}-doped BK7, measuring $45 \times 45 \times 3mm$ were polished to optical quality on one large face. The polished large face will be called the 'waveguide-face', and the face opposite to this will be called the 'electrode-face'. The samples were cleaned in preparation for FAIE, using the standard procedure outlined in section 4.4.1.

$175\mu m$ wide broad channels, from mask group 1 (appendix B, table B.1), and tapers from mask group 2 (appendix B, table B.2), were delineated on the waveguide-face using an identical procedure to that detailed in section 4.4.3. Planar waveguides, which did not require photolithography, were also fabricated. An electrode was created on the unpolished electrode-face of the sample by coating the face with an $\approx 800nm$ thick layer of aluminium using a thermal evaporator, as detailed in section 4.4.2.

Sample no.	Feature	FAIE duration min
F1	Planar	70
F2	Planar	80
F3	Planar	90
F4	Planar	100
F5	3×175μm wide broad channels and 2×2.5μm wide channels	70
F6	3×175μm wide broad channels and 2×2.5μm wide channels	90
F7	3×175μm wide broad channels and 2×2.5μm wide channels	110
F8	1× Group 1 linear tapers	90
F9	1× Group 1 linear tapers	110

Table 5.2: Fabrication parameters used during the fabrication of the FAIE waveguides

The prepared substrate was loaded into the FAIE cell, and the salt chamber was filled with a $61{:}39$ mix of potassium nitrate and calcium nitrate. A glass slide was placed over the top of the salt chamber to minimise evaporation of the salt. The loaded FAIE cell was placed into an Instron SFL ion exchange oven, with each half-cell resting on a $30 \times 20 \times 10mm$ block of PTFE, which electrically isolated the cell from the metal interior of the oven. Electrical connections were made to each half-cell, using teflon coated aluminium wire.

The oven was heated to $235^{\circ}\mathrm{C}$, and was left for $1hr$ to allow the contents to reach thermal equilibrium. After this time the FAIE was initiated by supplying a current of $380\mu A$ across the cell, from a Glassman EH-PS power supply. Constant temperature and current were maintained for times between 60–$110min$. During this time the voltage behaviour was recorded with a chart recorder. At the end of the preset time, the power supply and the oven were turned off, and the FAIE cell was cooled to room temperature over an hour.

The sample was removed from the chamber, washed in DI water to remove residual salt and dried in a $120^{\circ}\mathrm{C}$ oven. The aluminium electrode and ion exchange mask were removed, as detailed in section 4.4.4.

A $1mm$ section was cut from each end of the FAIE samples to remove edge-effects of the FAIE process, and the end-faces were polished perpendicular to the waveguide axis, in preparation for optical characterisation.

Table 5.2 summarises the fabrication conditions under which the FAIE waveguides were produced.

5.6 Direct Characterisation of FAIE by SIMS

The concentration profile of diffusant ions within the waveguide, and therefore the refractive index profile, was measured using SIMS analysis identical to that discussed in section 4.5. A direct measurement of the concentration profile would allow calculation of the refractive index profile, and confirmation of the parameters used to overcome thermal diffusion.

Due to the high cost of SIMS analysis, only two samples were analysed: samples F1 and F5, which contained a planar waveguide and $175\mu m$ wide broad channel waveguides respectively. The $2.5\mu m$ channels present on sample F5 could not be analysed, due to the lateral resolution of the SIMS. In each case the concentration of diffusant ions was measured through the depth of the waveguide. As previously discussed, SIMS analysis generates a variable named 'counts' for each analysed ion, which is directly proportional to the ion concentration. Calibration of the counts data could not be completed in the manner used for TIE waveguides, as the surface refractive index of a FAIE waveguide is dependant upon the applied field and temperature [15], and is therefore not constant. No measurement of the surface index has been completed for a waveguide produced under the conditions described in the previous section, so calibration of the counts data was not possible. However, the shape of the profile is of greatest relevance to the work completed with FAIE, which is not altered by calibrating the data. Under this rationale, it is possible to justify the assumptions made for the electric field strength and temperature required to produce a step-like index profile, without calibrating the data.

The SIMS data was prepared for analysis by removing the contribution to

the counts data made by background levels of potassium present within the BK7, followed by normalisation of the data.

Three functions were fitted to the normalised data. The unit step function (equation 5.10) was fitted to test the accuracy of this extreme case, which neglects all thermal diffusion characteristics. The modified erfc function (equation 5.3) was fitted to test whether appreciable thermal diffusion did occur during FAIE, and also allowed calculation of the diffusion coefficient. A third equation was fitted following the work of Yip et.al [2], who proposed a modified Fermi-function as an accurate description of the index profile of FAIE waveguides:

$$\frac{c}{c_s} = \left[1 - \exp\left(\frac{W_{ff}}{a}\right) + \exp\left(\frac{x - W_{ff}}{a}\right)\right]^{-1} \tag{5.11}$$

Where W_{ff} is the Fermi-function waveguide depth, and a is a constant related to the shape of the profile.

Whereas the unit step function descends from its maximum value to zero instantaneously, the modified Fermi-function reduces more gradually and in this way allows for thermal diffusion. The obvious disadvantage of the modified Fermi-function is that useful data, such as the diffusion coefficient, cannot be derived from the fit. However, testing the accuracy of this fit against the other proposed functions was believed to be of interest.

5.6.1 SIMS Fitting Results and Discussion

Figures 5.8–5.10 show the SIMS data generated for sample F2 fitted to each of the three analysed functions. The error in fit calculated for each theoretical profile is indicated through the use of the average percentage residual $\bar{r}_p$ (described in section 4.5), and is listed in table 5.3.

Within both samples the potassium concentration is maintained at an almost constant value through the depth of the waveguide, confirming that a step-like index profile has been created. This assumption is reinforced by the small difference in $\bar{r}_P$ between the modified erfc function, which

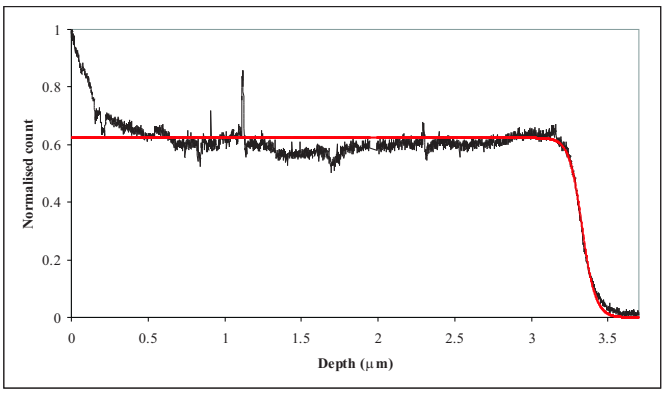

Figure 5.8: SIMS data fitted for sample F5, fitted to a modified erfc function (equation 5.3)

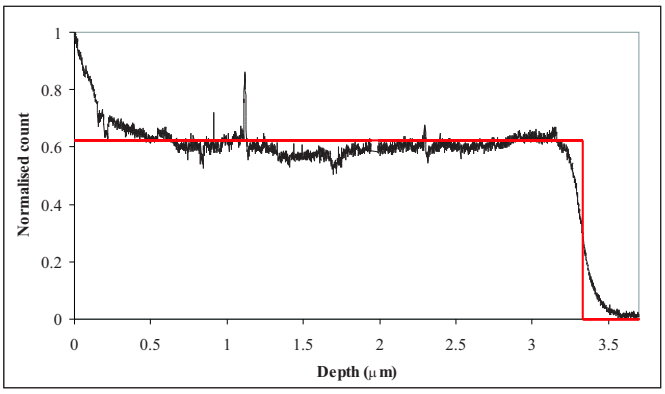

Figure 5.9: SIMS data fitted for sample F5, fitted to a unit step function (equation 5.10)

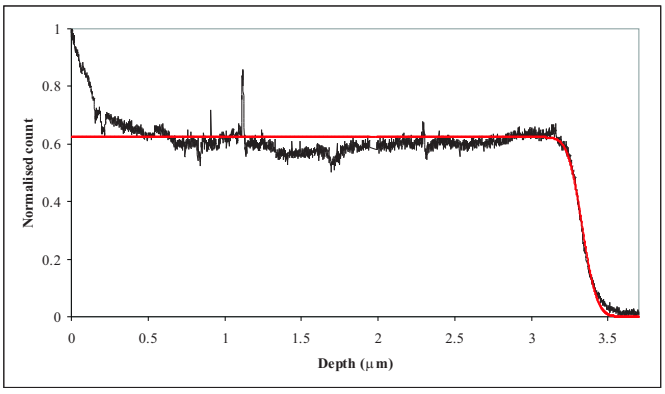

Figure 5.10: SIMS data fitted for sample F5, to a modified Fermi-function (equation 5.11)

Sample no.	Fitted function	Predicted depth μm	$\bar{r}_P$ %
F1	Modified erfc	3.2±0.5	16.9
	Unit step	3.2±0.8	23.9
	Modified Fermi	3.2±0.5	16.4
F5	Modified erfc	3.4±0.4	11.9
	Unit step	3.3±0.5	16.3
	Modified Fermi	3.3±0.4	12.6

Table 5.3: The quality of fit, calculated for samples F1 and F5, to each of the theoretical profiles

accounts for thermal diffusion, and the unit step function, which neglects it. The effect of the electric field on the ion exchange can be highlighted by comparing the FAIE SIMS results to the SIMS profiles generated for TIE (figures 4.5 and 4.6). It is obvious from this comparison that a more step-like profile has been obtained.

The modified erfc and modified Fermi-function provide a slightly more accurate description of the concentration profile. However, all three methods predict a similar value for the waveguide depth. For this reason it can be concluded that, for an applied field of the magnitude utilised during fabrication, the unit step function can be used for waveguide design.

The modified erfc fit, in conjunction with the FAIE duration, allows calculation of the diffusion coefficient for the potassium ion within BK7. Calculated values for the diffusion coefficient were $2.21\mu m^2 hr^{-1}$ for sample F1, and $2.25\mu m^2 hr^{-1}$ for sample F5, which are within the same order of magnitude as that measured by Opilski et.al. [10], but lower, as would be expected for an ion exchange completed at a lower temperature.

Samples F1 and F5 were created under identical fabrication conditions, however, the waveguide depth of F5 is greater than that of F1. FAIE through an aperture in a metal mask acts in the opposite manner to TIE: as the mask opening reduces, the depth of the waveguide increases [18]. This has important implications concerning the fabrication of tapered waveguides. During TIE it was beneficial that the wider sections of the waveguide were deeper, as this allowed a greater depth for the diode-pumped

end of the waveguide, whilst maintaining single-mode output at the channel end. FAIE tapered waveguides will be deeper in the channel end than at the broad channel end, which may cause problems with diode-pumping, producing a single-mode output, or both. The increase in waveguide depth for narrow channel openings is due to a field concentration within the opening, and can be overcome through the use of a dielectric mask material [19]. It was decided that during this early work with FAIE, that the benefits of ease of evaporation and etching gained with an aluminium mask, outweighed the problems caused through waveguide deepening. Once the FAIE process had been optimised, experiments could begin with dielectric mask materials to overcome the waveguide deepening.

5.7 Optical Characterisation of FAIE Waveguides

5.7.1 Determination of Waveguide Depth

Initial values for the temperature, current and diffusion time required to fabricate single mode (at $1.05\mu m$) FAIE waveguides were calculated from Sanford et.al. [12]. Sanford et.al calculated these values for K^+–Na^+ FAIE in soda-lime-silicate glass and, as a different glass was used during this work, the fabrication parameters would require some optimisation. Optimum fabrication conditions for FAIE in BK7 were found by producing waveguides by varying the FAIE duration, under identical conditions of temperature and current.

Planar waveguides were fabricated, and the number of modes supported at $633nm$ and $1.06\mu m$ were determined using m-line prism coupling techniques. The optimum FAIE duration which produced a single-mode waveguide at $1.06\mu m$, was applied to the fabrication of $175\mu m$ wide broad channels, and the optimisation of the FAIE duration was completed again. Tapered waveguides fabricated by FAIE were produced using the optimum fabrication values found for the $175\mu m$ wide broad channels.

5.7.2 The Prism Coupler

Figure 5.11 details the equipment required for prism coupling. A prism, of higher refractive index than the waveguide, is clamped onto the top surface of the waveguide. A linearly polarised laser is directed to be incident on the front face of the prism, with the path inside the prism depicted in figure 5.12. The prism and waveguide are mounted on a rotational stage, which allows the angle α to be varied. The ray is refracted inside the prism towards its base, and is incident at an angle θ_{pr}, which can be related to α through Snell's law and the geometry of the prism:

$$\theta_{pr} = \gamma + \sin^{-1}\left(\frac{n_1}{n_{pr}}\sin\alpha\right) \tag{5.12}$$

Where γ is the prism angle, n_1 is the index of the surrounding air and n_{pr} is the prism index.

Each mode p within the waveguide is related to a characteristic propagation angle θ_m as shown in figure 5.12. The effective index of the mode is related to the propagation angle and the index of the waveguide, which can be related to the prism index and the angle of incidence at the prism base through Snell's law:

$$(n_{eff})_p = n_2 \sin\theta_m = n_{pr}\sin\theta_p r \tag{5.13}$$

Where $(n_{eff})_p$ is the effective index of mode p.

It can be seen from equation 5.13 that by varying α the angle θ_{pr} can be varied to match each of the propagation angles within the waveguide. At this point the evanescent field that extends into the waveguide can couple power from the prism into the appropriate waveguide mode. It is possible to record the angle α at which this coupling occurs, as a bright line appears in the focussed output from the waveguide. It is this m-line that gives the prism coupling technique its name.

Rearranging the guidance condition for a asymmetric three-layer waveguide (equation 2.25) allows the effective index to be stated in terms of the

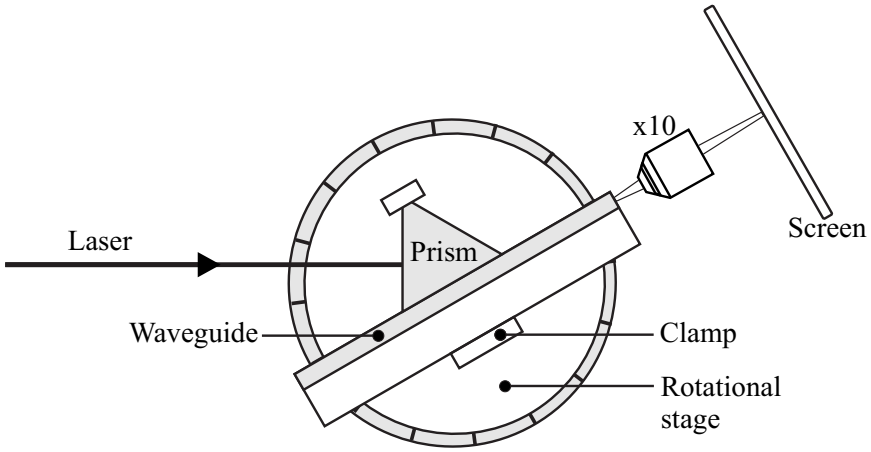

Figure 5.11: Prism coupling apparatus

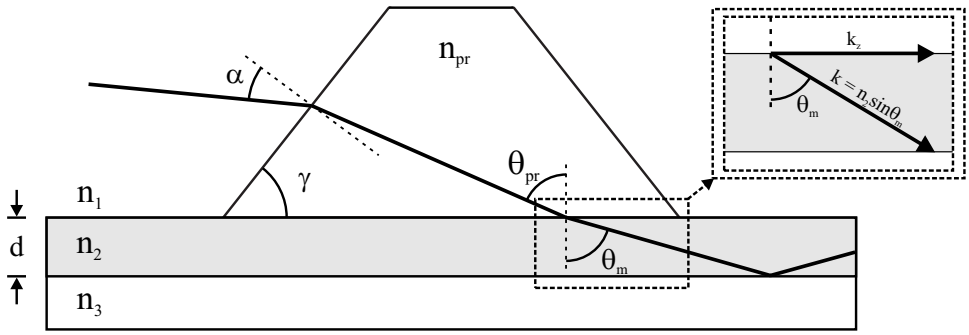

Figure 5.12: Ray path through a prism

waveguide index n_2 and depth d [20]:

$$k_0 d \left[n_2^2 - (n_{eff})_p^2 \right]^{\frac{1}{2}} = \psi_p \tag{5.14}$$

Where:

$$\psi_p = p\pi + \varphi_1 + \varphi_3 \tag{5.15}$$

and $k_0 = \frac{2\pi}{\lambda_0}$, λ_0 is the free-space wavelength, and φ_1, φ_3 are the phase changes due to reflection at the waveguide boundaries, as defined in section 2.2.2, which can be rearranged to account for the effective index [20]:

$$\begin{aligned} \varphi_1 &= \tan^{-1} \left[\left(\frac{n_2}{n_1} \right)^{2\rho} \left(\frac{(n_{eff})_p^2 - n_1^2}{n_2^2 - (n_{eff})_p^2} \right) \right] \\ \varphi_3 &= \tan^{-1} \left[\left(\frac{n_2}{n_3} \right)^{2\rho} \left(\frac{(n_{eff})_p^2 - n_3^2}{n_2^2 - (n_{eff})_p^2} \right) \right] \end{aligned} \tag{5.16}$$

Where n_3 is the substrate index and $\rho = 0$ for TE modes and $\rho = 1$ for TM modes.

If the angle α is known for at least two modes, the waveguide index and depth can be calculated using an iterative technique [21]. As the waveguides were designed to be single-mode at $1.05\mu m$, the prism coupling was completed using a helium-neon laser at $\lambda = 632.8nm$, which would allow approximately two modes to be supported. The following method assumes the waveguide to have a step-index profile, which has been shown to be a valid assumption for the FAIE waveguides (section 5.6.1). The calculated effective indices for each mode are entered into equation 5.14, and the two resulting equations are divided to eliminate the constants k_0 and d. Rearranging this equation for n_2 produces [21]:

$$n_2^2 = \frac{(n_{eff})_0^2 \psi_1^2 - (n_{eff})_1^2 \psi_0^2}{\psi_1^2 - \psi_0^2} \tag{5.17}$$

Equation 5.17 can not be calculated explicitly as the values ψ_0 and ψ_1 are unknown. To overcome this problem an initial guess value is used for

the waveguide index n_2, which can then be accurately calculated through an iterative algorithm performed on a computer. Entering the calculated value of n_2 into equation 5.14 with the appropriate effective index, allows calculation of the waveguide depth d.

5.7.2.1 Prism Coupling Results and Discussion

Table 5.4 lists the values of n_2, d and $\Delta n = n_2 - n_3$ calculated by prism coupling for each FAIE waveguide. The calculation could not be completed for samples F5 and F6 as only one mode was supported at $632.8nm$.

The waveguide depth of $3.8\mu m$ calculated for sample F1, can be compared to the depth calculated by fitting a unit step function to the SIMS data generated for this sample. A difference in the predicted waveguide depth of $0.6\mu m$ is apparent between the two methods, but can be explained as the index profile is not a definite step-function, as is assumed during prism coupling. An error is also present during the SIMS analysis, as the data recorded within the first $\approx 0.1\mu m$ of depth is partially due to a warm-up of the ion beam, and is not in fact an analysis of the sample.

Sample no.	Feature	FAIE duration min	Δn	d μm
F1	Planar	70	0.016±0.002	3.8±0.1
F2	Planar	80	0.016±0.002	3.8±0.1
F3	Planar	90	0.016±0.002	4.4±0.1
F4	Planar	100	0.019±0.002	4.6±0.1
F7	3×175μm broad channels and 2×2.5μm channels	110	0.018±0.002 0.019±0.002	5.7±0.1 6.5±0.1

Table 5.4: FAIE prism coupling results

Figure 5.13 shows the relationship between the planar waveguide depth and the FAIE duration. The data accurately follows a linear relationship, which can be measured using the R^2 parameter that is defined:

$$R^2 = 1 - \frac{SSE}{SSM} \tag{5.18}$$

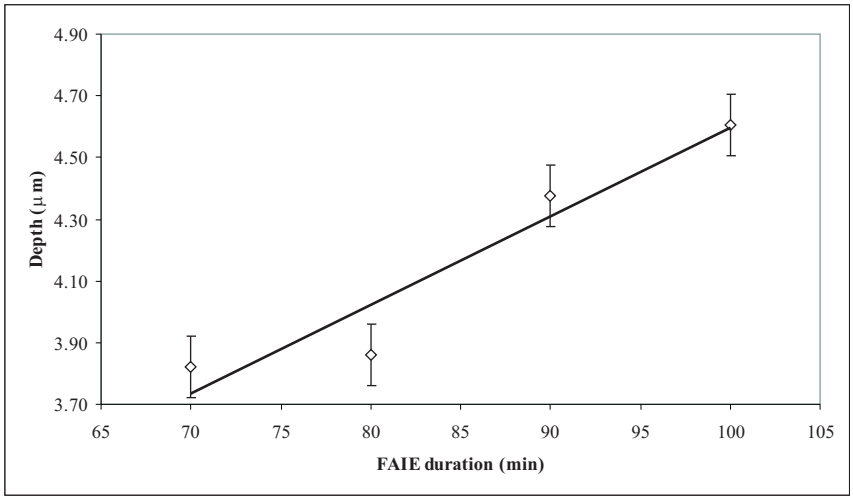

Figure 5.13: Relationship between FAIE waveguide depth and duration

Where SSE is the sum of the squared residuals, SSM is the sum of the squares about the mean value, and an $R^2 = 1$ indicates a perfect fit.

An R^2 of 0.92 was calculated for the linear fit to the data in figure 5.13, leading to the conclusion that the relationship between the waveguide depth and FAIE duration is behaving in a linear fashion, as predicted by equation 5.4.

Confirmation that FAIE produces deeper waveguides for narrower mask openings is evident from sample F7. $2.5\mu m$ channels exhibited an $\approx 10\%$ increase in waveguide depth compared to the $175\mu m$ broad channels. This has implications for the efficient operation of a tapered waveguide laser, as previously discussed. These results indicate that later work with FAIE should be completed with a dielectric mask to investigate whether this effect can be negated. More thorough investigation of this phenomenon could not be completed, as samples F5 and F6 supported only one mode at $632.8nm$.

There is no available data to confirm the value of Δn calculated for these waveguides. However, some confidence can be gained from general statements of the behaviour of Δn for the FAIE process. FAIE should produce larger values of Δn than TIE [16], as has been calculated. The magnitude of Δn depends upon the applied field and the temperature of the process,

so similar values would be expected for the FAIE waveguides, as each was fabricated under identical conditions of temperature and similar values of electric field. The similar values of Δn calculated for each waveguide supports this assumption, with an indication of an increase in Δn calculated for the broad channel waveguides being attributed to the increase in the applied field due to the concentrating effect of the metal mask [18].

5.7.3 Laser Results

Tapered waveguide lasers were fabricated for FAIE durations of 90 and $110min$, under identical conditions of current and temperature used during the production of broad channel waveguides. The operation of the lasers was tested using a titanium sapphire pump laser and identical experimental set up, as used for the TIE tapered waveguide lasers (section 4.6.1).

A cavity was created using two highly reflecting (HR) mirrors at the laser wavelength. An incident threshold power of $75mW$ was measured for the channel waveguide, an increase of $15\times$ that measured for a TIE fabricated channel, indicating that the FAIE channel suffers from a very high loss. The output spatial profile of the channel waveguide laser was recorded with a CCD camera (figure 5.14), and exhibited a double-mode in the width of the waveguide, which may be due to the higher refractive index change recorded for the FAIE waveguides. The $300\mu m$ wide taper was the only taper to exhibit lasing. The spatial output of this waveguide exhibited a highly multimode output in the width of the taper.

The multimode output cannot be attributed to the taper shape, as this has been shown to produce adiabatic operation during the investigation of TIE tapered waveguide lasers. It has been shown that channel waveguides fabricated by FAIE can suffer from 'lobes' in the index profile [5] (see figure 5.15). The lobes are areas of greater waveguide depth at the edges of the index profile, caused by an inhomogeneous applied field, due to the ion exchange occurring through a conducting mask. More rigorous SIMS analysis may allow the presence of these lobes to be identified. Alterna-

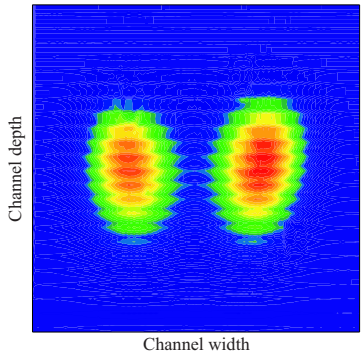

Figure 5.14: Output from the FAIE channel waveguide

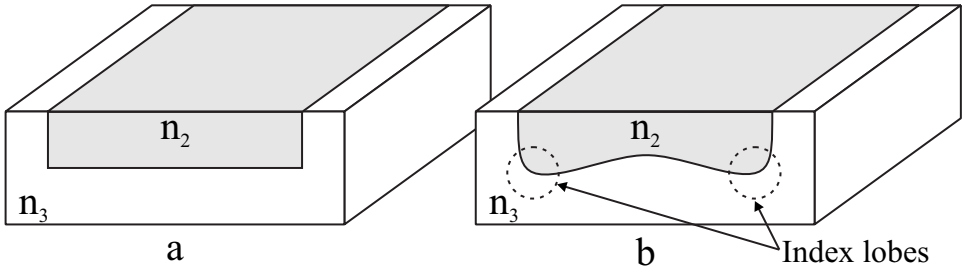

Figure 5.15: Index lobes resulting from FAIE fabrication: a/ desired step-index profile, b/ index profile showing lobes

tively, the use of a dielectric masking material would allow a homogeneous field to be applied across the sample [5] eliminating the formation of index lobes. A more tenuous explanation of the multimode output may be an inhomogeneous ion exchange. It may be possible that the ion exchange is being blocked by bubble formation, due to boiling of the ion exchange salt, or perhaps by contamination of the salt. However, both of these explanations are supposition, as no time was available to determine the cause of the multimode output. It is therefore necessary that further work is completed to optimise the FAIE process, and improve the laser performance of the resulting waveguides.

5.8 Summary

The fabrication parameters required to produce a FAIE waveguide with a step-like index profile have been discussed. The index profile of the re-

sulting waveguides was measured by SIMS analysis and attained a good match to the theoretically expected results. The effect of the applied field was highlighted by comparison to SIMS measured index profiles of TIE waveguides. The waveguide depth measured by SIMS analysis was verified by prism coupling techniques, and a reasonable agreement between these methods was determined. The assumptions made to allow fabrication of a step-index waveguide have therefore been verified.

Unfortunately, poor laser performance was gained from both a FAIE channel and tapered waveguide. A threshold power of $75mW$ was measured for the channel waveguide laser, a value $\approx 15\times$ greater than that measured for an identical waveguide fabricated by TIE. The high threshold of the channel waveguide laser indicates that the poor performance of the tapered waveguide is not attributable to the taper, and must be related to the fabrication process. The FAIE process requires some optimisation, and would benefit from more detailed SIMS analysis. There are many possibilities for improving the FAIE process, with emphasis placed on determining the presence of index lobes which, if present, may be reduced through the use of a dielectric mask material.

5.9 References

[1] T. Izawa and H. Nakagome. Optical waveguide formed by electrically induced migration of ions in glass plates. *Applied Physics Letters*, 21(12) : p584–586, 1972.

[2] G.L. Yip, P.C. Noutsios and K. Kishoika. Characteristics of optical waveguides made by electric-field-assisted K^+ -ion exchange. *Optics Letters*, 15(14) : p789–791, 1990.

[3] R.V. Ramaswamy and S.I. Najafi. Planar, Buried, Ion-Exchanged Glass Waveguides: Diffusion Characteristics. *IEEE Journal of Quantum Electronics*, QE-22(6) : p883–891, 1986.

[4] S.N. Houde-Walter and D.T. Moore. Gradient-index profile control by field-assisted ion exchange in glass. *Applied Optics*, 24(24) : p4326–4333, 1985.

[5] H.J. Lilienhof, E. Voges, D. Ritter and B. Pantschew. Field-Induced Profiles of Multimode Ion-Exchanged Strip Waveguides. *IEEE Journal of Quantum Electronics*, QE-18(11) : p1877–1883, 1982.

[6] G.B. Hocker and W.K. Burns. Modes in Diffused Optical Waveguides of Arbitrary Index Profile. *IEEE Journal of Quantum Electronics*, QE-11(6) : p270–276, 1974.

[7] M.N. Weiss and R. Srivastava. Determination of ion-exchanged channel waveguide profile parameters by mode-index measurements. *Applied Optics*, 34(3) : p455–458, 1995.

[8] C.R. Wylie. Advanced Engineering Mathematics. *McGraw-Hill*, Ch.8, New York, 1995.

[9] R.V. Ramaswamy and R. Srivastava. Ion-Exchanged Glass Waveguides: A Review. *Journal of Lightwave Technology*, 6(6) : p984–1001, 1987.

[10] A. Opilski, R. Rogozinski, M. Blahut, P. Karasinski, K. Gut and Z. Opilski. Technology of ion exchange in glass and its application in waveguide planar sensors. *Optical Engineering*, 36(6) : p1625–1638, 1997.

[11] P.G. Shewmon. Diffusion in Solids. *McGraw-Hill*, New York, 1963.

[12] N.A. Sanford, K.J. Malone and D.R. Larson. Integrated-optic laser fabricated by field-assisted ion exchange in neodymium-doped soda-lime-silicate glass. *Optics Letters*, 15(7) : p366–368, 1990.

[13] B.G. Pantchev. One-step field-assisted ion exchange for fabrication of buried multimode optical strip waveguides. *Electronics Letters*, 23(22) : p1188–1190, 1987.

[14] S.S. Gevorgyan. Single-step buried waveguides in glass by field-assisted copper ion-exchange. *Electronics Letters*, 26(1) : p38–39, 1990.

[15] S.I. Najafi, P.G. Suchoski and R.V. Ramaswamy. Silver Film-Diffused Glass Waveguides: Diffusion Process and Optical Properties. *IEEE Journal of Quantum Electronics*, QE-22(12) : p2213–2218, 1986.

[16] G. Sorbello, S. Taccheo, M. Marano, M. Marangoni, R. Osellame, R. Ramponi and P. Laporta. Comparitive study of Ag-Na thermal and field-assisted ion exchange in Er-doped phosphate glass. *Optical Materials*, 17 : p425–435, 2001.

[17] R. Klein, D. Jestel, H.J. Lilienhof and E. Voges. Reproducible Fabrication of Integrated Optical Components by Charge Controlled Ion Exchange in Glass. *Proceedings of SPIE 1988*, Vol.993 : p7–12, 1988.

[18] J. Albert and J.W.Y. Lit. Full modelling of field-assisted ion exchange for graded index buried channel optical waveguides. *Applied Optics*, 29(18) : p2798–2804, 1990.

[19] B. Pantchev, P. Danesh and Z. Nikolov. Field-assisted ion exchange in glass: The effect of masking films. *Applied Physics Letters*, 62(11) : p1212–1214, 1993.

[20] D.L. Lee. Electromagnetic Principles of Integrated Optics. *J. Wiley & Sons*, New York, Ch. 6, 1986.

[21] R. Ulrich and R. Torge. Measurement of Thin Film Parameters with a Prism Coupler. *Applied Optics*, 12(12) : p2901–2908, 1973.

Chapter 6

Indiffused Waveguides in Yttrium Vanadate

6.1 Introduction

Indiffusion, as a method for the fabrication of optoelectronic devices, was born from the desire to produce waveguides in crystals such as lithium niobate ($LiNbO_3$) and lithium tantalate ($LiTaO_3$) [1–3]. Much of this work was dedicated to determining the possibility of producing integrated optoelectronic devices, that take advantage of the inherent acousto-optic, electro-optic and non-linear properties of these crystals. These devices often require active and passive regions to be fabricated on the same substrate, a requirement that negates the use of bulk doped crystals. Indiffusion has been successfully used to allow the local doping of active regions, and the creation of passive waveguides [4–6].

Local doping of active and passive regions is also attractive for the production of high output power tapered waveguide lasers, as will be discussed in the following chapter. This chapter details the first indiffusion of neodymium, gadolinium and titanium into yttrium vanadate (YVO_4), and the production of the first diffused waveguide in this important material. The use of yttrium vanadate as a substrate material is particularly attractive due to its high absorption coefficient of diode-pump sources, possibly allowing efficient side-pumped tapered waveguides.

6.2 Indiffusion: Historical Summary

A summary of indiffusion requires a short explanation of the process. The first step in the production of an indiffused waveguide is the deposition of a metal onto the surface of a crystal. The crystal is then heated to high temperature (1000–2000°C). During the heating process metal ions gain sufficient energy to diffuse into the crystal lattice, and are incorporated by substitution with original ions in the lattice, or by taking up interstitial sites. Indiffusion has the advantages that it is a very simple fabrication technique that requires little sample preparation, and it allows the local doping of crystals with many different ions for purposes of waveguide fabrication and/or laser action. However, the process can be prohibitively long, at times requiring heating for over $200hr$, dependent on the diffusion properties of the diffusant ion and the host crystal.

The fabrication of optical waveguides by indiffusion was first utilised in semiconductors [7,8]. Interest was initiated into the diffusion properties of $LiNbO_3$ and $LiTaO_3$ through the desire to access the electo-optic, acousto-optic and non-linear properties of these crystals, whilst allowing the optical confinement and manipulation of modes afforded by waveguide technology. The production of passive waveguides in $LiNbO_3$ and $LiTaO_3$ by titanium, vanadium and nickel indiffusion was first completed by Schmidt et. al. [1]. As a consequence of Schmidts' work, titanium indiffusion has become one of the two commonly used procedures for the production of passive waveguides in $LiNbO_3$ and $LiTaO_3$. The alternative technique is proton exchange (PE), which has the disadvantage of producing waveguides that support only TM modes [9]. Indiffusion has proved to be a very flexible fabrication technique, successfully producing devices such as tunable [10] and mode-locked lasers [11] and numerous passive devices such as mode-splitters [12] and Mach-Zehnder modulators [13].

Active waveguides were first produced by the indiffusion of titanium into bulk doped crystals [5]. This process has two drawbacks: it does not allow the selective doping of the crystal, nor does it match the waveguide and gain distributions. A two-step process was developed to achieve this goal,

which restricts the active ion dopants to a planar layer at the top surface of the crystal. The first step is the production of a doped layer, created by a planar indiffusion of active ions. The second step is the production of waveguides in the doped planar layer, by the indiffusion of passive ions from a patterned metal source. This method has been used to create waveguide lasers doped with Yb [9], Nd [6], Tm [14] and Er [4,15].

Total confinement of the active ions to the waveguide region is also possible with the two-step process, through the indiffusion of a patterned source of active ions, followed by a second indiffusion from a patterned source of passive ions [16]. The process requires very accurate pattern reproduction, and an active and passive ion with reasonably different diffusion coefficients, so as not to radically alter the profile of the first diffusion, during the second diffusion. A more elegant solution is gained through the use of the diffusant ion as both the active ion and the index modifier. The fabrication is simplified, as only one diffusion is required, and an identical dopant and index distribution is produced in the waveguide. To the present date, this goal has only been achieved in sapphire doped with titanium [17].

6.3 Indiffusion Theory

The underlying physics that controls ion exchange and indiffusion are fundamentally linked. In both cases a source of diffusant ions experiences a concentration gradient that causes migration of the ions into a substrate material. The migration of ions is limited by the ion energy, which must be greater than the activation energy for the process. The ions gain sufficient energy to overcome the activation energy through heating. The activation energy E_A and diffusion temperature T, are linked with the diffusion coefficient D through the Arrhenius equation [18]:

$$D = D_0 e^{\left(-\frac{E_A}{kT}\right)} \tag{6.1}$$

Where D_0 is the diffusion constant and k is Boltzmanns constant.

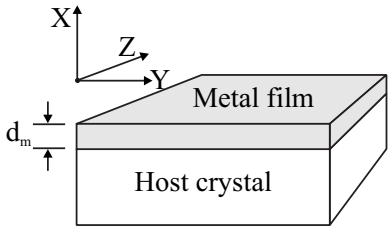

Figure 6.1: Coordinate system of indiffusion theory

In the majority of cases, the diffusant ions available for exchange during the ion exchange process are practically infinite, inasmuch that the ions contained within the salt far outnumber the ions available for exchange in the glass. This highlights the difference between ion exchange and indiffusion: as indiffusion normally occurs from a thin metal film of diffusant ions (figure 6.1), it is possible to fully deplete the source.

The one dimensional flux of diffusant ions J_x into a host crystal, is proportional to the concentration gradient with the one-dimensional diffusion coefficient D_x as the constant of proportionality [18]:

$$J_x = -D_x \frac{dC(x)}{dx} \tag{6.2}$$

Where $C(x)$ is the concentration of the diffusant ions.

The condition of mass conservation links the evolution of the concentration over time t, with the spatial differential of the flux:

$$\frac{dJ_x}{dx} = -\frac{dC(x)}{dt} \tag{6.3}$$

Substituting 6.2 into 6.3 produces the indiffusion equation:

$$\frac{dC(x)}{dt} = D_x \frac{d^2C(x)}{d^2x} \tag{6.4}$$

The one-dimensional indiffusion equation with relevant boundary conditions, can be solved to allow calculation of the concentration gradient within the host crystal.

6.3.1 Solution to the One-dimensional Indiffusion Equation

The solution of the indiffusion equation in one-dimension is dependent upon the thickness of the diffusant ion source d_m. The source is assumed to be infinite in two dimensions (Y and Z, from figure 6.1) and either infinite or finite in one dimension (X).

6.3.1.1 Solution to the Indiffusion Equation for an Unlimited Source

A sufficiently thick source of diffusant ions, which will not be greatly depleted during the diffusion can be assumed to be infinite in extent, as the supply of diffusant ions to the surface is constant throughout the diffusion. A constant supply of diffusant ions is also the case with TIE, and the following solution can be seen to be identical to that shown in section 4.3.1. The surface concentration is maintained at the solubility of the diffusant ions, whilst the number of ions incorporated into the sample and the diffusion depth increases with time. Applying the following condition for the metal:

$$d_m \rightarrow \infty \tag{6.5}$$

with the boundary conditions for the indiffusion:

$$\begin{aligned} C(x=0, t=0) &= C_s \\ C(x>0, t=0) &= 0 \\ C(x=0, t) &= C_s \end{aligned} \tag{6.6}$$

Allows the indiffusion equation to be solved and, in this case, it is found to be an erfc function [18] characterised by the maximum solubility of the diffusant ion C_s, the diffusion coefficient D and the diffusion time t.

$$C(x,t) = C_s \left[1 - \int \exp\left(-\frac{x^2}{4Dt}\right)\right] = C_s erfc\left(\frac{x}{2\sqrt{Dt}}\right) \tag{6.7}$$

Where $C(x,t)$ is the concentration profile.

The depth of the diffusion is characterised by the value $d_{diff} = 2\sqrt{Dt}$. The diffusion depth occurs at the point $erfc(1)$ and can therefore be determined experimentally with SIMS analysis (as described in section 4.5) , which in turn allows calculation of the diffusion coefficient.

6.3.1.2 Solution to the Indiffusion Equation for an Instantaneously Depleted Source

The other extreme of the indiffusion process is that of the instantaneous diffusion. If the metal source is fully incorporated into the host crystal, the thickness of the source can be assumed to be infinitesimal in extent. The supply of diffusant ions is therefore limited to the total number of ions within the metal source. As the number of diffusant ions within the crystal is constant, the surface concentration must reduce as the diffusion depth increases with increasing diffusion time. Applying the condition for the metal:

$$d_m \rightarrow 0 \tag{6.8}$$

with the boundary conditions for the indiffusion:

$$\begin{aligned} &\int C(x=0,t=0)dx = N_{tot} \\ &C(x>0,t=0) = 0 \\ &\int_0^\infty C(x,t)dx = N_{tot} \end{aligned} \tag{6.9}$$

Allows the indiffusion equation to be solved and, in this case, it is found to be a Gaussian [18], characterised by the total number of diffusant ions per unit area N_{tot}, the diffusion coefficient D and the diffusion time t.

$$C(x,t) = \frac{N_{tot}}{2\sqrt{\pi Dt}} \exp\left(-\frac{x^2}{4Dt}\right) \tag{6.10}$$

Where $C(x,t)$ is the concentration profile.

The diffusion depth is again characterised by the value $2\sqrt{Dt}$ which occurs at the point where the power of the exponent becomes $= -1$ i.e. at e^{-1}.

In practise the indiffusion profile can be either of the above extremes, or a combination of the two profiles, a 'transitional diffusion'. The diffusion may also be affected by diffusion through crystal defects, varying diffusion rates in different directions through the crystal, outdiffusion of the diffusant ions from the crystal or a chemical reaction occurring between the diffusant ions and the crystal. The diffusion coefficient will be characterised by fitting the theoretical profiles onto actual diffusant ion profiles generated by SIMS analysis. This will allow the effective diffusion coefficient to be calculated, which is the sum of all the diffusion routes and therefore the practical value required for production of waveguides in the host crystal.

6.4 High Power Tapered Waveguides

In the most simple sense, to achieve high output power from a waveguide laser there are two requirements. The laser must operate efficiently, and it must be pumped with a high-power pump source. The requirement for efficient operation is fulfilled by tailoring of the waveguide and resonator properties, and the use of an efficient laser transition, such as the four-level transition of the Nd^{3+} ion. High pump powers are most efficiently accessed by the use of diode-bar lasers as pump sources [19–21]. To date, diode-pumping of indiffused waveguides has utilised low power, single-mode pump sources ($\leqslant 200mW$) [22, 23]. The following sections investigate the possibilities of pumping indiffused waveguides with high-power diode-bars.

6.4.1 Material Requirements of Diode-pumped, Tapered Waveguide Lasers

The high power operation of tapered waveguides formed by ion exchange (chapters 4 and 5), is limited by the ability to efficiently couple the highly divergent and multimode pump beam from a diode-bar laser into the waveguides. Efficient diode-end-pumping of a tapered waveguide would require a taper width of $\approx 5mm$. As discussed in chapter 3, the constraint of adiabatic operation on the taper limits the maximum taper opening to widths of approximately $300\mu m$, in a substrate of reasonable length. The TIE waveguide lasers are also limited by the low numerical aperture (NA) of the potassium ion exchange process. If the waveguides are assumed to be step-index, then the NA can be calculated from the following equation:

$$NA = \sqrt{n_2^2 - n_1^2} \tag{6.11}$$

Where n_1 and n_2 are the substrate and waveguide refractive indices respectively.

Equation 6.11 produces values of 0.16 and 0.17 for the TE and TM modes respectively, for a K^+–Na^+ TIE waveguide.

The main factor which inhibits the efficient launch of a diode-bar into a tapered waveguide is the extremely poor beam quality in the slow axis, coupled with the constraints on the maximum taper width. The NA required to launch a diode-bar pump into a taper of width W can be estimated as follows [20]:

$$NA \geqslant \frac{\lambda M^2}{W} \tag{6.12}$$

Where λ is the pump wavelength and M^2 represents the factor by which the beam divergence of the diode-pump exceeds the diffraction limit.

M^2 values of a diode-bar in the slow axis are typically 1000–2000 requiring a NA approximately two orders of magnitude greater than that created by potassium TIE, in conjunction with the allowed width of the waveguide.

The requirement for containment of the diode pump within the depth of the tapered waveguide must also be considered, although the constraints are reduced, as the diode-bar quality is far superior in the fast axis with M^2 values between 2 and 5 being typical. Unlike the maximum taper width, theoretically the only limit on the waveguide depth is the duration of the indiffusion, which allows the depth of the waveguide to be tailored to allow a greater NA-depth product and reasonable confinement of the pump beam in this direction.

As has been shown, the high-power operation of diode-bar end-pumped, tapered waveguides is limited by the inability to efficiently couple the slow-axis of the diode-bar pump into the waveguide. However, a solution to this problem may be presented by changing the pump geometry. It is reasonable to assume that the constraints on the waveguide width could be solved by diode-side-pumping the broad section of the tapered waveguide [24] (figure 6.2).

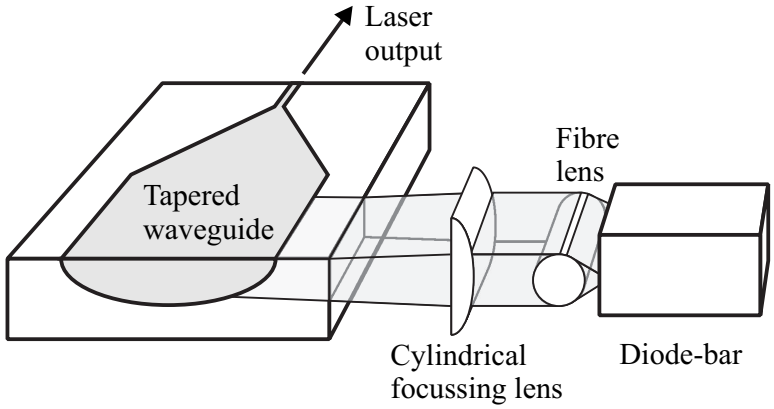

Figure 6.2: Possible geometry for a diode-side-pumped tapered waveguide laser

6.4.2 Side-pumping of a Tapered Waveguide

The most obvious benefit of diode-side-pumping, when dealing with an indiffused tapered waveguide laser, is that this pump configuration is the only one to allow high coupling efficiency and reasonable absorption of the diode pump. Face-pumping could also be utilised, and would benefit from lower constraints placed on focussing of the diode laser, but the very

shallow depth envisaged with indiffused waveguides ($< 10\mu m$) would lead to very low pump absorption.

Side-pumping has the additional benefit that it simplifies the power scaling of the waveguide laser, as the incident pump power can be scaled by increasing the length over which the waveguide is pumped. The incident pump power can be increased further by pumping both side-faces of the waveguide, which would also produce a more uniform gain profile leading to improved power extraction [25].

The use of diode-side-pumping poses three distinct problems:

1. A material with a short absorption length is required to fully absorb the pump over the taper width ($\approx 300\mu m$)
2. Side-pumping a bulk doped substrate is wasteful, as absorption is not limited to the waveguide regions.
3. The low NA in the direction of waveguide depth is not improved with a side-pumped geometry.

The solution to the first two problems are found by the use of a new substrate material with a short absorption length, and the local doping of that material. Neodymium doped yttrium vanadate, has been shown to have an absorption length comparable to the width of the broad section in a tapered waveguide [26]. Local doping of Nd^{3+} into YVO_4 could be realised with the use of indiffusion, which may have the secondary benefit of creating an index change sufficient for guidance of the laser mode.

Improving the NA of the waveguide poses more of a problem. As discussed in the following section, the indiffusion of three diffusant ions: Nd^{3+}, $Gd^{3+}$and Ti^{x+} will be investigated in YVO_4 (where the x in the ionic charge on the Ti^{x+} ion denotes that the charge on the Ti ion within YVO_4 is not known). An indication of the refractive index change due to the doping concentration is required to allow calculation of the possible waveguide NA. A reasonable assumption is that the index change due to Nd^{3+} is similar to that found in YAG (4.2×10^{-4} per $at\%$) [27], and that the index

change due to Gd^{3+} doping follows a linear relationship between $GdVO_4$ and YVO_4 (2.4×10^{-4} per $at\%$). The index change due to Ti^{x+} doping is more difficult to estimate, but it can be assumed that the index change will not be radically different to the values generated for Nd^{3+} and Gd^{3+} doping. If equation 6.11 is rearranged and the value for n_2 is modified to become $n_1 + cn_{cfn}$, where c is the concentration of the dopant ion in $at\%$ and n_{cfn} is the index change per $at\%$, then the required concentration can be stated:

$$c = \frac{\sqrt{NA^2 + n_1^2} - n_1}{n_{cfn}} \tag{6.13}$$

The following fabrication section assumes an initial waveguide depth of $10\mu m$, so this value will be used for the calculation. A diode-bar output with M^2 of 2 in the fast-axis, at a wavelength of $807nm$, is also assumed. To achieve a waveguide NA equal to that of the diode-bar would require dopant concentrations of $\approx 15at\%$ with Nd^{3+} doping and $\approx 25at\%$ with Gd^{3+} doping. Notwithstanding the fact that crystals doped with $> 3at\%$ of Nd^{3+} suffer from concentration quenching, these very high doping levels would require impossibly high surface solubilities, and may cause severe damage to the crystal. To conclude, a waveguide with a sufficiently high NA and depth would be impossible to create through indiffusion. However, this problem may be circumvented by incorporating a second fabrication technique with the indiffusion. Contact bonding of materials with different refractive indices has proven to be a powerful method for the production of high NA waveguides [20, 28]. It is reasonable to assume that an indiffused tapered waveguide could be created in YVO_4 and this could be contact bonded between two layers of another crystal with a different refractive index, to create a waveguide with a sufficient NA to contain the diode-pump beam. However, the work contained in this thesis will concentrate on only the indiffusion properties of waveguides in YVO_4.

6.4.3 Yttrium Vanadate as a Material for High Power, Indiffused Waveguides.

Although recently there has been a high degree of interest in yttrium vanadate, the technology itself is reasonably old: the crystal was first grown by Van Uitert et. al. in 1962 [29], with the first laser study made in 1966 [30]. Further studies on the laser performance of this crystal host have shown it to be an efficient gain medium for diode pumped lasers [31–33].

The strengths of Nd:YVO_4 as a laser crystal for diode pumping, are best illustrated by comparison with the more common laser crystal Nd:YAG, and are shown numerically in table 6.1 [26, 34]. The values in table 6.1 are shown for $1at\%$ Nd^{3+} doped crystals. The units used to specify pump bandwidth, require explanation: FW 75% refers to the wavelength range (in nm) where at least 75% of the diode light is absorbed in a 5mm pathlength.

Nd:YVO_4 benefits from a large stimulated emission cross-section, which can lead to a high gain, a wide pump bandwidth, which reduces the constraints on maintaining the wavelength of the diode pump, and a high absorption coefficient leading to reduced crystal sizes.

Nd:YVO_4 suffers from one major disadvantage: its thermal conductivity is approximately half that of Nd:YAG. The low thermal conductivity leads to a large temperature gradient during laser operation, which limits the maximum incident pump power. Studies of diode-end-pumped Nd:YVO_4 crystals, have shown that high pump intensities can lead to thermal shock and fracturing of the crystal [35]. The problem can be overcome with the use of lower Nd^{3+} doping concentrations, but this requires longer crystals to attain reasonable absorption, leading to higher propagation losses. The proposed ultra-thin, slab geometry of the waveguide is ideal for thermal management [19] and should reduce thermal effects to within manageable levels.

The property of Nd:YVO_4 most relevant to the following work with side-pumping, is its large absorption coefficient. A diode pump beam at a wavelength of $808nm$, with its polarisation aligned to the c-axis of the crys-

Characteristic	Nd:YAG	Nd:YVO_4
Stimulated emission cross-section ($10^{-19}cm^2$)	2.8	15.6
Peak absorption coefficient at 808nm (cm^{-1})	8.5	37 (c-axis) 10 (a & b-axis)
Pump bandwidth (FW 75%)	2.5	15.7
Thermal Conductivity ($Wm^{-1}K^{-1}$)	10.3	5.14

Table 6.1: Comparison of Nd:YAG and Nd:YVO_4 laser characteristics

tal, would allow access to an absorption coefficient of $37cm^{-1}$ with a $1at\%$ Nd^{3+} doped crystal. The absorbed power P_{abs} can be calculated from the following equation:

$$P_{abs} = P_{inc}(1 - e^{-\alpha l}) \tag{6.14}$$

Where P_{inc} is the incident power, α is the absorption coefficient and l is the length of the crystal.

The absorption length l_{abs} is defined as the length of crystal where the transmitted power drops to e^{-1} of its original value (i.e. $l_{abs} = \alpha^{-1}$). A $1at\%$ Nd^{3+} doped YVO_4 crystal would have an absorption length of $270\mu m$, a value comparable to the maximum taper widths produced thus far ($250\mu m$).

The strengths of Nd:YVO_4 as a laser host are clear, but there has been no research into the diffusion properties of the crystal. Consequently, the diffusion characteristics and the performance of a diffused waveguide in this material were unknown. For these reasons the following work was completed to initially investigate the diffusion characteristics of three different diffusant ions: neodymium, gadolinium and titanium. Indiffusion of neodymium is a requirement for laser gain, and therefore its diffusion properties must be investigated. The perfect situation would arise from the use of neodymium as the active dopant and the refractive index modifier, allowing the production of a doped waveguide in one fabrication step. The diffusion of titanium and gadolinium were investigated as they may be useful index modifiers for a two-step diffused waveguide as explained

in section 6.2. Gadolinium vanadate is known to have a higher refractive index than YVO_4 and occupies the same crystal site as Y^{3+}, making it the perfect index modifier. Titanium was also investigated as an index modifier. Titanium is known to have a high diffusion coefficient in $LiNbO_3$ and sapphire, and may therefore have a high diffusion coefficient in YVO_4, allowing the production of waveguides in reasonably short times. The titanium atom possesses a smaller atomic radius than both Nd and Gd ($176pm$ as opposed to $206pm$ and $233pm$ for Nd and Gd respectively), which may lead to a larger diffusion coefficient in relation to these ions.

Investigation of the diffusion characteristics would allow the design and testing of diffused waveguides, which in turn would allow the fabrication of an optimum waveguide for diode pumping.

6.5 Fabrication

The samples produced by indiffusion underwent near identical fabrication techniques. Differences in fabrication were limited to the diffusant ion used (Nd^{3+}, Gd^{3+} or Ti^{x+}), the diffusion temperature (1400 or 1600°C) or the diffusion time. The following section details the standard fabrication procedure for an indiffused waveguide. Any differences in the fabrication of the indiffused samples will be noted in the results section.

6.5.1 Sample Preparation

Undoped, c-cut YVO_4 crystals, of dimensions 18 (a-axis) x18 (b-axis) x3mm (c-axis), were purchased from the supplier Casix. The two largest faces were polished by the supplier. The samples were cleaned of organic and inorganic contaminants using an identical procedure to that listed in section 4.4.1. The only difference noted in the cleaning of the samples was related to the use of the Piranha wash. Problems had already been encountered with glass samples cracking due to the sudden heating involved with this wash. YVO_4 has a low thermal conductivity ($\approx 5Wm^{-1}K^{-1}$) , which became apparent as every sample subjected to the Piranha wash

cracked. For this reason only the low temperature fuming-nitric wash was used to clean YVO_4 samples.

6.5.2 Deposition of a Diffusant Metal Layer

The diffusion coefficients, and the surface solubilities of all three diffusant ions were unknown in YVO_4, so the initial thickness of the metal could not be calculated using equation 6.7 or 6.10. To allow initial diffusions to be made, assumptions of the doping level within the crystal were required. The value of the surface solubility and the diffusion coefficient could then be calculated, which would allow later waveguides to be designed with specific concentrations and diffusion depths. It was assumed that the diffusion would create a uniformly-doped, step-like diffused area as shown in figure 6.3. A computer package was used to model waveguide modes at $1.06\mu m$ in a uniformly doped waveguide, using the estimated values for the refractive index change due to Nd^{3+} and Gd^{3+} doping (section 6.4.2). A depth of $10\mu m$ was found to produce a single mode waveguide with a Nd^{3+} doping of $1at\%$. The low value of Nd^{3+} doping was chosen to counter cross-relaxation effects that occurs at higher doping levels ($> 3at\%$). A level of Gd^{3+} doping was calculated that also produced a single-mode waveguide at a diffusion depth of $10\mu m$. As the index change due to titanium doping was not known it was decided to start with a diffusant metal layer $100nm$ thick.

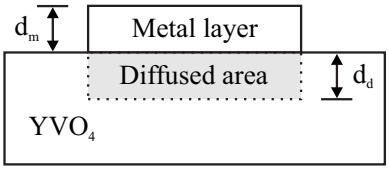

Figure 6.3: Diagrammatic representation of the metal thickness and diffusion depth used for the initial calculation of the metal depth required for indiffusion

The volume of metal required V_m and the step-like diffusion volume V_d can be related through the following equation.

$$V_m = c \times \frac{V_d M_m}{M_{YVO_4}} \tag{6.15}$$

Where c is the fractional doping level and M_m, M_{YVO_4} are the molar volumes of the metal and YVO_4.

As the diffusion is carried out over the same surface area of metal and YVO_4, the area in the volume calculations can be cancelled, producing an equation relating the metal depth d_m, to the step-like diffused depth d_d:

$$d_m = c \times \frac{d_d M_m}{M_{YVO_4}} \tag{6.16}$$

The values used in this calculation, and the values generated by it, are shown in table 6.2.

Each of the metals was purchased with a purity of 99.9%, from the supplier Goodfellow. A layer of each metal was thermally evaporated onto the surface of a YVO_4 crystal, using an Edwards 309 thermal evaporator. After evaporation the metal layer thickness was measured with an Alphastep profilometer, as the metal thickness recorded by the Edwards evaporator is open to error. The values for thickness measured by the profilometer are listed in the 'Actual d_m' column of table 6.2.

A useful side-effect of the sample holders used in the Edwards evaporator, is the production of uncoated, right-angled, triangular areas of $\approx 2mm$ per side, on two opposite corners of each sample. These areas were used post-indiffusion to give an indication of how the uncoated crystal reacted to the diffusion temperatures and times.

Metal	Molar Mass g	Density at 20°C gcm^{-3}	Doping concentration $at\%$	d_m nm	Actual d_m nm
Nd	144	7	1	43	55
Gd	157	7.85	1	38	40
Ti^{x+}	48	4.5	4	88	100

Table 6.2: Metal thicknesses for initial diffusions

6.5.3 Indiffusion

Practical values for the diffusion temperature and duration were unknown for the three diffusant ions in YVO_4. Indiffusions in $LiNbO_3$ are often carried out near $1000℃$, to maintain the poling of the crystal, as its Curie temperature is situated at $1140℃$ [9]. YVO_4 is not ferroelectric, and therefore does not suffer from poling loss, which allows the indiffusion to be completed at any temperature below its melting point ($1825℃$), although diffusion near the melting temperature may cause sample distortion and loss of polish quality. Diffusion at higher temperature is advantageous, as it reduces the process duration. For this reason the following diffusions were carried out at $1600℃$, the maximum temperature afforded by the furnace used for this work. Diffusions were also completed at $1400℃$, to allow calculation of the activation energy from equation 6.1.

Another assumption was required to gain a starting value for the duration of the indiffusion. Previous work with indiffusion (section 6.2) had shown that waveguide production was possible in $LiNbO_3$ through diffusion durations of 8–$300hr$, at temperatures around $1000℃$, and in sapphire through diffusion durations of 1–16 hours, at temperatures between 1500–$2000℃$. Although waveguide production in YVO_4 would be desirable, it was not necessary for the calculation of the diffusion coefficient. It was assumed that at temperatures between 1400–$1600℃$, appreciable diffusion would occur in times between 10 and $24hr$.

During the diffusion the samples were held within a platinum sheet, folded into a box shape. The box shape helped to prevent particulates, which build up on the furnace walls, from collecting on the surface of the sample. The sides of the box were left open to allow air flow over the sample. The furnace was ramped to either 1400 or $1600℃$ and after reaching this temperature was given an hour to settle into thermal equilibrium. During this time an oxygen flow of $10lmin^{-1}$ was created to produce an oxygen rich atmosphere. The oxygen flow was maintained throughout the diffusion in an attempt to prevent outdiffusion of oxygen from the YVO_4 crystal. Outdiffusion of lithium oxide occurs during diffusion of lithium

Sample no.	Metal	Temperature ℃	Duration hr
1	Nd	1400	24
2	Nd	1400	120
3	Nd	1600	10
4	Gd	1400	12
5	Gd	1400	24
6	Gd	1600	12
7	Ti^{x+}	1400	12
8	Ti^{x+}	1400	24
9	Ti^{x+}	1600	12
10	Ti^{x+}	1600	24
11	Nd	1600	700

Table 6.3: Fabrication parameters of indiffused waveguides

niobate and causes severe degradation of the sample. Dry and wet oxygen atmospheres have been shown to inhibit outdiffusion by creating a concentration of oxygen that is higher in the furnace atmosphere, than in the crystal [23,36]. It was not known whether outdiffusion would occur in YVO_4, so the oxygen flow was used as a precautionary measure.

A single, metal coated YVO_4 sample, held within the platinum box, was placed at the mouth of the furnace. The sample was pushed into the furnace hot-zone by the following procedure: 10 minutes at the mouth of the furnace, then 10 minutes at points 25 and 55cm further into the furnace. The final push moves the sample 70cm into the furnace where the hot-zone is situated. The diffusion time was said to have started once the crystal was in the hot-zone. Once the set diffusion time had elapsed the sample was removed from the furnace using identical steps. Table 6.3 lists the diffusion conditions for each indiffused sample,.

An uncoated crystal was diffused for $24hr$ at 1600℃, to test whether this temperature regime caused any adverse effects on the crystals surface. The crystal was examined visually and with the aid of an alpha-step surface profilometer, and was not noticeably affected by the temperature over this time.

A 1mm section was cut from each end of the diffused sample to remove

diffusion edge-effects. The samples were end-face polished, parallel to the c-axis in preparation for the following characterisation.

6.6 Characterisation

6.6.1 Surface Defects

Post-diffusion, two distinct surface defects were noticed on some of the samples. The first defect consisted of a layer of a white compound, found on the areas which were coated with metal. This effect has been encountered with indiffusion in $LiNbO_3$, and is caused by left-over, oxidised metal. Due to its appearance, this defect has been named 'orange peel' (figure 6.4). A further indiffusion can remove this layer completely [6], however, to maintain the diversity of the sample indiffusion times, the layer was removed with a 15–25 minute hand polish [1, 6], which leaves the diffused layer intact.

The second surface defect was observed on a small number of samples and consisted of a number of fine $\approx 200nm$ deep cracks situated either on the edges of the samples, or distributed over the entire surface (figure 6.4). The cracking is not caused by thermal effects, as uncoated crystals subjected to identical diffusion conditions do not show the effect. The effect is also absent on the bottom face of the substrates, which is polished to the same finish as the top surface, and would therefore be expected to react identically. The number of cracks appeared to increase with temperature, and was seen to be more prevalent on some batches of crystals. The cause of the effect has not yet been proven, but it is expected to be linked to the quality of the surface polish, as some batches of crystals showed no cracking at all, whilst other batches suffered from considerable cracking. Stress in the crystal, due to the high doping concentrations gained through some of the indiffusions (up to $12at\%$) could also be a cause of the cracking. The cracked surface layer can be removed with a hand-polish, which must remove $\geqslant 200nm$ of material from the top surface of the waveguide to gain a flat surface. The effect on the waveguide of the removal of this amount

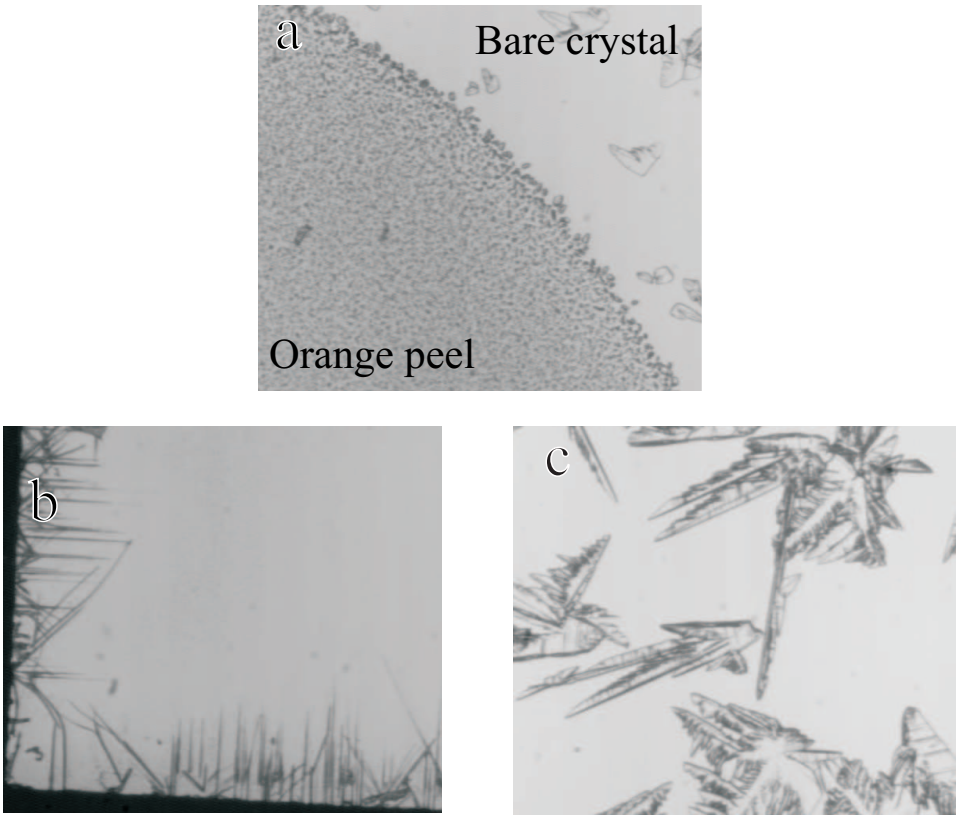

Figure 6.4: Surface defects present after indiffusion: a/ orange peel, b/ edge cracking, c/ surface cracking

of material is dependent on the depth of the waveguide.

The following characterisation required the removal of the orange peel from the samples affected by it, as it would affect the results of SIMS analysis. The metal ions would also cause absorption of the laser radiation used during optical characterisation. The degree of surface cracking on the samples dictated whether the surface was polished to remove the cracks.

6.6.2 SIMS Analysis

SIMS analysis, identical to that discussed in section 4.5, was used to determine the diffusant concentration and profile of each indiffused sample.

6.6.3 Calibration of SIMS data

SIMS analysis produces a profile of a variable 'counts' against depth in the sample. The value of 'counts' is the product of the number of analysed ions present in the sample, the beam current and the sensitivity of the SIMS apparatus to the analysed ion. The sensitivity K is related to the ion concentration as follows:

$$Counts = K \times ions/volume \tag{6.17}$$

The known surface refractive index created by K^+–Na^+ TIE in BK7 allowed simple calibration of the count data for the TIE waveguides. A similar method is not possible with indiffusion in YVO_4, as the surface refractive index created by the indiffusion of the three diffusant ions, is not known. There are two alternative calibration methods. SIMS analysis can be completed on a bulk doped sample of known concentration, which allows calculation of the sensitivity of the SIMS apparatus to the analsyed ion. The data for the indiffused sample is normalised to the bulk sample, to account for any differences in the beam current. The normalisation is completed with reference to the vanadium ion, as the concentration of vanadium present in the crystal is assumed to be unaffected by the indiffusion process, or by bulk doping. This method requires the availability of a bulk doped sample and was used to calibrate the Nd^{3+} indiffused samples.

No bulk doped samples of Gd:YVO_4 and Ti^{x+}:YVO_4 were available, so an alternative mathematical method was used. It is known that a Gaussian profile implies instantaneous diffusion, and hence, the full incorporation of the metal film into the crystal. To calibrate the data each SIMS profile is fitted to a Gaussian function and the sample with the closest match is used for the calibration. The calculated Gaussian profile is integrated, which in a physical sense produces a value for the area A under the profile, in units of counts·depth (i.e. in units of counts multiplied by depth). The area is related to the sensitivity by the following equation:

$$A = KN_{area} \tag{6.18}$$

Where K is the sensitivity of the SIMS apparatus to the particular ion, in units of counts·volume per ion, and N_{area} is the number of diffusant ions per unit area.

The total number of diffusant ions N supplied during the indiffusion can be calculated through the equation:

$$N = \frac{\rho_m V_m A_v}{\mu_m} \tag{6.19}$$

Where ρ_m is the density of the metal, V_m is the volume of the metal, A_v is Avogadro's number and μ_m is the molar mass of the metal. The equation is rearranged to allow calculation of the total number of ions supplied, per unit area N_{area}:

$$N_{area} = \frac{\rho_m d_m A_v}{\mu_m} \tag{6.20}$$

Where d_m is the depth of the metal. Equation 6.20 allows calculation of K, and hence the ions per volume, which in turn can be related to the concentration of ions in $at\%$.

Both calibration techniques were applied to the Nd^{3+} indiffused samples, to investigate the accuracy of the mathematical calibration method. An average difference of 5% was calculated, which is well within experimental error and verifies the mathematical calibration technique.

6.6.4 Fitting of SIMS data to Theoretical Profiles

The SIMS data was fitted to the theoretical indiffusion profiles using computational software, with the closest fit attained using a least squares method. The software fitted the following profiles to the SIMS data:

$$y = \alpha e^{-\frac{x^2}{\beta}} \tag{6.21}$$

$$y = \gamma erfc\left(\frac{x}{\delta}\right) \tag{6.22}$$

Where equation 6.21 is the Gaussian fit that represents the profile for a fully depleted source and equation 6.22 is the erfc fit that represents the profile for an undepleted source. The variables α, β, γ and δ are fitting parameters derived from equations 6.10 and 6.7 respectively, and are therefore equal to:

$$\begin{aligned} \alpha &= \frac{N_{tot}}{2\sqrt{\pi Dt}} \\ \beta &= 4Dt \\ \gamma &= C_s \\ \delta &= 2\sqrt{Dt} \end{aligned} \tag{6.23}$$

Where the variables are defined identically to those in section 6.3.

The values for each curve fit are listed in table 6.4. The $\bar{r}_p$ shown in bold indicates the smallest error, and therefore indicates which theoretical profile best fits the SIMS data. Figure 6.5 and 6.6 show examples of the SIMS data (shown in black) and the fitted data (shown in red).

Sample no.	Metal	$\bar{r}_p$ (%)		d_{diff}	Temperature	Diffusion coefficient
		Gaussian	Erfc	μm	℃	$\times 10^{-19} m^2 s^{-1}$
1	Nd	32.5	**9.1**	0.52	1400	7.8
2	Nd	**2.0**	25.5	0.98	1400	5.6
3	Nd	14.9	**7.2**	1.07	1600	80
4	Gd	11.5	**7.5**	0.84	1400	41
5	Gd	11.5	**8.8**	1.28	1400	47
6	Gd	**6.6**	7.1	1.71	1600	170
7	Ti^{x+}	83.1	**76.7**	0.23	1400	3.0
8	Ti^{x+}	**73.3**	78.2	0.21	1400	1.3
9	Ti^{x+}	12.3	**11.3**	1.08	1600	902
10	Ti^{x+}	8.7	**7.3**	1.08	1600	34
11	Nd	23.5	**15.2**	0.85	1600	0.7

Table 6.4: Error of fit, diffusion coefficient and diffusion depth for the indiffused samples

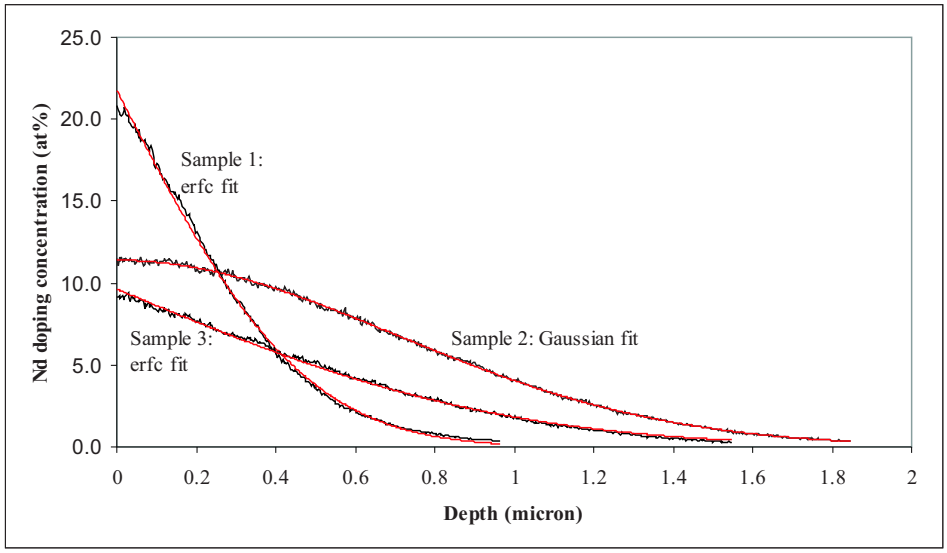

Figure 6.5: Indiffused profiles of neodymium indiffusions measured by SIMS analysis, in black, fitted theoretical profiles in red

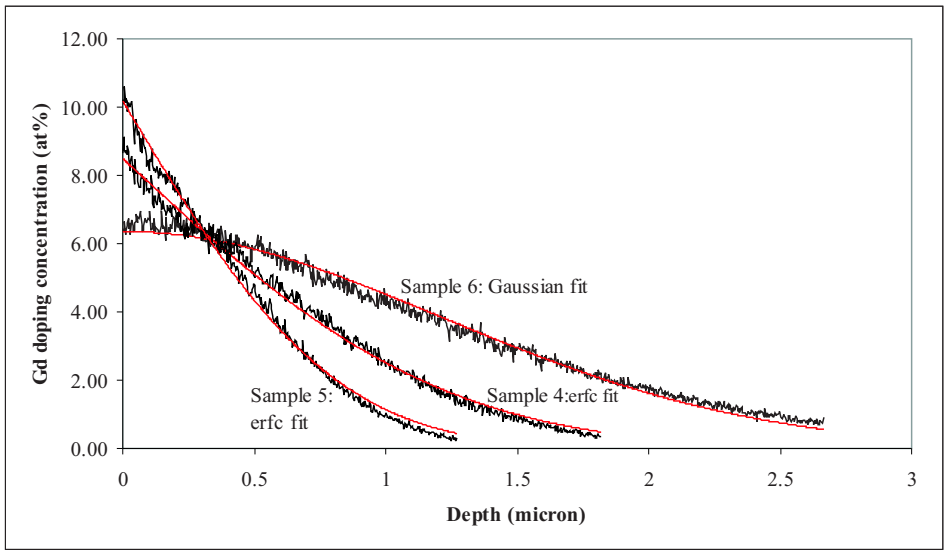

Figure 6.6: Indiffused profiles of gadolinium indiffusions measured by SIMS analysis, in black, fitted theoretical profiles in red

6.6.5 Calculation of Diffusion Properties

The calculation of the diffusion coefficient was completed by fitting each indiffused sample to a Gaussian and an erfc function. The profile that attained the closest match to the raw data was used for the calculation of the diffusion coefficient. Comparison of the profiles generated by the fitting software (equations 6.21 and 6.22), with reference to the theoretical profiles (equations 6.7 and 6.10), allows calculation of the diffusion depth d_{diff}:

$$\begin{aligned} d_{diff} &= \sqrt{\beta} \\ d_{diff} &= \delta \end{aligned} \tag{6.24}$$

In both cases $d_{diff} = 2\sqrt{Dt}$, which allows calculation of the diffusion coefficient. Table 6.4 lists the values for diffusion depth and the diffusion coefficient calculated for each of the three diffusant ions. The $\bar{r}_p$ value (derived in section 4.5) shown in bold indicates the profile which best describes the raw data, and was therefore used for the calculation of the diffusion coefficient.

The temperature dependence of the diffusion coefficient is given by:

$$D = D_0 e^{\left(-\frac{E_A}{kT}\right)} \tag{6.25}$$

Where k is Boltzmann's constant and T is the absolute temperature.

The diffusion coefficients, calculated at different temperatures, are used in the above equation to produce two simultaneous equations that are solved to produce values for the activation energy E_A and the diffusion constant D_0, which are listed in table 6.5. As only two temperatures were used for these calculations, these values can only be reliably used over the temperature range $1400 - 1600$℃.

Metal	Diffusion constant m^2s^{-1}	Activation Energy J
Nd	$7.9 \times \pm 0.1 \times 10^{-9}$	$5.3 \pm 0.7 \times 10^{-19}$
Gd	$1.3 \times \pm 0.1 \times 10^{-12}$	$2.9 \pm 0.4 \times 10^{-19}$
Ti^{x+}	$1.7 \times \pm 0.6 \times 10^{3}$	$1.2 \pm 0.2 \times 10^{-18}$

Table 6.5: Diffusion constants and activation energies

6.6.6 Discussion of SIMS Results

As no research has previously been completed on indiffusion in YVO_4, it is difficult to compare the results for the diffusion coefficients. Cherniak [37] investigated the indiffusion of various rare earth elements in YAG, and calculated a diffusion coefficient for Nd^{3+} of $4.2 \times 10^{-19} m^2 s^{-1}$ at 1400°C, which is comparable to the value calculated here. The diffusion coefficients of other rare earth ions (La^3+, Dy^3+ and Yb^3+) were calculated to be between 2.0–$4.5 \times 10^{-19} m^2 s^{-1}$ at 1400°C. The small variation in these results was attributed to the relatively similar ionic radius of the rare earth ions (101–$117pm$). For this reason the relatively high diffusion coefficient of Gd^{3+} is unexpected, but is favourable to the production of indiffused waveguides. In general the diffusions of Nd^{3+} and Gd^{3+} follow the expected relationship with the diffusion depth increasing with increased diffusion temperature and duration. The indiffusion of Ti^{x+} appears to follow this trend, but the results require some explanation.

A large difference between the values for $\bar{r}_p$ calculated for the erfc and Gaussian fit, would show that the indiffusion was acting at one extreme of the two possible indiffusion limits. This behaviour is seen with sample 2, which is a very close fit to a Gaussian, and for this reason was used when verifying the calibration of dopant concentration. The other Nd^{3+} indiffused samples exhibited a close fit to an erfc function, indicating a non-depleted source during the indiffusion. The initial conditions (based on a $1at\%$ doping and $10\mu m$ depth) for diffusant source thickness and diffusion duration have actually produced waveguides with depths ranging between $\approx 0.5\mu m$ and $\approx 1.0\mu m$, with correspondingly higher surface concentrations up to $12at\%$. It is therefore expected that all three sam-

ples would not produce efficient lasers due to extensive cross-relaxation at these very high doping concentrations [40].

The Gd^{3+} samples showed a lower differentiation between the two profiles, which would indicate that the indiffusion is in a transitional stage between the two extremes of instantaneous and infinite diffusion. A closer fit would be desired for sample 6, as this was the sample used to calibrate the indiffusions.

The Ti^{x+} indiffused samples showed an almost equal error in the fit to the two profiles. As no bulk-doped Ti^{x+}:YVO_4 samples were available, and none of the samples showed a close match to a Gaussian profile (with a high differentiation between profiles), these diffusions could not be calibrated. The low differentiation between the samples is not due to a transitional stage diffusion. The SIMS results show very low counts and hence imply very low concentrations of Ti^{x+} ions in the samples (figure 6.7). The concentration of Ti^{x+} was highest in the short, low temperature diffusion and decreased as the diffusion time or temperature increased. The maximum number of counts dropped by a factor of ≈ 1000 between the $12hr$, 1400°C and the $24hr$, 1600°C diffusions. The low Ti^{x+} concentrations, and shallow diffusion depth allows very little data to be fitted to a theoretical profile leading to an inaccurate fit and consequently inaccurate results for the diffusion properties. The values calculated for the diffusion coefficient, diffusion constant and activation energy are therefore not representative of Ti^{x+} indiffusion in YVO_4, which is reinforced by the radically different diffusion coefficients calculated for different diffusion times at the same temperature, and the extreme increase in the calculated diffusion constant.

The cause of the low Ti^{x+} concentration is thought to be either outdiffusion of the Ti^{x+} ions from the sample, or segregation of the diffusion. Segregation occurs as an oxide layer builds up on the surface of the sample. The diffusant ion has a higher affinity for the oxide layer and is drawn towards the surface of the sample where evaporation can occur [38, 39]. It is also possible that the Ti^{x+} film evaporated instead of indiffusing into the crystal, although this seems unlikely as Ti^{x+} indiffusion in sapphire has been completed successfully at higher temperatures than used with

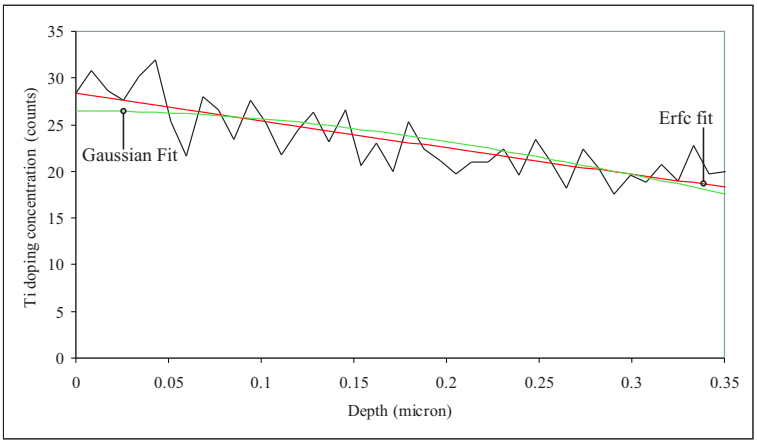

Figure 6.7: Indiffused profile and theoretical fitting data of a titanium indiffusion

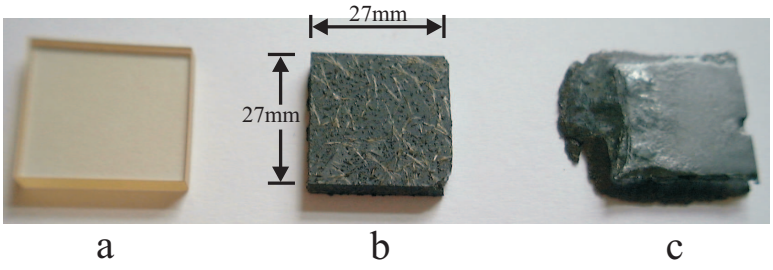

Figure 6.8: a/ bare YVO_4 crystal, b/ YVO_4 crystal after Ti^{x+} indiffusion in argon atmosphere, c/ YVO_4 crystal after Ti^{x+} indiffusion in vacuum

this work [17]. In an attempt to inhibit the growth of an oxide layer Ti^{x+} indiffusions were completed in a vacuum and an argon atmosphere. During these diffusions it was found that oxygen outdiffusion does occur - severely - in YVO_4, an $\approx 1mm$ thick layer over the crystal surface had blackened, and crumbled (figure 6.8). The combination of the Ti^{x+} outdiffusion in an oxygen atmosphere and the oxygen outdiffusion in a vacuum or ambient atmosphere halted the work with Ti^{x+} indiffusion in YVO_4.

The results for sample 11 also require some explanation. After determination of the diffusion coefficient of Nd^{3+} in YVO_4 from samples 1–3. It was calculated that a $700hr$ diffusion at 1600°C, from a metal source $125nm$ thick would created a single-mode waveguide at $1.064\mu m$. This diffusion was completed, but no waveguide was observed in the sample. SIMS analysis showed a surface doping level of $\approx 8at\%$ and a diffusion depth of

$0.85\mu m$. It is believed that the diffusion was affected by the segregation coefficient. These results seem to show that the Nd^{3+} ion requires a greater layer of oxide, or longer heating, to initiate Nd^{3+} outdiffusion. This effect, combined with the limitations on the furnace atmosphere limits the creation of waveguides by Nd^{3+} indiffusion.

6.6.7 Fluorescence Spectroscopy

The fluorescence of the Nd^{3+} indiffused samples was investigated by face pumping, normal to the samples surface, with an unfocussed beam from a titanium sapphire laser, tuned to the Nd^{3+}absorption at $808nm$. The fluorescence was captured from the polished side face of the sample.

The fluorescence spectrum from each indiffused sample was recorded with a triple grating spectrometer, and the results were compared to the spectrum from a $2.2at\%$ bulk doped Nd:YVO_4 sample. As can be seen in figure 6.9 the spectra are very similar, with a slight broadening of the main peak observed in the diffused sample, as the side peaks of the profile are not clearly resolved. Polarised spectra were also recorded (figure 6.10) and, although the low fluorescence signal led to noisy spectra, it can be seen that the indiffused and bulk spectra are similar.

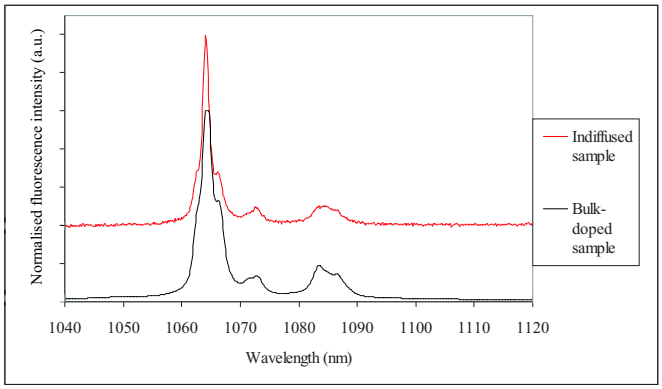

Figure 6.9: Unpolarised fluorescence spectra of indiffused Nd:YVO_4 and bulk doped Nd:YVO_4 samples

The fluorescence lifetime allows an indication of the doping concentration to be measured. The lifetime was recorded for a bulk doped sam-

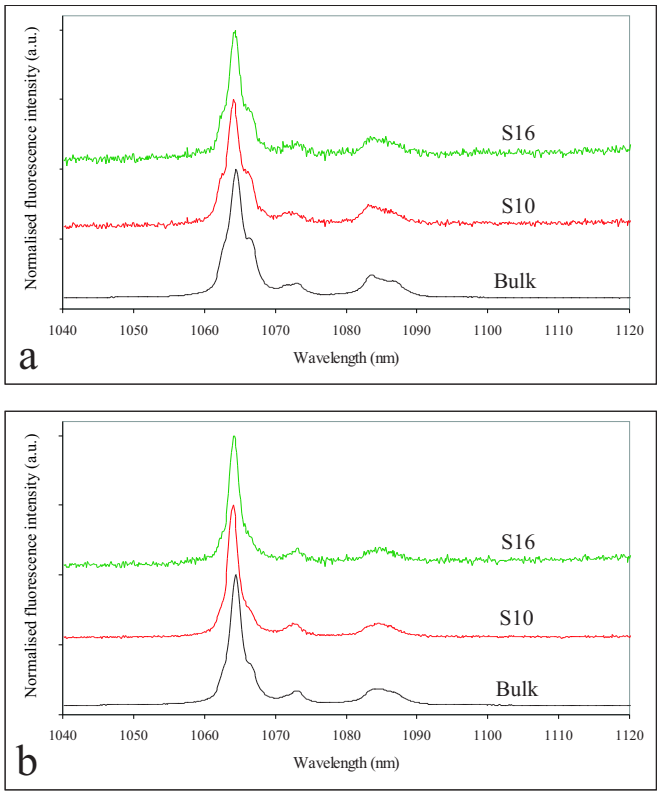

Figure 6.10: Fluorescence spectra of indiffused Nd:YVO_4 and bulk doped Nd:YVO_4 samples, a/σ polarisation, b/π polarisation

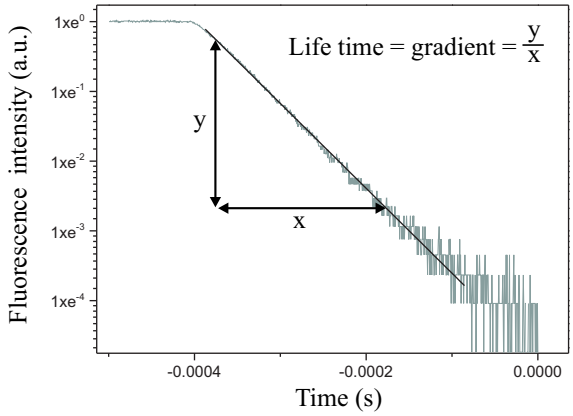

Figure 6.11: Typical fluorescence decay for Nd^{3+} diffused YVO_4

ple and each of the diffused samples, by chopping the titanium sapphire beam and recording the fluorescence decay with a silicon photodiode connected to a digital oscilloscope. A typical output of the fluorescence decay is displayed in figure 6.11. The lifetimes of the diffused spectra were measured between 70 and $110\mu s$ which can be compared to $\approx 50\mu s$ and $\approx 90\mu s$ for bulk-doped Nd:YVO_4 samples of 2 and $1at\%$ respectively. The results of this analysis would lead to an estimate of the doping concentration in the indiffused samples of 1.5–$2.5at\%$. However, SIMS analysis has shown much greater doping concentrations than that measured here. The difference between the doping concentrations calculated by each method can be explained, as the highly doped regions near the surface of the samples would suffer from strong non-radiative cross-relaxation [40], which would lead to only the fluorescence from the weakly doped tail of the diffusion profile being measured.

6.6.8 Investigation of Waveguide Modes

The modes supported by each of the indiffused waveguides were initially investigated by end-launching into each of the indiffused waveguides with either an argon ion laser, operating at $457, 488$ or $514nm$, or a He-Ne laser operating at $632.8nm$. The beam was launched into the waveguides with a $\times 10$ microscope objective and focussed, with another $\times 10$ microscope objective, onto a CCD camera. Sample 2 was the only indiffused sample to show waveguide properties, supporting a TM mode at 457 and $488nm$, although no TE modes were observed. The measured spot sizes on the CCD camera allowed calculation of a cavity mode spot size of $\approx 1.8\mu m$ to be calculated for both wavelengths.

The end-launch experiments were confirmed with the use of a dark-line prism coupler. The apparatus used was similar to that used in section 5.7.2. A single mode was again observed in sample 2, at 457 and $488nm$, with an extra mode present at $514nm$. The extra mode at $514nm$ that was not seen in the end-launch experiments, can be explained by the Nd^{3+} ion absorption at this wavelength. Unfortunately, due to the indices of the sample and prism used during this experiment, it was not possible to

confirm the lack of TE modes in this waveguide.

The assumptions made for the index change due to Nd^{3+} doping (section 6.4.2) were combined with the SIMS generated profile for sample 2 to model the behaviour of the waveguide. Close agreement was found for the cut-off ($\approx 560nm$) and modal-size ($\approx 1.8\mu m$ at 457 and $514nm$) with the experimentally derived results. No explanation for the lack of TE modes has been found, however, it is fortunate that the absorption cross-section for $807nm$ pumping, and emission cross-section at $1.06\mu m$ is greater for the TM polarisation of the diffused waveguides.

6.7 Summary

A theoretical discussion of the requirements for a diode-bar, side-pumped tapered waveguide laser has been completed, and leads to the conclusion that a substrate material with a high pump absorption coefficient is required. Yttrium vanadate (YVO_4) has been proposed as a suitable material, however, ion exchange techniques are not applicable to this crystal requiring a different fabrication technique. The production of waveguide structures within YVO_4 may be possible through the use of indiffusion.

The first indiffusion of Nd^{3+}, Gd^{3+} and Ti^{x+} in YVO_4 has been reported. The diffusion coefficient and activation energy of each ion has been determined and, with Ti^{x+} as the exception, have been found to be comparable to the values determined for indiffusion in YAG. SIMS analysis has allowed a measurement of the refractive index profile for each ion and, excepting Ti^{x+} indiffusion, has produced a good match with the theoretically expected profile.

The first waveguide formed by indiffusion of Nd^{3+} in YVO_4 was fabricated, with the modal properties of this waveguide measured by end-launch and prism coupling techniques. The experimentally measured mode size, number of supported modes and cut-off wavelength has been validated by modelling of the SIMS generated index profile.

Spectroscopic studies of the Nd^{3+}-indiffused waveguide have shown an

identical fluorescence spectra to that found in a bulk material. The fluorescence lifetime measured for these samples ranged between 50–$100\mu s$, leading to an early assumption of a Nd^{3+} doping concentration of around 1.5–$2.5at\%$. The disparity between the doping concentration measured by SIMS analysis and fluorescence lifetime has been attributed to concentration quenching due to the high Nd^{3+} doping concentration.

6.8 References

[1] R.V. Schmidt and I.P. Kaminow. Metal-diffused optical waveguides in LiNbO3. *Applied Physics Letters*, 25(8) : p458–460, 1974.

[2] I.P. Kaminow and J.R. Carruthers. Optical waveguiding layers in $LiNbO_3$ and $LiTaO_3$. *Applied Physics Letters*, 22(7) : p326–328, 1973.

[3] J.M. Hammer and W. Phillips. Low-loss single-mode optical waveguides and efficient high-speed modulators of $LiNb_xTa_{1-x}O_3$ on $LiTaO_3$. *Applied Physics Letters*, 24(11) : p545–547, 1974.

[4] R. Brinkmann, W. Sohler and H. Suche. Continuous-Wave Erbium-Diffused $LiNbO_3$ Waveguide Laser. *Electronics Letters*, 27(5) : p415–417, 1991.

[5] R. Brinkmann, W. Sohler, H. Suche and C. Wersig. Fluorescence and Laser Operation in Single-Mode Ti-Diffused Nd:MgO:$LiNbO_3$ Waveguide Structures. *IEEE Journal of Quantum Electronics*, 28(2) : p466–470, 1992.

[6] M. Hempstead, J.S. Wilkinson and L. Reekie. Waveguide Lasers Operating at 1084nm in Neodymium-Diffused Lithium Niobate. *IEEE Photonics Technology Letters*, 4(8) : p852–855, 1992.

[7] H.F. Taylor, W.E. Martin, D.B. Hall and V.N. Smiley. Fabrication of single-crystal semiconductor optical waveguides by solid-state diffusion. *Applied Physics Letters*, 21(3) : p95–98, 1972.

[8] W.E. Martin. Waveguide electro-optic modulation in II–VI compounds. *Journal of Applied Physics*, 44(8) : p3703–3707, 1973.

[9] J.K. Jones, J.P. de Sandro, M. Hempstead, D.P. Shepherd, A.C. Large, A.C. Tropper and J.S. Wilkinson. Channel waveguide laser at $1\mu m$ in Yb-indiffused $LiNbO_3$. *Optics Letters*, 20(13) : p1477–1479, 1995.

[10] J. Amin, M. Hempstead, J.E. Roman and J.S. Wilkinson . Tunable coupled-cavity waveguide laser at room temperature in Nd-diffused Ti:$LiNbO_3$. *Optics Letters*, 19(19), p1541–1543, 1994.

[11] H. Suche, L. Baumann, D. Hillier and W. Sohler. Modelocked Er:Ti:$LiNbO_3$ -waveguide laser. *Electronics Letters*, 29(12) : p1111–1112, 1993.

[12] P.K. Wei and W.S. Wang. Novel TE-TM mode splitter on lithium niobate using nickel indiffusion and proton exchange techniques. *Electronics Letters*, 30(1) : p35–37, 1994.

[13] R.C. Twu, C.C. Huang and W.S. Wang. Zn Indiffusion Waveguide Polariser on a Y-Cut $LiNbO_3$ at $1.32\mu m$ Wavelength. *IEEE Photonics Technology Letters*, 12(2) : p161–163, 2000.

[14] J.P. de Sandro, J.K. Jones, D.P. Shepherd, M. Hempstead, J. Wang and A.C. Tropper. Non-Photorefractive CW Tm-Indiffused Ti:$LiNbO_3$ Waveguide Laser Operating at Room Temperature. *IEEE Photonics Technology Letters*, 8(2) : p209–211, 1996.

[15] P. Becker, R. Brinkmann, M. Dinand, W. Sohler and H. Suche. Er-diffused Ti:$LiNbO_3$ waveguide laser of 1563 and 1576nm emission wavelengths. *Applied Physics Letters*, 61(11) : p1257–1259, 1992.

[16] D.M. Gill, A. Judy, L. McCaughan and J.C. Wright. Method for local incorporation of Er into $LiNbO_3$ guided wave optic devices by Ti co-diffusion. *Applied Physics Letters*, 60(9) : p1067–1069, 1992.

[17] L.M.B. Hickey. Ti:sapphire waveguide laser by the thermal diffusion of Ti into sapphire. *PhD. Thesis*, University of Southampton - Southampton, 1998.

[18] P.G. Shewmon. Diffusion in Solids. *McGraw-Hill*, New York, 1963.

[19] D.P. Shepherd, S.J. Hettrick, C. Li, J.I. Mackenzie, R.J. Beach, S.C. Mitchell and H.E. Meissner. High-power planar dielectric waveguide lasers. *Journal of Physics D*, 34 : p2420–2431, 2001.

[20] D.P. Shepherd, C.L Bonner, C.T.A. Brown, W.A. Clarkson, A.C. Tropper, D.C. Hanna and H.E. Meissner. High-numerical-aperture, contact-bonded, planar waveguides for diode-bar-pumped lasers. *Optics Communications*, 160 : p47–50, 1999.

[21] J.R. Lee, H.J. Baker, G.J. Hilton and D.R. Hall. High-average-power Nd:YAG planar waveguide laser that is face pumped by 10 laser diode bars. *Optics Letters*, 27(7) : p524–526, 2002.

[22] K. Scafer, I. Baumann, W. Sohler, H.Suche and S. Westenhofer. Diode-Pumped and Packaged Acoustooptically Tunable Ti:Er:$LiNbO_3$ Waveguide Laser of Wide Tuning Range. *IEEE Journal of Quantum Electronics*, 33(10) : p1636–1641, 1997.

[23] M. Fujimura, M.S. Khan, H. Tsugawa, M. Haruna, H. Nishihara, S. Ikunishi and T. Gozen. Thermally Nd-diffused Z-propagation Ti:$LiNbO_3$ waveguide laser pumped by laser diode. *Optics Letters*, 32(21) : p2003–2004, 1996.

[24] D.C. Hanna, A.C. Large, D.P. Shepherd, A.C. Tropper, I. Chartier, B. Ferrand and D. Pelenc. A side-pumped Nd:YAG epitaxial waveguide laser. *Optics Communications*, 91 : p229–235, 1992.

[25] J.I. Maxkenzie, S.C. Mitchell, R.J. Beach, H.E. Meissner and D.P. Shepherd. 15W diode-side-pumped Tm:YAG waveguide laser at $2\mu m$. *Electronics Letters*, 37(14) : p898–899, 2001.

[26] L. DeShazer. Vanadate Crystals exploit diode pump technology. *Laser Focus World*, 30(2) : p88–93, 1984.

[27] D.J. Pelenc. *PhD Thesis*, Universite Joseph Fourier - Grenoble I, 1993.

[28] C.L. Bonner. Multi-Watt, Diode-Pumped Planar Waveguide Lasers. *PhD Thesis*, University of Southampton - Southampton, 2000.

[29] L.G. Van Uitert, R.C. Linares, R.R. Soden and A.A. Ballman. Role of f-Orbital Electron Wave Function Mixing in the Concentration Quenching of Eu^{3+}. *Journal of Chemical Physics*, 36(3) : p702–705, 1962.

[30] J.R. O'Conner. Unusual Crystal-Field Energy Levels and Efficient Laser Properties of YVO_4:Nd. *Applied Physics Letters*, 9(11) : p407–409, 1966.

[31] R.A. Fields, M. Birnbaum and C.L. Fincher. Highly efficient Nd:YVO_4 diode-laser end-pumped laser. *Applied Physics Letters*, 51(23) : p1885–1886, 1987.

[32] Y.F. Chen, T.H Huang, C.C. Liao, Y.P. Lan and S.C. Wang. Efficient High-Power Diode-End-Pumped TEM_{00} Laser. *IEEE Photonics Technology Letters*, 11(10) : p1241–1243, 1999.

[33] A. Di Lieto, P. Minguzzi, A. Pirastu, S. Sanguinetti and V. Magni. A 7-W diode-pumped Nd:YVO_4 cw laser at $1.34\mu m$. *Applied Physics B*, B75 : p463–466, 2002.

[34] A. Brignon, G. Feugnet, J.P. Huignard and J.P. Pochelle. Compact Nd:YAG and Nd:YVO_4 Amplifiers End-Pumped by a High-Brightness Stacked Array. *IEEE Journal of Quantum Electronics*, 34(3) : p577–585, 1998.

[35] X. Peng, L. Xu and A. Asundi. Power Scaling of Diode-Pumped Nd:YVO_4 Lasers. *IEEE Journal of Quantum Electronics*, 38(9) : p1291–1299, 2002.

[36] P.M. Read, S.P. Speakman, M.D. Hudson and L. Considine. An ion beam investigation of the preliminary stages of titanium indiffusion in lithium niobate waveguides. *Nuclear Instruments and Methods in Physics Research*, B15 : p398–403, 1986.

[37] D.J. Cherniak. Rare earth element and gallium diffusion in yttrium aluminium garnet. *Physics and Chemistry of Minerals*, 26 : p156–163, 1998.

[38] K. Suzuki, Y. Yamashita, Y. Kataoka, K. Yamazaki and K. Kawamura. Segregation Coefficient of Boron and Arsenic at Polycrystalline Silicon/SiO_2 Interface. *Journal of the Electrochemical Society*, 140(10) : p2960–2964, 1993.

[39] T.T. Fang, W.T.C. Fang, P.B. Griffin and J.D. Plummer. Calculation of the fractional interstitial component of boron diffusion and segregation coefficient of boron in $Si_{0.8}Ge_{0.2}$. *Applied Physics Letters*, 68(6) : p791–793, 1996.

[40] S. Guy, C.L. Bonner, D.P. Shepherd, D.C. Hanna, A.C. Tropper and B. Ferrand. High-Inversion Densities in Nd:YAG: Upconversion and Bleaching. *IEEE Journal of Quantum Electronics*, 34(5) : p900–909, 1998.

Chapter 7

Conclusion

7.1 Summary

The first tapered dielectric waveguide lasers, fabricated by thermal ion exchange in Nd^{3+}-doped BK7 borosilicate glass, were demonstrated during this thesis. These lasers exhibited high efficiency operation for maximum taper widths up to $250\mu m$, and losses comparable to that of channel waveguides fabricated on the same substrate. The low-loss operation, combined with the measured spatial-output-profile from the laser leads to the conclusion that the tapers are acting adiabatically, as designed. A comparison of the laser performance of parabolic and linear tapered waveguides has also been completed, which indicated a clear advantage for the linear taper shape at taper widths of 175–$250\mu m$. The tapered waveguide lasers have been shown to be suitable for end-pumping with a broad-stripe diode-laser allowing the possibility of a $1W$-class integrated-optic laser source, although some further work is required to optimise the performance.

The laser performance of channel waveguides fabricated in Yb^{3+}-doped IOG-1 phosphate glass was determined, and found to produce efficient devices. Tapered waveguides fabricated within this glass did not lase due to available pump power being insufficient to reach threshold, however, high-power diode pumping of these waveguides should allow lasing. The threshold power of Yb^{3+} lasers is increased by the re-absorption

loss, which can be minimised by reducing the length of the gain medium. A hybrid substrate glass composed of bonded doped and undoped glass was fabricated to investigate the possibility of reducing the re-absorption loss, and hence the laser threshold. Preliminary investigation of the hybrid substrate was completed with a hybrid Nd:BK7/BK7 glass. Early testing of the substrate confirms that the bonding process, although simple, is very effective, and produces a mechanically strong and optically low loss bond.

Optimisation of the performance of a diode-end-pumped tapered waveguide led to an investigation of field-assisted ion exchange (FAIE). FAIE has previously been shown to produce a step-like index profile, which may allow the overlap between the multimoded pump and the single-mode laser to be improved. Analysis of waveguides fabricated by this process indicated a step-like index profile which matched the theoretically expected results.

The initial steps towards the realisation of a tapered waveguide suitable for diode-bar side-pumping have been completed. The indiffusion process required for production of waveguides of this type has been characterised for three different diffusant ions. The first indiffused waveguide in YVO_4 was produced, and the subsequent modelling of the waveguides modal properties attained a close match to experimentally determined results.

7.2 Tapered Waveguides fabricated by Thermal Ion Exchange

The design, TIE fabrication and laser performance of the first Nd:BK7, tapered waveguide laser was described in chapter 4. The $175\mu m$ wide, $12mm$ long linear tapered waveguide laser displayed a high slope efficiency of 42% and a loss of $0.2dBcm^{-1}$, comparable to that of a channel waveguide laser. The low-loss operation of the taper, combined with the measured output spatial-mode-profile indicates adiabatic performance from the simple linear taper design. These initial, and extremely promising results, pro-

voked further investigation into the optimisation of the taper shape and width. Parabolic and linear tapered waveguides were fabricated by TIE in Nd:BK7, with taper widths of 175–$250\mu m$ (11–$22mm$ long), under the design rule of Milton and Burns [1]. The expansion coefficient and taper widths used during the design of the waveguides led to additional losses, above the normal propagation loss, of $< 1.4dB$ for the linear tapers, while the parabolic taper loss was seen to increase dramatically with increasing taper width. It was concluded that linear tapered structures are more suited for large taper expansions (up to $250\mu m$), and are therefore more suited to diode-pumped devices. No indication of a major increase in the linear taper loss was noticed, implying that the adiabatic performance of these waveguides could be maintained for widths $> 250\mu m$.

The refractive index profile of the TIE fabricated waveguides was investigated by SIMS analysis. The close match with the theoretically expected index profile [2] confirmed the production of a graded index waveguide, and allowed confidence in the quality of the fabrication process.

The performance of the Nd^{3+}-doped waveguides provoked investigation into the performance of Yb^{3+}-doped lasers. Channel and tapered waveguides were fabricated in Yb^{3+}-doped IOG-1 phosphate glass. Characterisation of a channel waveguide laser allowed calculation of moderate-loss ($0.6dBcm^{-1}$) and high slope efficiency (50–75%) performance. Tapered waveguides fabricated within this material were calculated to require higher pump powers than were available at the time, to overcome the reabsorption loss and reach threshold. Broad-stripe diode-pumping of the tapered waveguides will allow access to the required pump power. The laser performance of the channel waveguides, coupled with the known adiabatic operation of the tapered structure, allows confidence in predicting good laser performance from these devices. In relation to Nd^{3+}, the Yb^{3+} ion allows access to a higher output power per unit pump power [3], this advantageous property may allow access to output powers of 2–$3W$ with diode-pump powers of 4–$8W$. Yb^{3+} also allows access to an operating wavelength of $\approx 980nm$, which may provide a competitive pump laser for erbium-doped amplifiers. However, optimisation of the TIE process with

IOG-1 glass is required to reduce surface degradation and improve yield. It is believed that the cause of the surface degradation has been identified, and is due to the inclusion of water in the glass during fabrication. Methods for excluding water during processing were discussed, and require further investigation.

The desire to produce an efficient Yb^{3+} laser operating at the highly three-level $980nm$ transition prompted work on the potential of a hybrid doped/undoped glass. Tapered waveguides fabricated in this glass, with only the broad-section of the waveguide being doped, would allow access to efficient pumping with a diode-laser, deliver single-spatial-mode output and minimise the re-absorption loss. Under this rationale a hybrid Nd:BK7/BK7 glass was created using a simple thermally-assisted bonding process. The resulting bond strength was found to be sufficient to allow dicing, polishing and TIE waveguide fabrication with no noticeable degradation. Channel and tapered waveguide lasers produced in this glass exhibited losses of $0.05dBcm^{-1}$ and $0.1dBcm^{-1}$ respectively, the lowest loss measured for any waveguide produced during this thesis, which indicates a high-quality, low-loss bond. A slope efficiency of 38% was measured for the tapered waveguide laser, under titanium sapphire pumping, a result comparable to that measured for an identical tapered waveguide fabricated in standard Nd:BK7. The simple, yet extremely effective bonding process, combined with a diode-pumped tapered waveguide could result in the production of various useful laser devices. Characterisation of the quasi-three-level $946nm$ Nd^{3+} transition will allow calculation of the effect of the hybrid glass on the re-absorption loss. Production of hybrid Yb^{3+}-doped/undoped glass substrates, followed by tapered waveguide fabrication may allow access to high-pump powers whilst producing low threshold power, high efficiency and single-mode laser operation.

Broad-stripe diode-pumped, $175\mu m$ wide, $12.5mm$ long linear tapered waveguide lasers exhibited an increase in the threshold power to $200 - 300mW$ and a reduction in the slope efficiency to 12.9%, in relation to titanium sapphire pumping. Investigation of the mechanisms involved with this degradation in performance, indicated a reduced pump and laser

overlap and insufficient pump absorption. However, the use of higher power, or polarisation coupled broad-stripe diode-lasers may still allow access to output powers of $\approx 1W$. Improved performance is expected from these devices with a move to a step-like index profile to improve the pump and laser overlap, an increase in the taper width to improve the launch efficiency and an increase in the length of the broad section to improve the pump absorption.

7.3 Tapered Waveguides fabricated by Field-Assisted Ion Exchange

FAIE theory was derived in chapter 5, followed by discussion of the fabrication parameters required to produce a step-like refractive index profile [4]. SIMS analysis of the FAIE waveguides exhibited a step-like index profile, with a close match to the theoretically expected profile. Diode-pumped tapered waveguide lasers fabricated by TIE have been shown to suffer from a reduced pump and laser overlap, the use of FAIE should allow this factor to be improved. An increase in the laser performance of the diode-pumped devices can be envisaged, if this improvement of the pump and laser overlap is combined with the optimised tapered waveguide design discussed in the previous section.

The practicalities required for the production of FAIE waveguides have been discussed in detail, and should prove useful to further research into the FAIE fabrication process. The fabrication of channel waveguides, and the production of the first tapered waveguide by the FAIE process has been shown to operate as theoretically expected, in respect to the waveguide depth attained. The values of waveguide depth measured by SIMS analysis were supported by prism coupling experiments.

The FAIE tapered waveguides exhibited poor laser performance, relative to identical tapered waveguides fabricated by TIE. The cause of the poor laser performance requires further investigation, although the creation of index lobes due to FAIE through a conducting mask is a likely candidate.

Optimisation of the FAIE process, with emphasis on the investigation of dielectric mask materials, should improve the laser performance of later FAIE waveguides.

TIE fabricated tapered waveguide lasers have exhibited near-symmetric, single-spatial-mode operation in both axes, and early research indicates a reasonable coupling efficiency with a broad-stripe diode laser. However, increasing the diode-pump power beyond $\approx 8W$ is accompanied by a decrease in the beam quality of the diode-pump. This reduction in beam quality could be accommodated in the tapered direction by increasing the width of the taper, whereas a double-clad structure [5] would increase the NA [6], and therefore the launch efficiency in the non-tapered direction. Waveguides of this form would be limited to diode-end-pumping due to the low pump absorption efficiency of Nd^{3+}-doped glass. The access to higher pump powers, afforded by the side-pumped geometry, was discussed in chapter 6, and required a new substrate material and fabrication method.

7.4 Indiffused Waveguides in Yttrium Vanadate

A theoretical investigation into the possible side-pumping of tapered waveguide lasers was completed in chapter 6. The requirement of a short pump absorption length led to the proposed use of yttrium vanadate (YVO_4) as a substrate material [7]. As the ion exchange process is not suited to the production of waveguides within crystals, indiffusion was proposed as a technique for the fabrication of tapered waveguides [8].

The production of a tapered waveguide laser within this important substrate material required an understanding of the indiffusion properties of various ions in YVO_4, and for this reason the indiffusion of Nd^{3+}, Gd^{3+} and Ti were studied. With the exception of Ti, the refractive index profiles of the diffused samples attained a good match with the theoretically expected profiles, confirming that the indiffusion was operating as expected. Furthermore, the resulting diffusion coefficient and activation energy calculated for the Nd^{3+} ion ($6.7 \times 10^{-19} m^2 s^{-1}$ at 1400°C and $5.3 \pm 0.7 \times 10^{-19} J$ respectively) were comparable to the value calculated for Nd^{3+} indiffusion

in YAG [9]. The Gd^{3+} ion exhibited an activation energy of $2.9\pm0.4\times10^{-19}J$ at $1400℃$, and a relatively high diffusion coefficient of $4.4 \times 10^{-18}m^2s^{-1}$.

Problems were noticed with Ti indiffusion, as very little Ti was measured to have diffused into the YVO_4. Outdiffusion of Ti was regarded as a possible cause of this, and further experiments were completed to investigate indiffusion of Ti in different furnace atmospheres. Unfortunately, indiffusion completed in an atmosphere other than oxygen caused severe surface degradation of the YVO_4 sample, which was attributed to oxygen outdiffusion from the crystal. Further investigation of the indiffusion of Ti is required. It may be possible to improve the indiffusion process by determining the concentration of oxygen required in the furnace atmosphere to inhibit oxygen outdiffusion, and mixing this concentration of oxygen with an ambient gas to inhibit oxide growth, and therefore limit segregation of the diffusion.

The fluorescence from the Nd^{3+} indiffused YVO_4 samples was characterised, and the spectra were found to be very similar to that of a bulk doped crystal. The fluorescence lifetime was measured at 50–$100\mu s$, leading to an early assumption of a Nd^{3+} doping concentration of around 1.5–$2.5at\%$. However, later SIMS analysis showed much higher doping concentrations up to $12at\%$, with the disparity between these results attributed to concentration quenching due to the high doping level [10].

The fabrication of the first indiffused waveguide in YVO_4 was also described in chapter 6. The modal characteristics of the Nd^{3+}-indiffused waveguide were tested by end-launching and prism coupling techniques, with a single TM mode determined at wavelengths up to $514nm$. Modelling of the SIMS derived index profile produced comparable results for the expected mode radii and predicted a cut-off wavelength of $560nm$, validating the measured results. The fabrication parameters required for the production of a single-mode waveguide at the Nd^{3+} laser wavelength were calculated, and the indiffusion was completed. Unfortunately, this resulted in a much lower Nd^{3+} concentration than expected, which is most probably due to outdiffusion of Nd^{3+}, caused by segregation of the diffusion. Thus, as has previously been indicated, a thorough investigation of

outdiffusion in YVO_4 is required.

An alternative route to the production of indiffused waveguides for propagation at $\approx 1\mu m$, is to utilise the relatively high diffusion coefficient of the Gd^{3+} ion. A short Nd^{3+} indiffusion would produce the required doping level, which would be followed by a Gd^{3+} indiffusion to produce the required index profile. Another option to reduce the duration of the indiffusion process would be to investigate co-diffusion which has successfully reduced the required fabrication time of Er-indiffused $LiNbO_3$ [11].

Once the indiffusion process has been optimised, the fabrication of channel and tapered waveguides will be investigated, and their laser performance characterised. The goal of the majority of waveguide lasers is the production of efficient, compact, high-power lasers with single-spatial-mode operation in both axes [12]. It is possible to envisage a double-clad, Nd^{3+}-indiffused YVO_4, diode-bar side-pumped tapered waveguide laser fulfilling many of these requirements.

7.5 References

[1] W.K. Burns, A.F. Milton and A.B. Lee. Optical waveguide parabolic coupling horns. *Applied Physics Letters*, 30(1) : p28–30, 1977.

[2] R.V. Ramaswamy and R. Srivastava. Ion-Exchanged Glass Waveguides: A Review. *Journal of Lightwave Technology*, 6(6) : p984–1001, 1987.

[3] T.Y. Fan. Solid State Lasers: New Developments and Applications. *Plenum Press*, New York, 1993.

[4] H.J. Lilienhof, E. Voges, D. Ritter and B. Pantschew. Field-Induced Profiles of Multimode Ion-Exchanged Strip Waveguides. *IEEE Journal of Quantum Electronics*, QE-18(11) : p1877–1883, 1982.

[5] C.T.A. Brown, C.L. Bonner, T.J. Warbuton, D.P. Shepherd, A.C. Tropper and D.C. Hanna. Thermally bonded planar waveguide lasers. *Applied Physics Letters*, 71(9) : p1139–1141, 1997.

[6] C.L. Bonner, T. Bhutta, D.P. Shepherd and A.C. Tropper. Double-Clad Structures and Proximity Coupling for Diode-Bar-Pumped Planar Waveguide Lasers. *IEEE Journal of Quantum Electronics*, 36(2) : p236–242, 2000.

[7] L. DeShazer. Vanadate Crystals exploit diode pump technology. *Laser Focus World*, 30(2) : p88–93, 1984.

[8] P.G. Shewmon. Diffusion in Solids. *McGraw-Hill*, New York, 1963.

[9] D.J. Cherniak. Rare earth element and gallium diffusion in yttrium aluminium garnet. *Physics and Chemistry of Minerals*, 26 : p156–163, 1998.

[10] S. Guy, C.L. Bonner, D.P. Shepherd, D.C. Hanna, A.C. Tropper and B. Ferrand. High-Inversion Densities in Nd:YAG: Upconversion and Bleaching. *IEEE Journal of Quantum Electronics*, 34(5) : p900–909, 1998.

[11] D.M. Gill, A. Judy, L. McCaughan and J.C. Wright. Method for local incorporation of Er into $LiNbO_3$ guided wave optic devices by Ti co-diffusion. *Applied Physics Letters*, 60(9) : p1067–1069, 1992.

[12] D.P. Shepherd, S.J. Hettrick, C. Li, J.I. Mackenzie, R.J. Beach, S.C. Mitchell and H.E. Meissner. High-power planar dielectric waveguide lasers. *Journal of Physics D*, 34 : p2420–2431, 2001.

Appendix A

The Effective Index Method

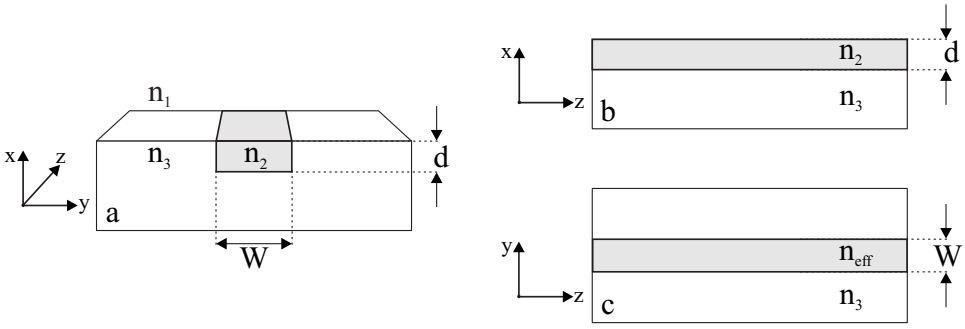

Figure A.1: Diagrammatic representation of: a/ a channel waveguide, and the channel as viewed through b/ the xz-plane and c/ the yz-plane

The effective index method is a useful tool for calculating the modal properties of non-planar waveguides [1]. The guidance afforded by the channel geometry (figure A.1a) is the result of confinement in both lateral directions (x and y-directions). The method used for finding the mode solutions of an asymmetric waveguide (chapter 2) assume that the structure is homogenous in the y-direction, and is therefore not applicable to the channel geometry. The effective index method operates by dissecting the original waveguide into two separate waveguides: one in the xz plane (figure A.1b), and one in the yz-plane (figure A.1c). In this way, the waveguides can be solved separately, with the sum of the solutions allowing the calculation of the modal properties of the original channel waveguide.

The method begins by viewing the channel waveguide in the xz-plane

between $W/2 \leqslant y \leqslant -W/2$. If the y-axis variation of the waveguide is neglected, or alternatively if $W \rightarrow \infty$, the channel appears to be an asymmetric planar waveguide . Parameters are defined to describe the normalised depth V, and the normalised index b [1]:

$$V = k_0 d \left(n_2^2 - n_3^2\right)^{\frac{1}{2}} \tag{A.1}$$

$$b = \frac{n_{eff}^2 - n_3^2}{n_2^2 - n_3^2} \tag{A.2}$$

These parameters are substituted into the guidance equation for the asymmetric waveguide (equation 2.25) producing:

$$V\left(1-b\right)^{\frac{1}{2}} = p\pi + \tan^{-1}\left(\frac{b}{1-b}\right)^{\frac{1}{2}} + \tan^{-1}\left(\frac{b+a}{1-b}\right)^{\frac{1}{2}} \tag{A.3}$$

Where p is the mode number, a is a measure of the waveguide asymmetry, which ranges from 0 for a symmetric waveguide, to ∞ for a highly asymmetric waveguide, and is defined differently for TE or TM modes:

$$\begin{aligned} a^{TE} &= \left(\frac{n_3^2 - n_1^2}{n_2^2 - n_3^2}\right) \\ a^{TM} &= \left(\frac{n_2^2}{n_1^2}\right)^2 \left(\frac{n_3^2 - n_1^2}{n_2^2 - n_3^2}\right) \end{aligned} \tag{A.4}$$

Entering the values of n_1^2, n_2^2, n_3^2, d and k_0 into equation A.3, then solving for n_{eff}, allows calculation of the mode behaviour of the asymmetric waveguide. It can be seen that the properties of the channel waveguide in the xz-plane can be modelled through the value of n_{eff}.

To understand the properties of the channel waveguide in yz-plane, the channel can be substituted for a symmetric planar waveguide of width W (figure A.1c), with the core index altered so that $n_2 = n_{eff}$. It should be noted that this waveguide is fictitious, as n_{eff} is different for each mode. Parameters are defined, within this plane, for the normalised depth V' and the normalised index b' [1]:

$$V' = k_0 W \left(n_{eff}^2 - n_3^2\right)^{\frac{1}{2}} \tag{A.5}$$

$$b' = \frac{n_{eff}'^2 - n_3^2}{n_{eff}^2 - n_3^2} \tag{A.6}$$

There is no requirement for an asymmetry measure, as the waveguide is symmetric. Equations A.5 and A.6 are substituted into the guidance equation (equation 2.25), and produce the normalised guidance equation within the yz-plane:

$$V'\left(1 - b'\right)^{\frac{1}{2}} = p\pi + 2\tan^{-1}\left(\frac{b'}{1 - b'}\right)^{\frac{1}{2}} \tag{A.7}$$

As the core index was altered to take into account the behaviour of the waveguide in the xz-plane using the value calculated for n_{eff}, the solutions of the above guidance equation are the mode solutions of the original channel waveguide.

A.0.1 Propagation Angle in a Channel Waveguide

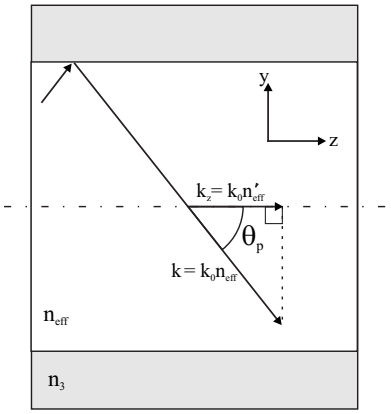

Figure A.2: Ray propagation angle in a channel waveguide

The effective index method can now be used to study the projection of a ray within a channel waveguide. The ray model assumes that the waveguide mode propagates with the direction of propagation being that of the mode wave-vector k, as shown in figure A.2, where:

$$\begin{aligned} k &= k_0 n_{eff} \\ k_z &= k_0 n'_{eff} \end{aligned} \tag{A.8}$$

Which allows the propagation angle θ_p to be stated:

$$\cos\theta_p = \frac{k_0 n'_{eff}}{k_0 n_{eff}} = \frac{n'_{eff}}{n_{eff}} \tag{A.9}$$

The values n_{eff} and n'_{eff} can be related to measurable quantities by rearranging equations A.2 and A.6:

$$\begin{aligned} n_{eff} &= \left[n_3^2 + b\left(n_2^2 - n_3^2\right)\right]^{\frac{1}{2}} \\ n'_{eff} &= \left[n_3^2 + bb'\left(n_2^2 - n_3^2\right)\right]^{\frac{1}{2}} \end{aligned} \tag{A.10}$$

A parameter Δn is defined as the difference in index of the original channel waveguide core and substrate, where $\Delta n = n_2 - n_3$. Small values of Δn, as created by ion exchange and indiffusion, allow the approximation $n_2^2 - n_3^2 \approx 2n_3\Delta n$ to be made. Substituting equations A.10 into equation A.9, making use of the approximation, produces:

$$\cos\theta_p = \left(\frac{n_3^2 + 2bb'n_3\Delta n}{n_3^2 + 2bn_3\Delta n}\right)^{\frac{1}{2}} \tag{A.11}$$

The above equation shows the relationship between the waveguide indices and the propagation angle, this can be further simplified with the use of a Taylor series, producing the equation as quoted by Milton and Burns [2]:

$$\cos\theta_p = \frac{n_3 + bb'\Delta n}{n_3 + b\Delta n} \tag{A.12}$$

A.1 References

[1] D.L. Lee. Electromagnetic Principles of Integrated Optics. *J. Wiley & Sons*, Ch. 5, New York, 1986.

[2] W.K. Burns, A.F. Milton and A.B. Lee. Optical waveguide parabolic coupling horns. *Applied Physics Letters*, 30(1) : p28–30, 1977.

Appendix B

Taper Design Features of Photolithographic Masks

The following appendix has been added to reduce the size and complexity of the experimental chapters. In this way the design features of the photolithographic masks used to fabricate tapered waveguides, need only be listed once and can be referenced when required.

Three different groups of tapers were used during this thesis. The features within these groups are listed in tables B.1 to B.3.

Group 1 tapers were available at the start of this work, and were used as it was believed they would offer reasonable adiabatic operation. Group 2 and 3 tapers were designed after initial work had begun with the group 1 tapers. Group 2 tapers were used to investigate the effect of increasing width on the operation of a linearly tapered waveguide, which had exactly the same taper angle as the group 1 tapers. The parabolic tapers within group 3 were designed using the Milton and Burns approach (equation 3.13). Parabolic tapers were designed using $\alpha = 2$, although not totally adiabatic this value would allow high conversion efficiencies, and the reduction in taper length would make wide taper openings possible for the short substrate lengths available. Linear tapers were then designed to have an identical width and length as the parabolic tapers, as this would allow fair comparison of the effect of the taper shape on adiabatic operation.

All tapers were fabricated with $2.5\mu m$ wide channel sections. The possible length of the channel and broad section was approximately $3cm$, dependent on the substrate length. The length of these sections within the tapered waveguides was designed by tailoring the substrates length.

Feature number	Feature type	Max. feature width (μm)	Taper length (mm)	Taper angle ($^\circ$)
1	Linear taper	175	12.5	0.40
2	Channel	2.5	—	—
3	Linear taper	175	12.5	0.40
4	Channel	2.5	—	—
5	Linear taper	175	12.5	0.40

Table B.1: Design features of mask group 1: Linear tapers

Feature number	Feature type	Max. feature width (μm)	Taper length (mm)	Taper angle ($^\circ$)
1	Linear taper	175	12.5	0.40
2	Linear taper	175	12.5	0.40
3	Channel	2.5	—	—
4	Linear taper	200	14.3	0.40
5	Linear taper	200	14.3	0.40
6	Channel	2.5	—	—
7	Linear taper	250	17.9	0.40
8	Linear taper	250	17.9	0.40
9	Channel	2.5	—	—
10	Linear taper	300	21.5	0.40
11	Linear taper	300	21.5	0.40
12	Channel	2.5	—	—
13	Linear taper	350	25.1	0.40
14	Linear taper	350	25.1	0.40

Table B.2: Design features of mask group 2: Linear tapers of different width

Feature number	Feature type	Max. feature width (μm)	Taper length (mm)	Taper angle (°)	α value
1	Linear taper	175	11.0	0.45	—
2	Parabolic taper	175	11.0	—	2
3	Channel	2.5	—	—	—
4	Linear taper	200	14.3	0.40	—
5	Parabolic taper	200	14.3	—	2
6	Channel	2.5	—	—	—
7	Linear taper	250	22.3	0.32	—
8	Parabolic taper	250	22.3	—	2
9	Channel	2.5	—	—	—
10	Linear taper	300	32.2	0.26	—
11	Parabolic taper	300	32.2	—	2
12	Channel	2.5	—	—	—
13	Linear taper	350	43.8	0.23	—
14	Parabolic taper	350	43.8	—	2

Table B.3: Design features of mask group 3: Linear and parabolic tapers of identical length

Appendix C

Derivation of the Non-Linear Diffusion Equation

The current density equation for either ion A (the diffusant ion) or ion B (the exchanger ion) is [1]:

$$\underset{\sim}{J}_i = q\mu_i C_i \underset{\sim}{E} - D_i \nabla C_i \tag{C.1}$$

where i is used to denote either ion A or B, $\underset{\sim}{J}_i$ is the ion flux, μ_i is the ionic mobility, C_i is the concentration, $\underset{\sim}{E}$ is the electric field and D_i is the diffusion coefficient.

The diffusion coefficient and mobility of the ions are related by the Einstein relation [2]:

$$D_i = \frac{kT\mu_i}{q} \tag{C.2}$$

where k is Boltzmann's constant, T is the absolute temperature and q is the charge on the electron.

The electric field is determined by the Poisson equation:

$$\nabla \cdot \underset{\sim}{E} = \frac{q}{\varepsilon}\left(C_A + C_B - C_B^0\right) \tag{C.3}$$

where C_B^0 is the absolute concentration of the exchanger ions, before ion

exchange.

The continuity equation for each ion relates the concentration temporal dependance to the spatial distribution:

$$\nabla \cdot \underset{\sim}{J}_i + q\frac{\partial C_i}{\partial t} = 0 \tag{C.4}$$

The total current density is the sum of the flux for each ion, and as these fluxes are equal and opposite, the total current density is zero:

$$\nabla \cdot \left(\underset{\sim}{J}_A + \underset{\sim}{J}_B\right) = 0 \tag{C.5}$$

The continuity equations are substituted into the above equation to gain:

$$q\nabla \cdot \underset{\sim}{E}\left(\mu_A C_A + \mu_B C_B\right) + q\underset{\sim}{E}\left(\mu_A \nabla C_A + \mu_B \nabla C_B\right) - D_A\nabla^2 C_A + D_B\nabla^2 C_B = 0 \tag{C.6}$$

where ∇^2 is the Laplace operator.

The total ion concentration within the glass is constant, assuming that the ion exchange occurs on a one-for-one basis, and therefore:

$$C_A + C_B = C_B^0 = \text{constant} \tag{C.7}$$

This simple equation, combined with the rules of vector calculus, allows the following to be deduced:

$$\nabla C_A = -\nabla C_B, \text{ and } \nabla^2 C_A = -\nabla^2 C_B \tag{C.8}$$

Rearranging equation C.6, using the Einstein relation to simplify, produces:

$$\nabla \cdot \underset{\sim}{E} = \frac{1-M}{1-(1-M)\,c}\left(\underset{\sim}{E} \cdot \nabla c - \frac{kT}{q}\nabla^2 c\right) \tag{C.9}$$

Where the mobility ratio is:

$$M = \frac{\mu_A}{\mu_B} \tag{C.10}$$

and the normalised concentration for ion A is:

$$c = \frac{C_A}{C_B^0} \tag{C.11}$$

Finally, equation C.9 and C.1 are substituted into equation C.4 to gain the nonlinear differential equation for the A ions:

$$\frac{\partial c}{\partial t} + \frac{1}{1-(1-M)\,c}\mu_A \underset{\sim}{E} \cdot \nabla c = \frac{D_A}{1-(1-M)\,c}\nabla^2 c \tag{C.12}$$

C.1 References

[1] H.J. Lilienhof, E. Voges, D. Ritter and B. Pantschew. Field-Induced Index Profiles of Multimode Ion-Exchanged Strip Waveguides. *IEEE Journal of Quantum Electronics*, QE-18(11) : p1877–1883, 1982.

[2] R.V. Ramaswamy and R. Srivastava. Ion-Exchanged Glass Waveguides: A Review. *Journal of Lightwave Technology*, 6(6) : p984–1001, 1987.

Appendix D

List of Publications

D.1 Journal Publications

S.J. Hettrick, J.I. Mackenzie, R.D. Harris, J.S. Wilkinson, D.P. Shepherd and A.C. Tropper. Ion-Exchanged Nd:glass tapered waveguide laser. *Optics Letters*, 25(19) : p1433–1435, 2000.

D.P. Shepherd, S.J. Hettrick, C. Li, J.I. Mackenzie, R.J. Beach, S.C. Mitchell and H.E. Meissner. High-power planar dielectric waveguide lasers. *Journal of Physics D*, 34(16) : p2420–2432, 2001.

S.J. Hettrick, J.S. Wilkinson and D.P. Shepherd. Neodymium and gadolinium diffusion in yttrium vanadate. *Journal of the Optical Society of America B*, 19(1) : p33–36, 2002.

S.J. Hettrick, J. Wang, C. Li, J.S. Wilkinson and D.P. Shepherd. An Experimental Comparison of Linear and Parabolic Tapered Waveguide Lasers and a Demonstration of Broad-Stripe Diode Pumping. *Journal of Lightwave Technology*, to be published, March 2004.

D.2 Conference Publications

S.J. Hettrick, J.I. Mackenzie, R.D. Harris, J.S. Wilkinson, A.C. Tropper and D.P. Shepherd. Ion-Exchanged Nd:glass tapered waveguide laser. *CLEO/Europe*, Nice, 10–15 Sep., 2000, CTuM6.

C. Li, S.J. Hettrick, J.I. Mackenzie, J.S. Wilkinson and **D.P. Shepherd**. Longitudinally-diode-pumped high-power waveguide lasers. *ECIO*, Paderborn, 4–6 Apr., 2001. WeB2.4.

S.J. Hettrick, J.S. Wilkinson and D.P. Shepherd. Thermally diffused waveguides in YVO_4. *Quantum Electronic and Photonics (QEP-15)*, Glasgow, 3–6 Sep., p179, 2001.

S.J. Hettrick, J.S. Wilkinson and D.P. Shepherd. Neodymium and gadolinium diffusion in yttrium vanadate. *14th Annual Meeting of the IEEE Lasers and Electro-Optics Society (LEOS)*, San Diego, 12–15 Nov., 2001. MP2.

S.J. Hettrick, C. Li, J.I. Mackenzie, J.S. Wilkinson and D.P. Shepherd. Nd:glass tapered planar waveguide laser. *14th Annual Meeting of the IEEE Lasers and Electro-Optics Society (LEOS)*, San Diego, 12–15 Nov., 2001. MP3.

D.P. Shepherd, J.I. Mackenzie, S.J. Hettrick and C. Li. Planar waveguides for high power laser devices. *Doctoral School Programme - Swiss Federal Institute of Technology*, Lausanne, 2002 (invited).

S.J. Hettrick, J. Wang, C. Li, J.S. Wilkinson and **D.P. Shepherd**. An experimental comparison of linear and parabolic tapered waveguide lasers. *ECIO*, Prague, 2–4 Apr., 2003. ThA2.5.